Chemical Vapour Deposition of Large-area High-quality Graphene Films for Electronic Applications

Kai WANG

A thesis submitted to Imperial College London

In fulfilment of the requirements for the degree of

Doctor of Philosophy

Department of Materials

Imperial College London

April 2014

Declaration

This thesis is the author's own work, unless those cited to references. Parts of this thesis have been published, or are in the submission preparation.

Acknowledgements

Firstly I would like to express my deepest appreciation to Prof. Norbert Klein and Prof. Neil Alford. Without their guidance and help this dissertation would not have been possible. Especially I would like to thank them for the encouragement during times when I lacked confidence and patience.

I also would like to thank all the colleagues I have met in the past 3.5 years, especially Dr. Olena Shaforost, Dr. Stephen Hanham and Dr. Toby H. Basey-Fisher for help and discussions in the microwave measurement; Dr. Cecilia Mattevi and Dr. HoKwon Kim, Stefan Goniszewski, and Mohammad Adabi for help and discussions in the graphene growth and transfer; Dr. Peter K. Petrov, Dr Bin Zou, Dr Tianle Wang for help in electrical measurements and thin film fabrication techniques; Dr Yannick Sonnefraud and Dr. Sasha Rakovich for help in the Raman characterization; William Otter for help and discussions in device fabrications; Mahmoud G Ardakani, Russell Stracey, Benjamin Chan and other technicians for various help during my experiments.

Special thanks to my family and all my friends in the UK and China, who always support me during ups and downs.

Last but not the least; I would like to thank KAUST for the generous financial support.

Table of Contents

List of Figures

List of Tables

Abstract

Low Pressure Chemical Vapour Deposition (LPCVD) and transfer processes are explored and optimized to obtain large-area, continuous and high quality monolayer graphene on target substrate. The size of synthesized graphene reaches up to 20 mm * 20 mm, and can be further extended by upgrading to a larger reaction chamber; the monolayer coverage rate and conductivity is better than normal commercial graphene products on the market. A novel frame-assisted method is developed to transfer graphene without introducing many defects and impurities. Annealing and acetone treatment are combined to remove PMMA residues effectively and unharmfully. A new under-etching route to fabricate graphene free-standing structure is also proposed and explored.

A novel non-contact microwave examination method has been employed to simplify the sheet resistance measurement processes and to avoid the effects of metallic contacts. This method is simple and non-destructive to graphene, and can be further integrated into the graphene production line in the future. A new double-layer device is fabricated and utilized to observe the microwave field effect in graphene.

The interaction between graphene and oxygen under different temperatures and oxygen partial pressures is studied and discussed. Strontium Titanate films ($SrTiO_3$ or STO) are deposited on transferred CVD grown graphene on MgO substrates. Based on the oxidation test result, the deposition process of Strontium Titanate is optimized to minimize the defects introduced on graphene. Raman mapping data show that graphene is still continuous after the STO deposition although the D band suggests some newly formed defects.

Key works: graphene, chemical vapour deposition, transfer, microwave measurement

1. Introduction

1.1 Properties and Applications of Graphene

Graphene is a monoatomic 2-D material in which sp^2 hybridized carbon atoms are closely arranged as a hexagonal crystal lattice. [1] Graphene is the basic 2D building unit which can be transformed into all other carbon materials, such as being wrapped up to fullerenes (0D), being rolled to carbon nanotubes (1D) or being stacked to graphite (3D) (Figure 1-1).

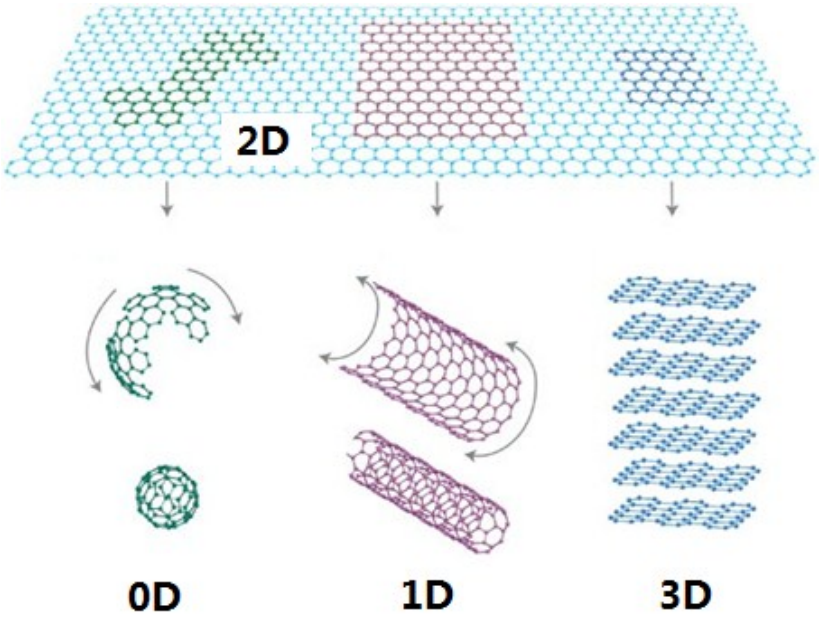

Figure 1-1: Structure of Graphene and its relationship with carbon materials in other dimensions.
Left: 0-D fullerenes; Middle: 1-D carbon nanotubes; Right: 3-D graphite.(adapted from reference [1])

Although theoretically predicted to have many fascinating properties, free-standing graphene, the thermodynamically unstable two-dimensional crystal, was considered impossible to exist. It was not until 2004 that suspended graphene was first discovered by A. Geim and K. Novoselov [2]. Since then, and especially after the awarding of Nobel Physics Prize in 2010, graphene has attracted great research interests in areas such as physics, chemistry, nanoelectronics, materials science and bioscience because of its fascinating electronic, optical, mechanical and thermal properties (Figure 1-2):

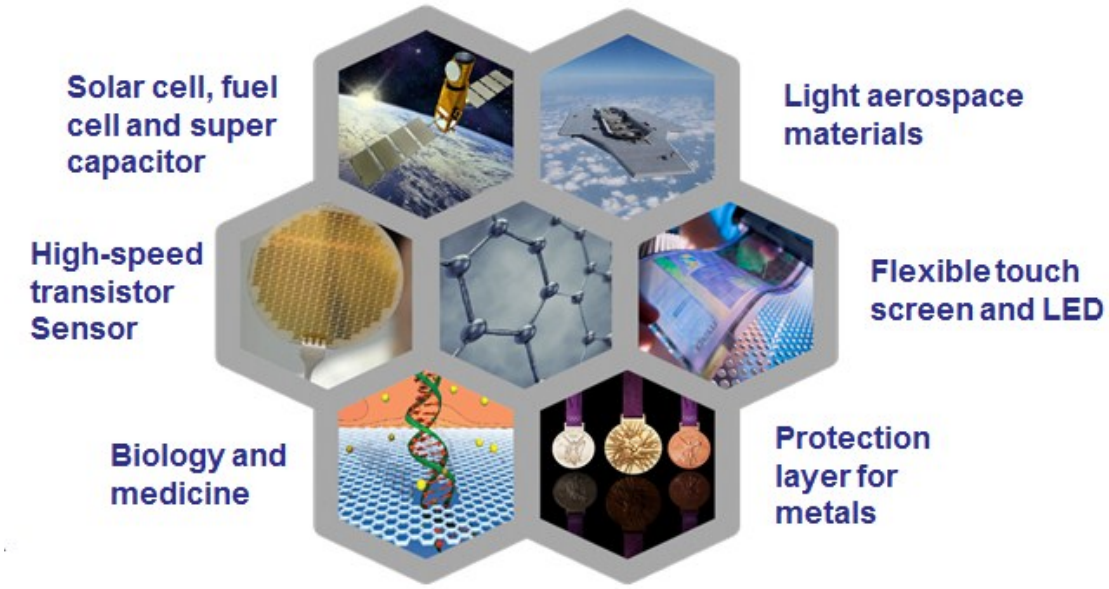

Figure 1-2: Various suggested applications of graphene.

Graphene's great mechanical strength [5] (Young's modulus of 1 TPa) and low mass density (~2300 kg/m^3) make it an ideal candidate for various composites, especially in aerospace industry. The high surface to volume ratio opens the opportunity of advanced gas sensors and bioelectric sensors [20]. The monolayer only absorbs about 2.3% of normally incident light [8], which makes graphene also a favourable alternative for transparent electrodes in solar cells, touch screens and LEDs. It has a

high electron mobility of up to 200,000 cm^2/Vs [15; 16; 17], high current density of up to $\sim 2 \times 10^8$ $A\,cm^{-2}$ [18], high saturation velocity of up to 5.5×10^7 $cm\,s^{-1}$ [19]and a high thermal conductivity (above 5,000 $W\,mK^{-1}$ [11]), which are ideal for many high-speed electronic applications. The chemically inert nature of graphene also makes it a great corrosion barrier for metal protection.

1.2 Motivation and Goals

Despite graphene's promising properties and applications, two obstacles remain in its way to commercialization as a large-area transparent electrode: how to achieve mass production of graphene on a large scale and how to effectively modulate graphene's electrical conductivity (Table 1-1). In this thesis, various studies have been conducted to explore solutions to the two problems:

	ITO	Carbon Nanotube	Graphene (monolayer)
Young's modulus (GPa)	116 [3]	<950 [4]	1020 [5]
Transmittance (%)	>90 [6]	90 [7]	97.7 [8]
Heat Conductivity (W/m-K)	~10 [9]	3500 [10]	5000 [11]
Sheet Resistance (Ω/sq)	< 100 [6]	~500 [12]	125-5000 [6; 12]
electron Mobility(cm^2/Vs)	<50 [13]	100,000 [14]	200,000(Exfoliated) [15; 16; 17] ~7,300 (CVD) [6]
Mass production	Yes	Yes	In development

Table 1-1: Comparison in properties of graphene, ITO and carbon nanotube for large-area transparent electrodes.

Chapter 2 reviews the recent advances in graphene synthesis. Various preparation methods are reviewed and compared.

Chapter 3 describes the main fabrication and characterization techniques which are employed in this thesis.

Chapter 4 explores how to obtain high quality graphene on a large scale: a low pressure chemical vapour deposition (LPCVD) system is set up to synthesize

graphene on copper. The deposition conditions are studied and optimized to synthesize large-area high-quality graphene sheets. It further discusses the transfer of synthesized graphene sheet from a copper catalyst to target substrates and how to minimize the damage during this process. A new under-etching route to fabricate a graphene free-standing structure is also proposed and explored.

Chapter 5 is about the employment of a new microwave method to examine graphene's electrical properties: a microwave resonator is employed to enable contact-free determination of sheet resistance in a convenient, accurate and low-cost way. A double-layer graphene device is also designed and fabricated and the field effect in graphene is also (indirectly) observed with the microwave resonator.

Chapter 6 studies the deposition of Strontium Titanate (STO) dielectric films onto graphene sheet for future top-gated FET transistors and capacitor applications. The interactions between graphene and oxygen under different temperatures and oxygen partial pressures were studied to optimize the STO deposition conditions and to minimize the damage of graphene.

2. Literature Review[1]

This chapter reviews various major graphene synthesis techniques (Table 2-1). The pros and cons of each are also discussed and compared.

Method	Carbon Source
Mechanical exfoliation	Highly Ordered Pyrolytic Graphite (HOPG)
Chemical exfoliation	
Reduction of graphene oxides	
Epitaxial growth on SiC	SiC
Chemical vapour deposition	Hydrocarbon gases (such as Methane or Ethylene)
Decomposition from solid carbon source	Organic molecules

Table 2-1: An overview of major graphene synthesis methods

[1] Part of this chapter has been submitted to Imperial College London in the Early Stage Review report.

2.1 Exfoliation from graphite

2.1.1 Mechanical Exfoliation

High quality graphene sheets were first generated using mechanical exfoliation of Highly Ordered Pyrolytic Graphite (HOPG) by Geim, A. K. and colleagues [2; 21]. After repeated peeling by using an adhesive tape, graphene crystals, along with graphite particles, were then transferred onto Si substrates which are covered with a certain thickness (normally ~300 nm) of SiO_2 layer, where they became visible due to a feeble interference-like contrast compared with an empty wafer (Figure 2-1). (See section 3.2.1 Optical Microscope for more details)

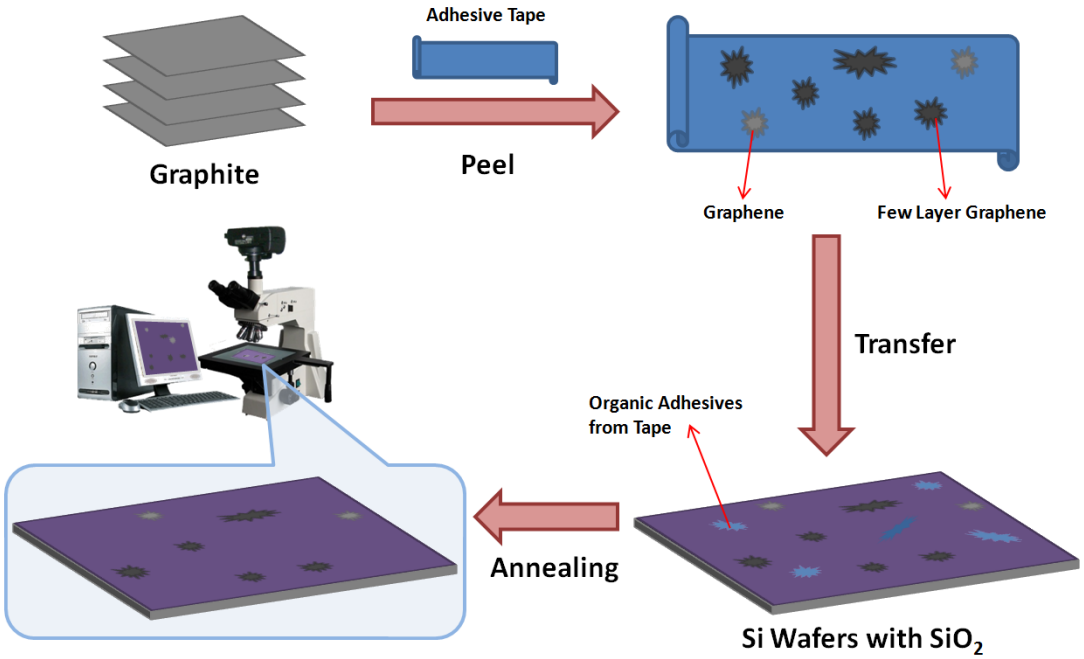

Figure 2-1: Schematic of the 'Scotch-Tape' Method.

These exfoliated graphene sheets have the best structures and performances[16; 17] till

now, with a size of up to 100 μm[1] (Figure 2-2). So they are considered pristine graphene which can be used to compare performances and structures of graphene prepared by other methods. However the randomness of products made it difficult to prepare graphene sheets on a large scale or in a well-controlled shape, size and number of layers. So exfoliated graphene is now mainly used for basic research and new concept devices. New preparation methods for graphene sheets on a large scale are in urgent need for industrial applications.

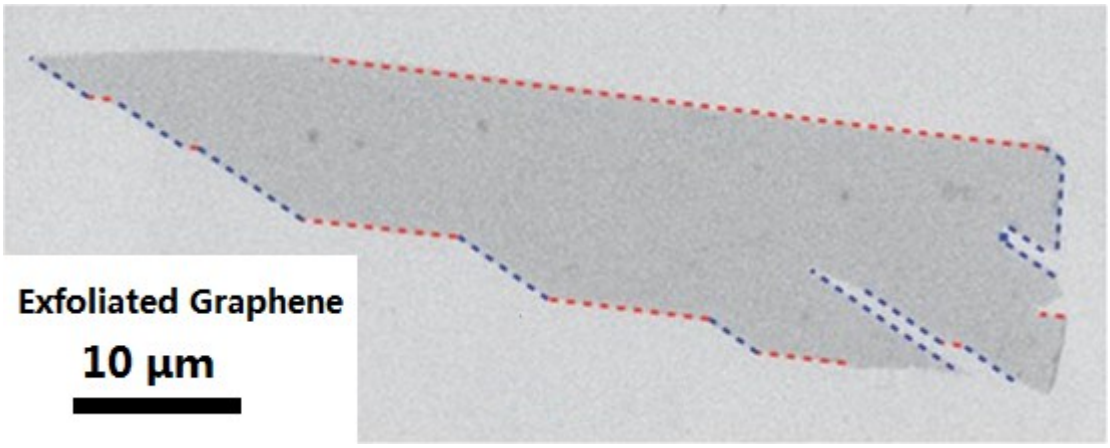

Figure 2-2: SEM Image of an exfoliated graphene crystal. The blue and red dotted lines illustrate the zigzag and armchair edges.

(adapted from reference [1])

2.1.2 Chemical Exfoliation

Other than the traditional mechanical exfoliation, methods such as intercalation [22] (Figure 2-3) and liquid phase exfoliation [23; 24] (Figure 2-4) are explored to achieve mass exfoliation of graphite layers. During the sonication process, the graphite bulk

fragments into graphene sheets, while the solvent molecules stabilize the separated sheets from aggregation. Despite that chemical exfoliation greatly improves the scale of production, lack of control in shapes and number of layers still makes this method unsuitable for device applications.

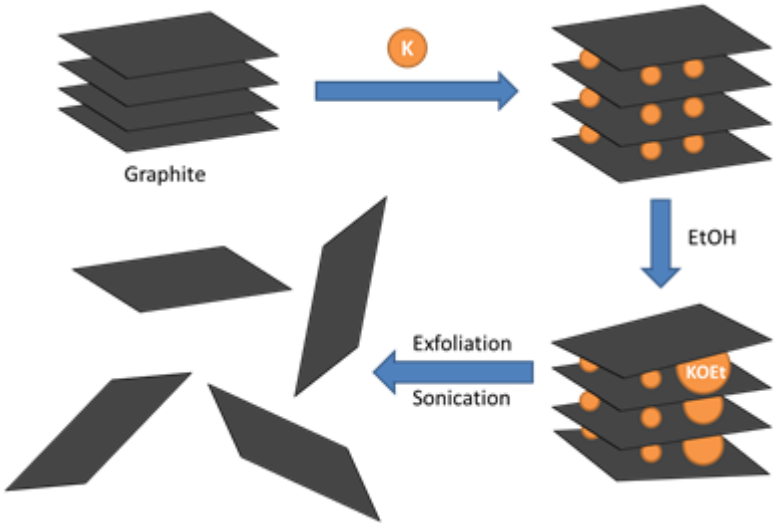

Figure 2-3: Schematic of the intercalation method

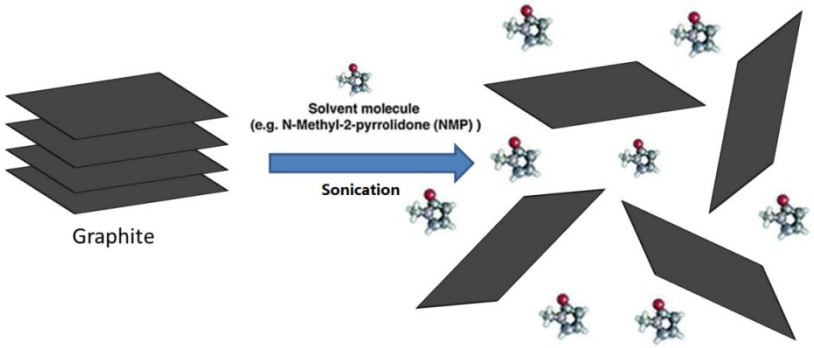

Figure 2-4: Schematic of the liquid phase exfoliation method

2.2 Reduction of Graphene Oxides

Another method of separating sheets from graphite is oxidation by treatment with a strong acid [25], which introduces oxygen-bearing functional groups (such as phenols, carboxylic acids, epoxides, other carbonyls) to the graphite layers. After sonication in water, due to the electrostatic repulsion between the negative charges on adjacent layers brought by deprotonating of functional groups, the graphite layers separate to form graphene oxide sheets, which can be then transferred and reduced by thermal annealing in hydrazine vapour. (Figure 2-5)

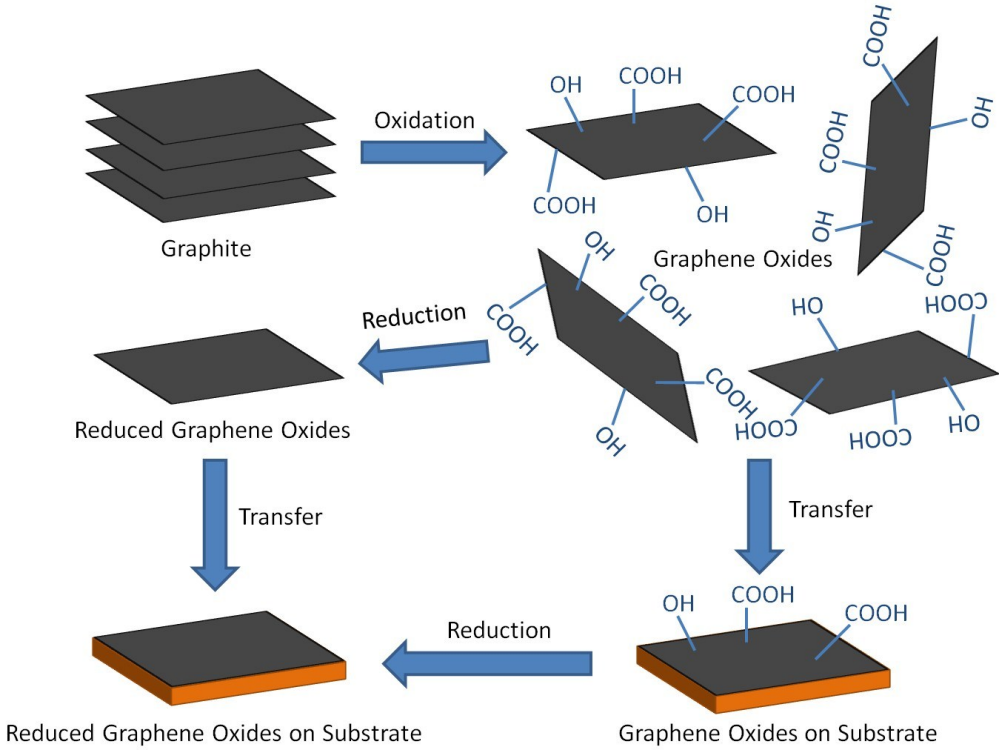

Figure 2-5: Schematic of Reduced Graphene Oxides Preparation

This solution-based method also uses graphite as initial carbon source, which provides a low-cost and large-scale preparation route. However the reduced graphene oxides

(RGO) is rendered with various structural defects, residual oxygen functional groups and contamination from solution (Figure 2-6) during the oxidation and reduction processes, leading to poorer electrical and mechanical properties in device applications.

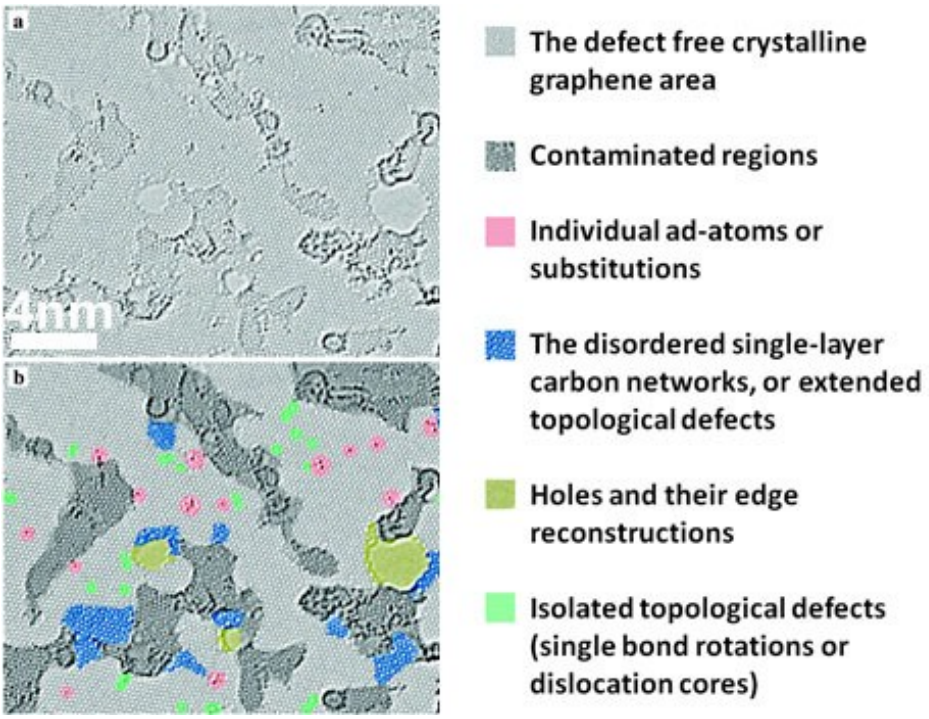

Figure 2-6: A typical high-resolution TEM image of a reduced graphene oxide sheet (single layer).

(a). the original TEM image. (b). the image with coloured marks of different types of defects / impurities. (Adapted from reference [26])

2.3 Epitaxial Growth

Epitaxial growth of graphene on SiC is achieved by a hybrid epitaxial-thermal decomposition process. [27; 28; 29; 30] By heating the silicon atoms off on the surface of SiC wafer at high temperature (1000–1600 °C), the remaining carbon atoms go through a graphitization process to form epitaxial graphene on the surface of SiC substrate. (Figure 2-7)

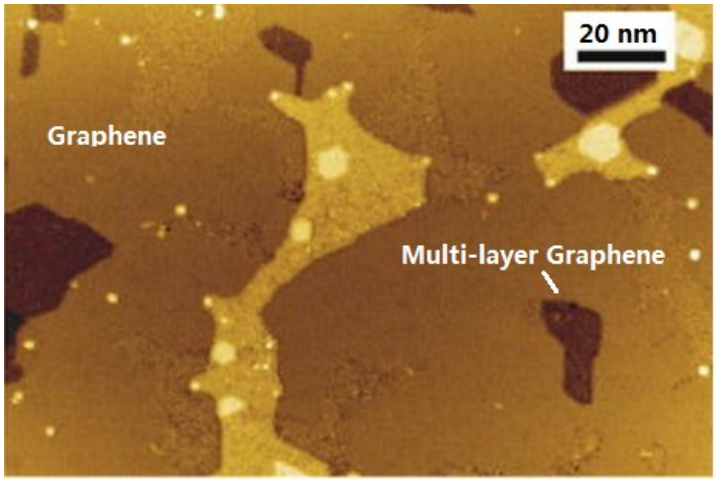

Figure 2-7: STM image of epitaxial graphene on SiC(0001) substrate

(Adapted from reference [28])

Due to the small mismatch of their hexagonal lattices and the uniform structure of the substrate crystal, large areas of high quality graphene films can be achieved. Furthermore, graphene grown on SiC can be directly used for electronic transport studies and related applications because SiC is highly resistive and will not shunt current flow through the channel, while graphene prepared by other methods like exfoliation and CVD method involves transferring the graphene sheets onto other insulating substrates. However, it is difficult to get mono- or bilayer graphene, or to detach graphene from its expensive substrates.

2.4 Chemical Vapour Deposition (CVD)

2.4.1 Introduction

Although many methods have been explored, a technological breakthrough in manufacturing high-quality monolayer graphene sheets on a large scale is still urgently needed. Since nowadays most of the commercial carbon nanotubes (CNTs), a one dimensional (1D) carbon material with structures similar to graphene, are produced by chemical vapour deposition (CVD), it is not surprising that CVD will also be a promising route to large scale production of single layer graphene. Recently mass production of graphene films on inexpensive transition metals such as Ni [31; 32; 33; 34; 35] and Cu [6; 36; 37; 38; 39] has been achieved. In the high temperature deposition process, these transition metals act as both the catalyst for hydrocarbon cracking and the growing substrate for graphene formation.

The growth mechanisms of graphene on Ni and Cu are different, due to the differences in solubility of carbon. According to the binary phase diagrams of C−Ni and C−Cu (Figure 2-8), the solubility of C in Ni is much higher than that in Cu. These mechanisms are studied and confirmed by carbon isotope labelling in conjunction with Raman spectroscopic mapping [40], which can track the carbon distributions during growth.

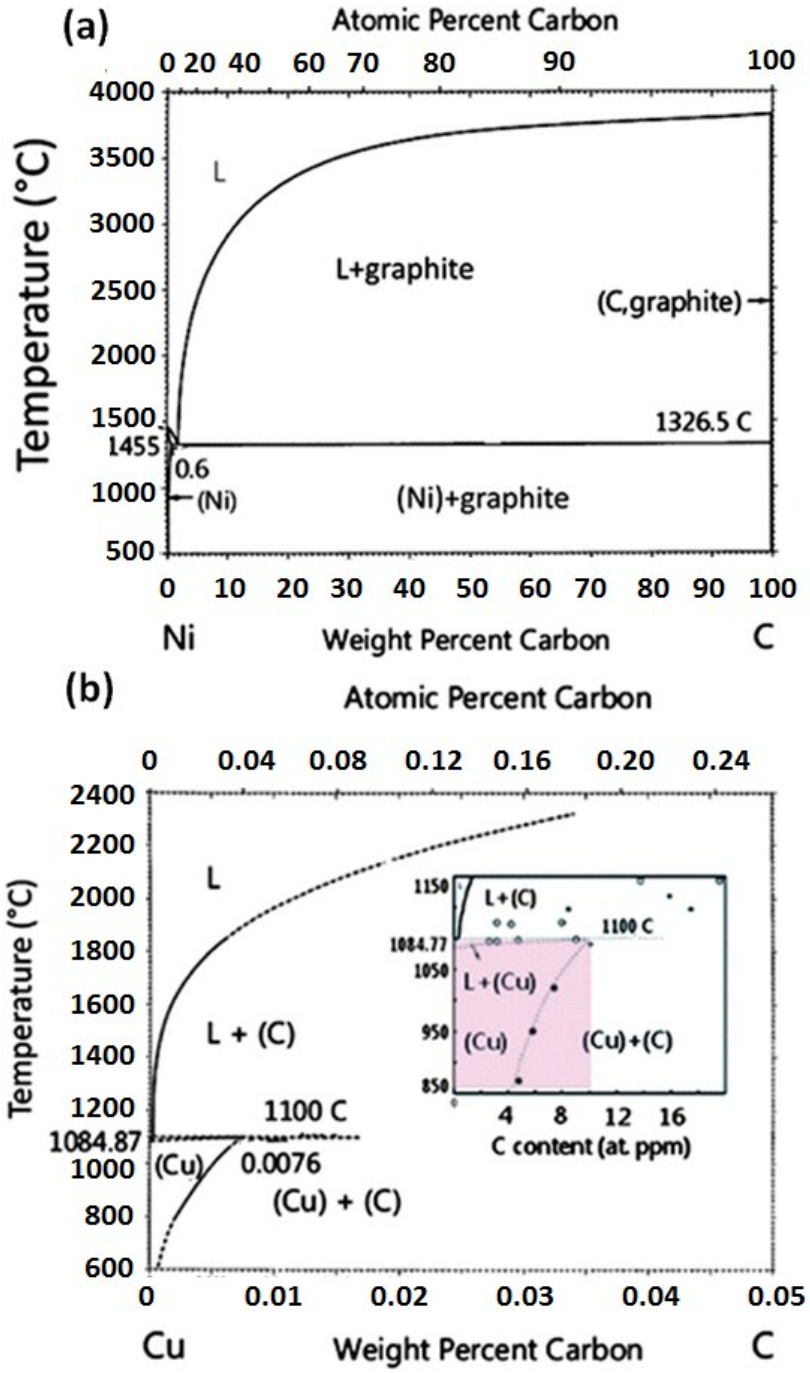

Figure 2-8: Binary phase diagrams of (a) Ni–C; (b) Cu–C

(Adapted from reference [41; 42] respectively)

In the case of Ni, during the high temperature process carbon atoms diffuse into the Ni substrate first, and then segregate and precipitate at the surface of the Ni substrate

to form graphene layers. Upon cooling, segregation occurs rapidly within the Ni grains, but slowly at the Ni grain boundaries. Due to the different rate of segregation of carbon from the metal carbide, nickel usually generates inhomogeneous graphene of 1-8 layers.

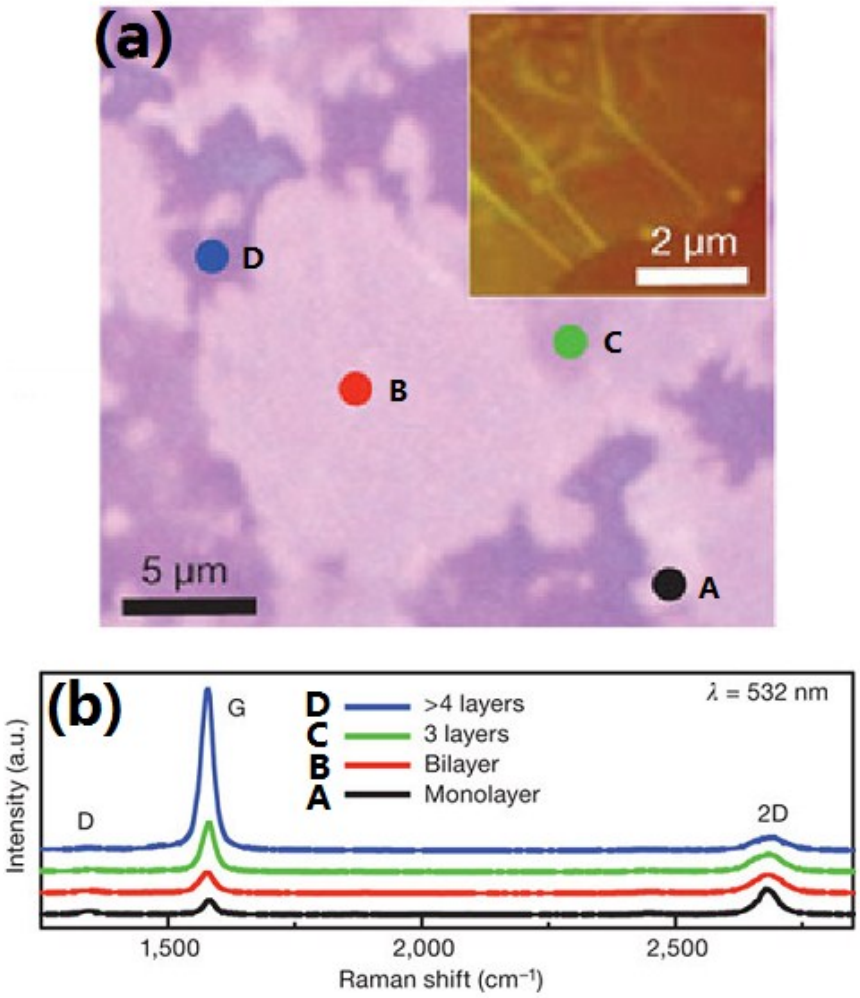

Figure 2-9: Optical image (a) (Insert: AFM image) and Raman spectra (b) of CVD graphene grown on Ni (Adapted from reference [31])

Cu, on the other hand, dissolves only a small amount of carbon during the high temperature process. Thus the graphene is mainly formed from the CH_4 gas source

which is decomposed by the catalytic Cu surface. The graphene growth stops automatically once the catalytic Cu surface is fully covered with carbon. Unlike CVD growth on Ni, Cu generates mostly mono-layer graphene (Figure 2-10). Moreover, Cu can be more easily removed by chemical etching, making it more simple and convenient to transfer graphene onto target substrates. The CVD growth of graphene on copper is further optimized and discussed in the next sections (2.4.2-2.4.4).

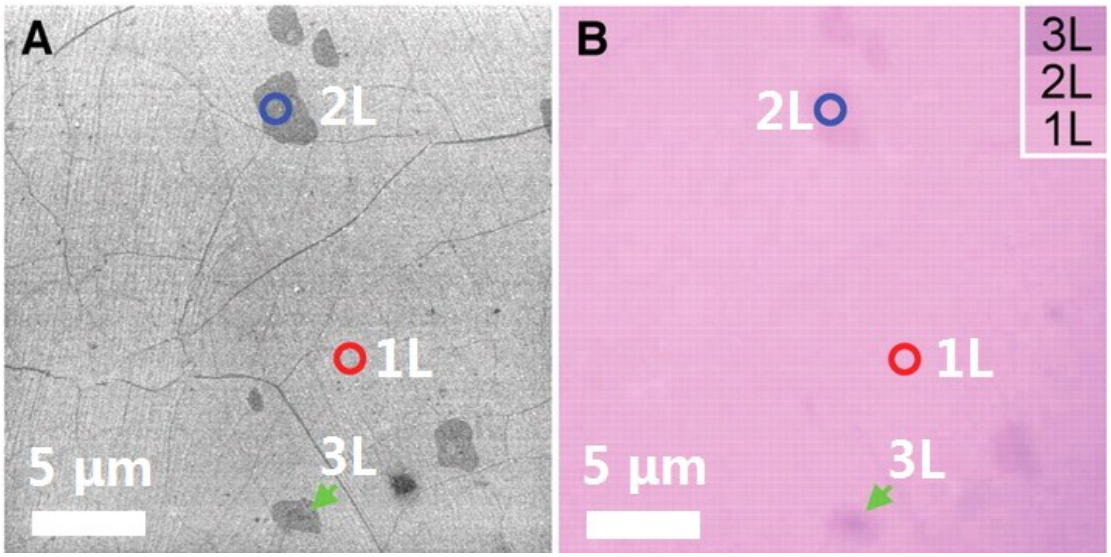

Figure 2-10 (a) A typical SEM image of CVD grown graphene on a copper foil (b) optical image of the same graphene transferred onto a SiO2/Si substrate (thickness of oxide layer: 285 nm) Adapted from reference [36].

2.4.2 Growth parameters (on copper)

Although many studies have been made to explore the CVD growth parameters (Table 2-2), there is still no commonly accepted recipe for best quality graphene. Typical CVD experiments are conducted at high temperatures (~1000 °C) in low pressure or

atmospheric pressure environment with CH_4 and H_2 as gas precursors. The optimum conditions vary with equipment, gases, substrates, and many other factors.

Paper	Temperature	Time	Pressure	CH_4/H_2 Ratio	Notes
[43]	1000 °C	20 min	450 mTorr	0.167	few-layer graphene
[44]	1000 °C	30 min	350 mTorr	2	Monolayer graphene
[45]	1000 °C	20 min	7.5 Torr	4	Monolayer graphene
[46]	1050 °C	10 min	-	0.00024	Discontinuous Graphene islands
[36]	1000 °C	30 min	500 mTorr	17.5	Monolayer graphene
[6]	1000 °C	30 min	460 mTorr	3	Monolayer graphene
[47]	1045 °C	15.5 min	Atmospheric pressure	0.001	Discontinuous graphene domains
[48]	850 – 900 °C	10 min	50 Torr	4	Few layers
[49]	950 °C	4 min	500 mTorr	Hexane (4mL/h)	1-2 layers

Table 2-2: A list of published CVD conditions for graphene growth. (1 Torr = 1.33 mBar = 133.322 Pa)

2.4.3 Transfer Process

A. Conventional Transfer

For many electronic or optical applications, it is necessary to transfer graphene from the copper where it grew on, to the specific target substrate. Conventional transfer method involve the following steps (Figure 2-11): (1) Spin coat a layer of PMMA film on the surface graphene / copper foil as support; (2) Etch away copper in solutions such as $FeCl_3$ or $(NH_4)_2S_2O_8$; (3) Dip the PMMA/Graphene film from solution and clean it in DI water bath several times to remove residues of etchant; (4) Scoop the PMMA/Graphene film with the target substrate and leave to dry; (5) Remove the PMMA film by annealing or acetone solution treatment.

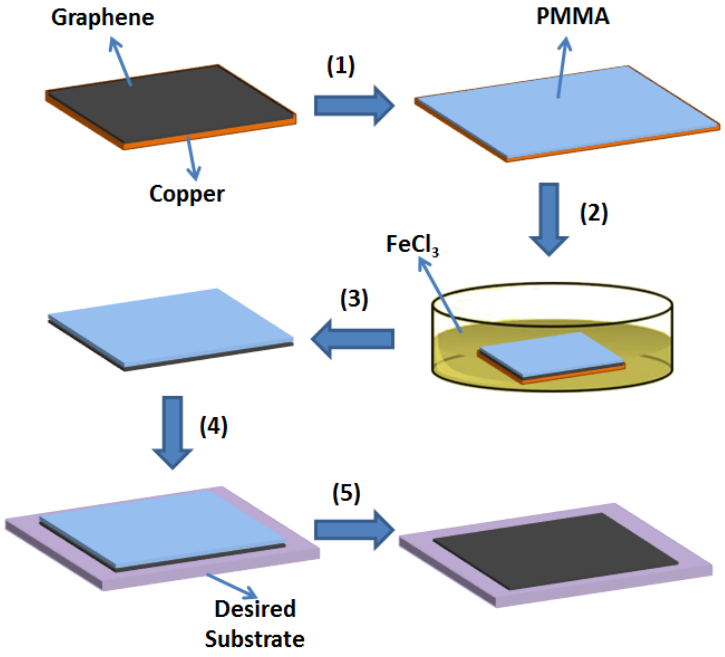

Figure 2-11: Schematic of graphene transfer process from copper to target substrate.

(1) Spin coating of PMMA film. (2) Remove copper in etchant solution. (3) Clean the film in DI water bath. (4) Scoop the film with target substrate. (5) Remove the PMMA support.

The conventional transfer method is an effective way to transfer graphene from copper to any target substrate; however, the process can cause ripples, holes and etchant residues which harm graphene performance. It is important to further optimize it to reduce defects.

B. Elastomer stamp transfer

J Song and colleagues [116] developed a general method which utilizes a polydimethylsiloxane elastomer stamp and a self-releasing polymer layer as transfer media to place graphene onto any target substrates, including flexible or hydrophobic ones. After detaching from the self-releasing layer, the elastomer stamp can be reused for other transfers. Figure 2-12 illustrates the detailed elastomer stamp transfer procedures.

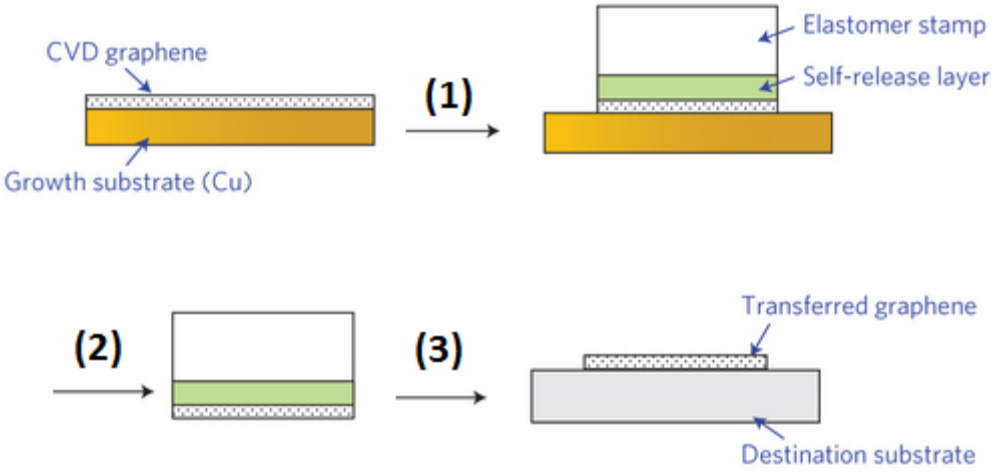

Figure 2-12: Schematic of the elastomer stamp transfer method. (1): Contact with the self-releasing polymer layer and elastomer stamp; (2): etching of copper substrate; (3): Transfer onto target substrate and remove the self-releasing polymer layer

(Adapted from reference [116])

C. Roll to roll transfer

Sukang Bae and colleagues have developed a new roll to roll transfer technique to get 30-inch large graphene film from copper onto a flexible PET substrate. [6; 50] The CVD synthesized graphene was firstly attached to a polymer support (thermal release tape) and then immersed into etchant to remove copper. Graphene was then transferred onto the flexible target substrate after detachment from the polymer support. This technique is especially promising due to its possibility to be part of an integrated graphene production line.

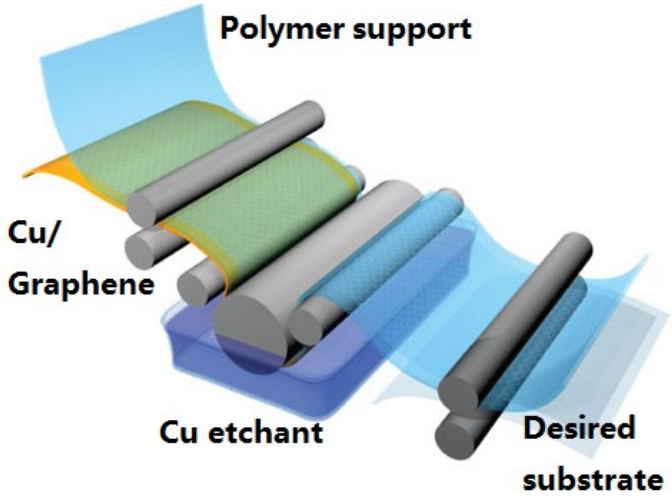

Figure 2-13: Schematic of the roll to roll transfer process
(Adapted from reference [6; 50])

D. Electrochemical Delamination

Some groups have been exploring a novel electrochemical delamination to separate

graphene without the need to etch away all the metal catalyst [51; 52; 53]. Unlike conventional transfer process in which solutions such as $FeCl_3$ etch away the copper, the novel electrochemical delamination method utilizes the hydrogen bubbles emerging at the graphene/Cu interfaces ($2H_2O + 2e^- \rightarrow H_2 + 2OH^-$) to achieve graphene–copper separation. The delaminated graphene/PMMA film is then transferred onto the target substrate, after which the supporting PMMA is removed. (Figure 2-14)

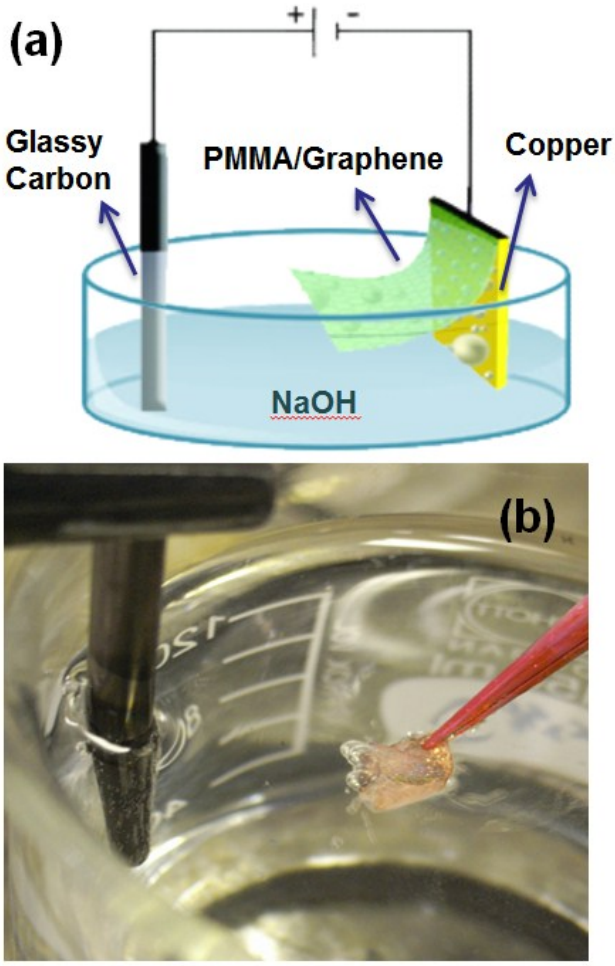

Figure 2-14: Schematic (a) and photo (b) of the electrochemical delamination process.

Although the Electrochemical delamination technique offers a more effective way to separate graphene from copper and the possibility of reuse of the growing catalytic metal, the bubbles can leave holes in the resulting graphene films during the process which need to be carefully studied and minimized. (Table 2-3)

Transfer Method	Chemical Etching	Electrochemical delamination
Separation time	1-20+ hours	1-60 minutes
Graphene Surface	Contaminated by ion residues from the etchant	Clean, free from solution impurities
Chemical Solution	Can be reused several times	Can be reused hundreds of times
Growing substrate	Etched away	Can be recycled and reused hundreds of times.
Graphene surface	More complete	Holes caused by bubbles

Table 2-3: Comparison of the conventional chemical etching method and the electrochemical delamination method.

2.4.4 CVD growth of graphene on copper thin films

Although the traditional transfer method involving PMMA / thermal release tapes can achieve detachment from copper foil, the process normally brings considerable contaminations and damages to graphene films. Many groups are exploring CVD growth of graphene on copper thin films [54; 55; 56; 57] instead of foil, because it can be easily evaporated, etched away or peeled off.

Ariel Ismach, et al [55] found that the copper films would de-wet and evaporate during or immediately after long period of high temperature CVD growth, leading to graphene on the bare dielectric substrates such as quartz without the need of additional transfer processes (Figure 2-15). However, there are still copper residues underneath the graphene layer (Figure 2-15), and thus impair the quality of synthesized graphene.

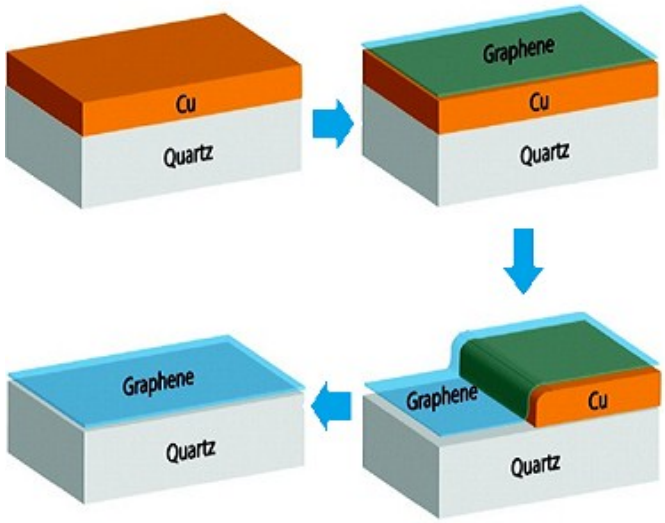

Figure 2-15: Schematic of the transfer-free process in reference (Adapted from reference [55])

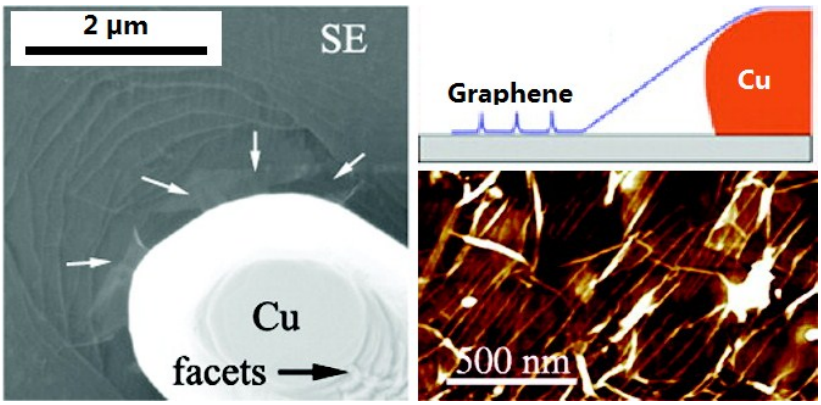

Figure 2-16: SEM image (left, secondary electron mode) and AFM image (right) of the CVD grown graphene and remaining copper underneath. (Adapted from reference [55])

Mark P. Levendorf and colleagues developed a fabrication method to directly pattern graphene sheets grown on copper films into devices [56]. As shown in Figure 2-17, the deposited protective photoresists was first patterned by photolithography, followed etching away all the underlying copper film, after which the protective photoresists are removed.

CVD growth of graphene on copper is promising for microelectronics as the device fabrication is compatible with conventional thin film processing techniques. However, due to the high temperature conditions (> 800 °C) during CVD growth, the copper evaporation is significant and leaves holes in the film (Figure 2-18). Thus it is not suitable for growing mm^2 scale continuous graphene films. Plasma Enhanced CVD (PECVD) method can reduce the growth temperature to ~750 °C and obtain continuous films. [58; 59; 60; 61; 62] Due to lack of facilities, graphene growth is only conducted on copper foils in this thesis.

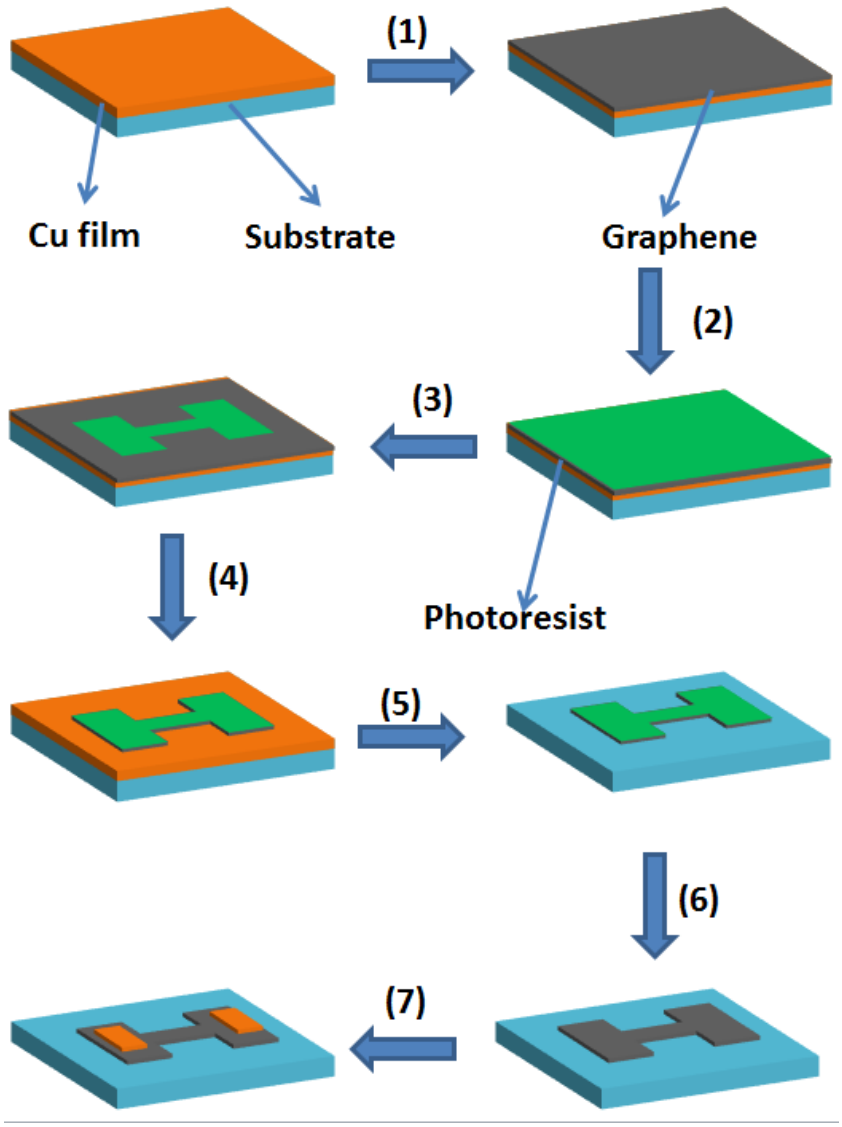

Figure 2-17: Schematic of the transfer-free process in reference (1): Graphene Growth. (2): Spin photoresist. (3): Pattern photoresist. (4): Reactive-ion etching (RIE) of unprotected graphene. (5): Etching away copper film. (6): Strip photoresist. (7) Deposit top-electrode. (Adapted from reference[56])

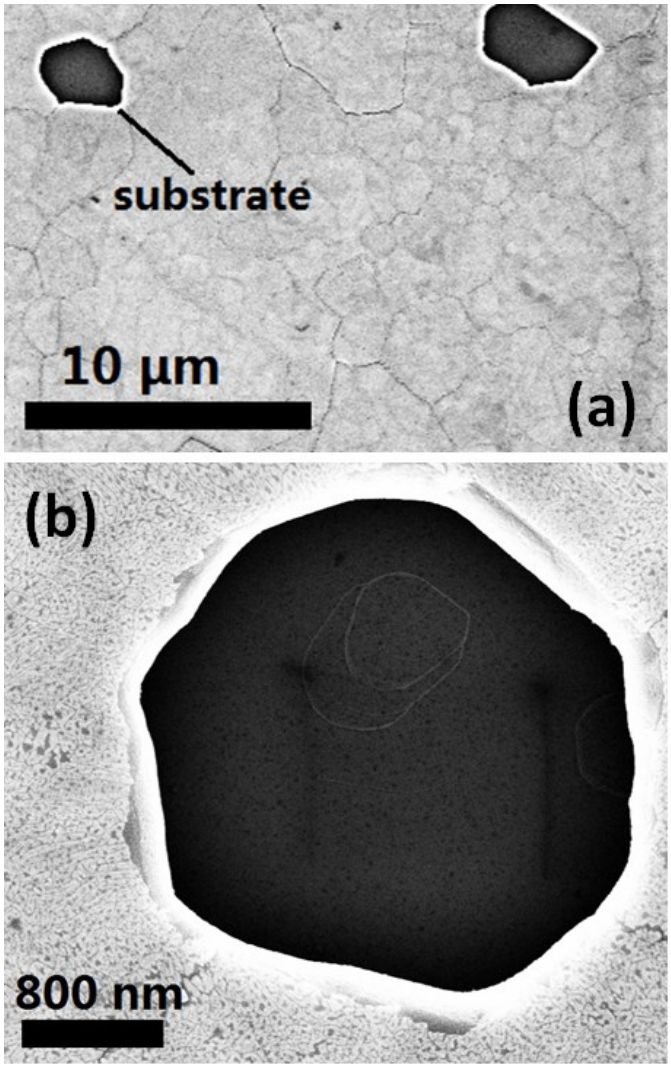

Figure 2-18: SEM images of copper film after CVD growth. Holes are formed in the copper film as a result of evaporation during the high temperature process.

2.4.5 Summary

CVD growth of graphene on copper is one of the most promising mass production methods for high-quality graphene: Graphene production has been scalable to areas of up to ~0.1m^2 [6]; with the possibility of integration into production line through the

CVD mass production and the roll to roll mass transfer techniques; and competitive low cost.

However, due to the polycrystalline nature and various kinds of defects, the electron mobility of CVD-grown graphene is still two orders of magnitudes lower than graphene fabricated by mechanical exfoliation. Much work still needs to be done to further improve the quality and minimize defects.

2.5 Decomposition from other Solid Carbon Sources

Although CVD growth of graphene on copper shows great promise for industrial applications, the high processing temperature as (~1000°C) and the use of organic carbon gases are still two limitations. Z Sun and colleagues developed a novel method to turn solid carbon-containing materials into graphene, with metals as catalysts [63].

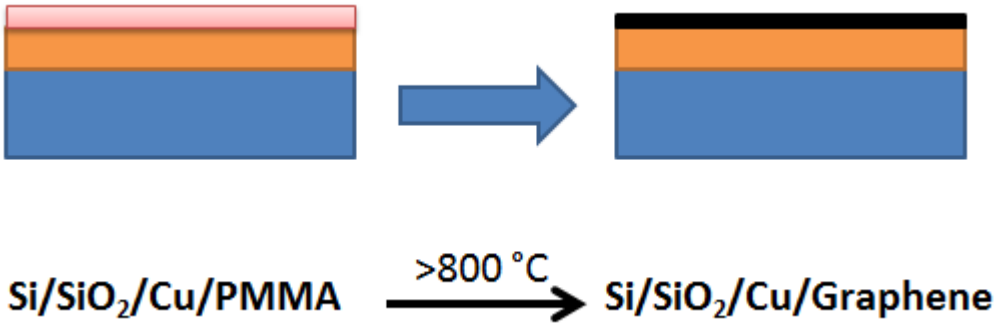

Figure 2-19: Schematic of graphene preparation from PMMA

(Adapted from reference [63])

As shown in Figure 2-19, the solid carbon source, which ranges from fluorene ($C_{13}H_{10}$), poly(methyl methacrylate) (PMMA) and (table sugar, $C_{12}H_{22}O_{11}$), was firstly spin-coated on a Cu thin film catalyst. Uniform graphene sheets were formed on the SiO_2/Si substrates at a temperature between 800 °C and 1,000 °C for a short period of time, under low pressure vacuum conditions with a reductive H_2/Ar gas flow. The authors were also able to selectively grow only monolayer graphene by adjusting the hydrogen flow rate and growth to suppress the growth.

Compared to CVD growth of graphene on copper, this method only requires a temperature of 800 °C, compared to 1000 °C in CVD. This lower processing temperature is more favourable for the fabrication of heterostructure devices in the semiconductor industry. Other solid carbon sources, such as fluorene ($C_{13}H_{10}$) and sucrose ($C_{12}H_{22}O_{11}$), have also been used to grow graphene in similar conditions. However, as these carbon sources all contain other elements like oxygen, sulphur, nitrogen or phosphorus, it is difficult to produce pure graphene products without impurities.

2.6 Comparisons of different graphene synthesis methods

In summary, each method has its own advantages and disadvantages (Table 2-4): mechanical exfoliation offers the best quality graphene samples, however the lack of control over size and number of layers, as well as the inconvenience for mass production make it only applicable for laboratory research. Although chemical exfoliation improves the exfoliation efficiency, it still does not achieve control of size

and number of layers. Epitaxial growth can generate relatively high quality graphene on SiC, the expensive cost of epitaxial substrate and lack of flexibility on substrate make it difficult for industrial production. Reduction of graphene oxides can produce graphene in large quantities; however numerous defects are introduced during the oxidation and reduction processes. Chemical vapour deposition and decomposition from solid carbon source can produce monolayer graphene on a large scale, however the quality needs to be further improved.

	Mass Production	Monolayer	Size	Quality	Cost	Transfer
Mechanical exfoliation	N	Uncontrollable	Uncontrollable	Highest	High	Y
Chemical exfoliation	Y	Uncontrollable	Uncontrollable	high	Low	Y
Reduction of graphene oxides	Y	Uncontrollable	Uncontrollable	Very low	Low	Y
Epitaxial growth	Y	Uncontrollable	Large	High	Very high	N
Decomposition from solid carbon source	Y	Yes	Large	Low (with impurities)	Low	Y
Chemical vapour deposition on Ni	Y	N	Large	Low	Low	Y
Chemical vapour deposition on Cu	Y	Yes	Large	Low	Low	Y

Table 2-4: comparisons of major graphene synthesis methods

To produce uniform monolayer graphene at reasonable cost, chemical vapour deposition on copper appears to be the most promising way for industrial applications. Chapter 4 and 5 explore the CVD synthesis and transfer of graphene in detail and bring up some modifications to obtain graphene with better quality.

3. Experimental Techniques

This chapter describes the major fabrication (section 3.1) and characterization techniques (section 3.2) which are utilized in this thesis.

3.1 Fabrication Techniques

3.1.1 Chemical Vapour Deposition (CVD)

Chemical vapour deposition (CVD) is a material processing process which involves chemical reactions of gas precursors to deposit high quality solid materials (0-D nanoparticles, 1-D nanowires / nanotubes and 2-D plates / films). [64]

In a typical CVD experiment, the substrate is located in the middle of a tube furnace or vacuum chamber. Additional catalysts and high temperature treatment might be needed to enable the reaction of volatile precursors to react on the surface of the substrate. For materials which are sensitive to oxygen, high vacuum environment and inert carrier gases like Ar are introduced to protect the products from oxidation. (Figure 3-1)

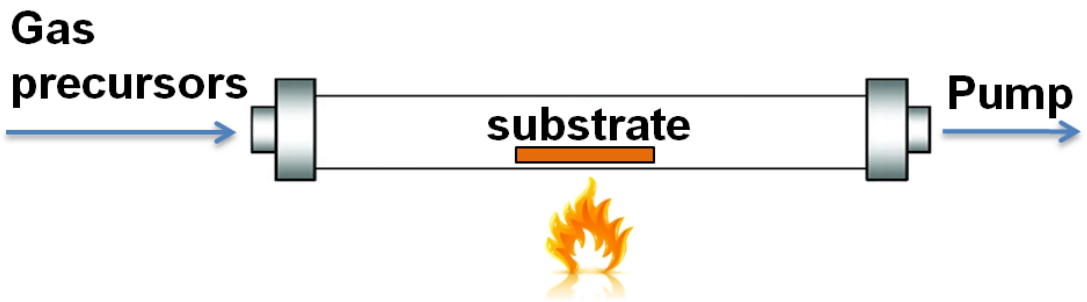

Figure 3-1: Schematic of a typical CVD system

The CVD method can be classified into three categories: atmospheric pressure CVD (APCVD), low-pressure CVD (LPCVD, <1 Torr) and ultra-high vacuum CVD (UHVCVD, normally < ~10^{-8} Torr), according to its operating pressure (gas pressure).

For materials which are not favourable for a high temperature process, Plasma Enhanced CVD (PECVD) method is also utilized to enhance the reactions and to reduce the reaction temperature[58; 59; 60; 61; 62].

In this thesis, LPCVD is utilized to grow large-area high quality graphene films, more details of which can be found in Chapter 3.

3.1.2 Pulsed laser deposition (PLD)

Pulsed laser deposition (PLD) is a physical vapour deposition process which utilizes high-power pulsed lasers to strike (vaporize) material atoms from the target and to deposit onto the substrate as films.[65] (Figure 3-2)

Although PLD is normally conducted in ultra-high vacuum chamber, oxygen is introduced as a background gas when depositing oxide films. In this thesis, PLD is utilized to deposit Strontium Titanate (STO) films onto graphene, more details of which can be found in Chapter 5.

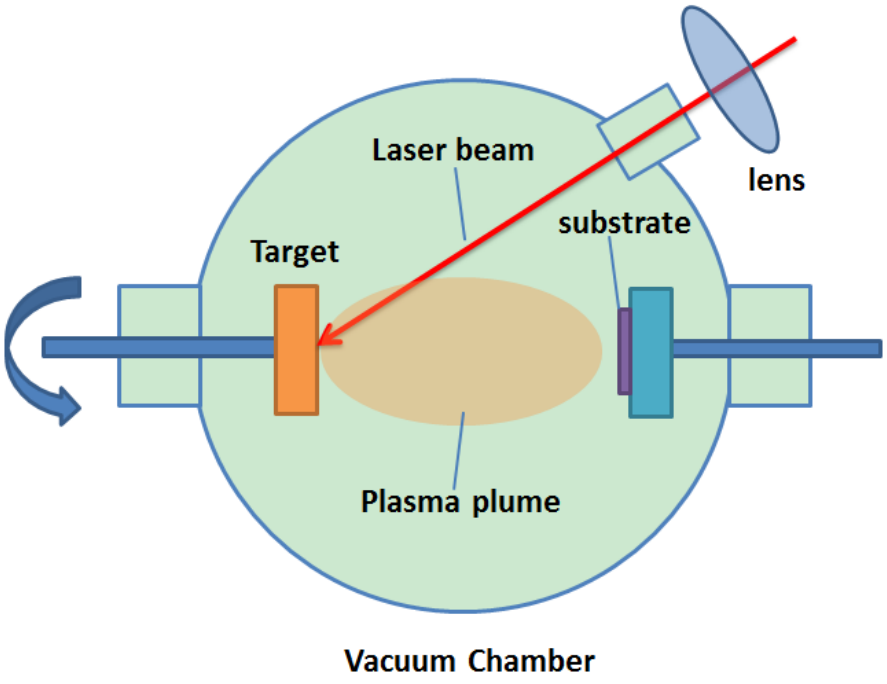

Figure 3-2: Schematic of a typical PLD system

(adapted from reference [65])

3.1.3 Spin coating

Spin coating is a thin film deposition technique which utilizes rotation to spread fluids of materials into homogenous films of certain thickness on a flat substrate. [66]

In a typical environment, the deposition material is dissolved and diluted in solvent to form fluids, drops of which are placed on a target substrate which is sucked in the middle of a spin coater by vacuum. The coater then spins at a given rotation speed and period until the desired thickness is achieved. After deposition, the substrate is normally left to dry or baked to solidify the film and remove any remaining solvent. (Figure 3-3)

In this thesis, spin coating is mainly utilized to deposit PMMA film in graphene

transfer.

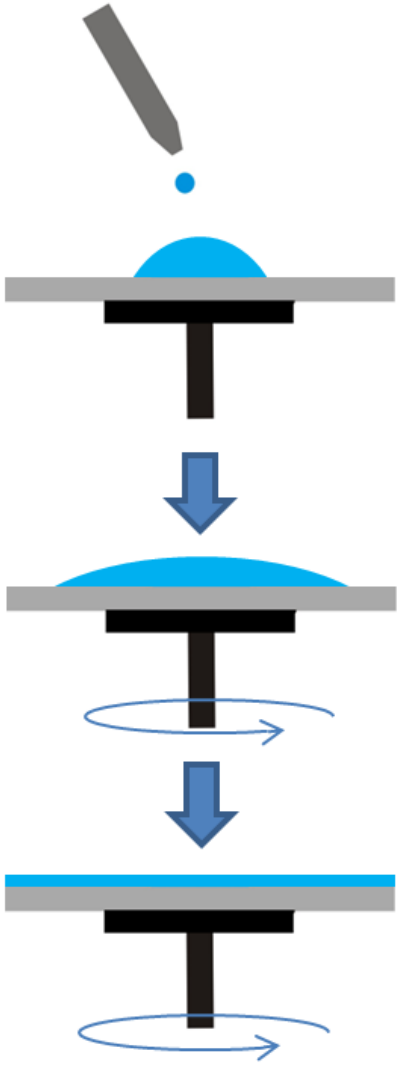

Figure 3-3: Schematic of a typical spin coating process

3.1.4 Photolithography

Photolithography is a conventional fabrication process which utilizes photomask and UV light to pattern thin films or substrates [117]. As shown in Figure 3-4, after exposed

to a UV light, the pattern from a photomask is transferred to the photoresist which was pre-coated on the surface of substrate. The UV light causes a chemical change in the exposed photoresist, making it soluble (positive photoresist) or insoluble (negative photoresist) in the developer solution. After development, the underlying film or substrate is etched, after which the remaining photoresist is stripped away.

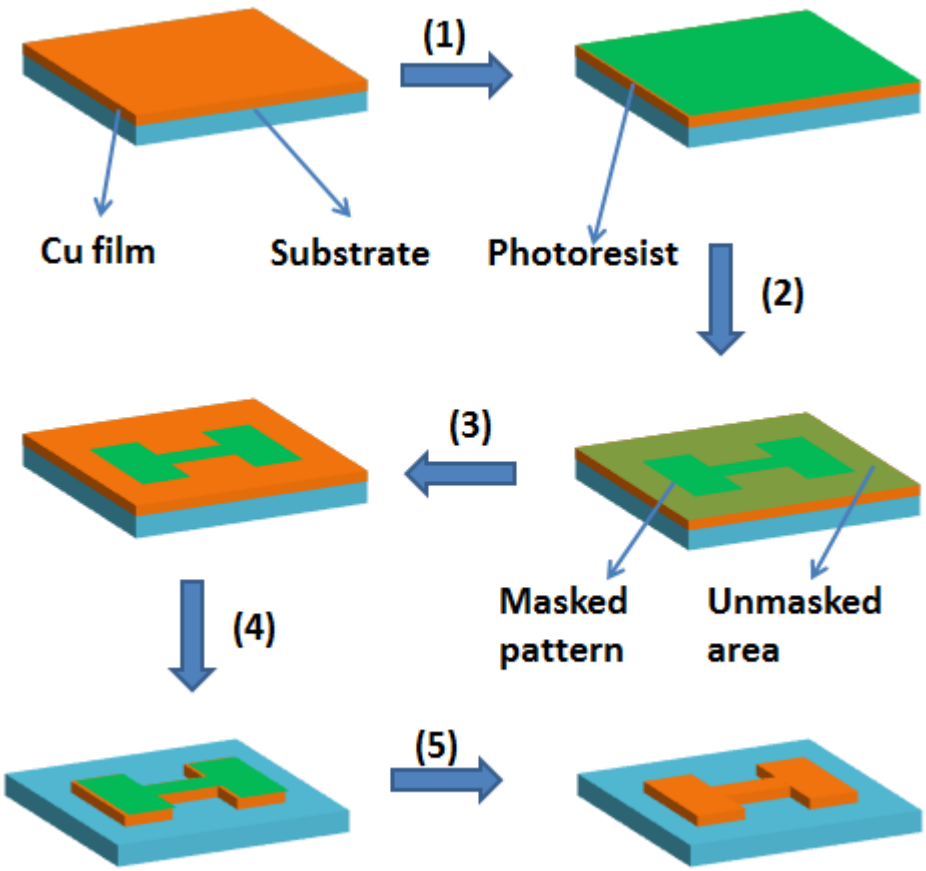

Figure 3-4: Schematic of the photolithography process. (1): spin photoresist; (2): expose; (3): develop; (4): chemical etching of copper; (5): strip photoresist.

3.2 Characterization Techniques

3.2.1 Optical Microscope

The optical microscope, or light microscope, is widely used as a convenient characterization tool in areas such as biology and materials science. With the help of lenses and a light source, microstructures of samples can be observed through magnified images. (Figure 3-5)

As monolayer graphene is nearly transparent (only 2.3% light absorption[8]), it is difficult to observe graphene directly with an optical microscope. However, it is found that on top of SiO_2/Si substrate (Si substrate with ~300 nm SiO_2 layer), graphene can be more visible due to a slight interference-like contrast difference. [67; 68]

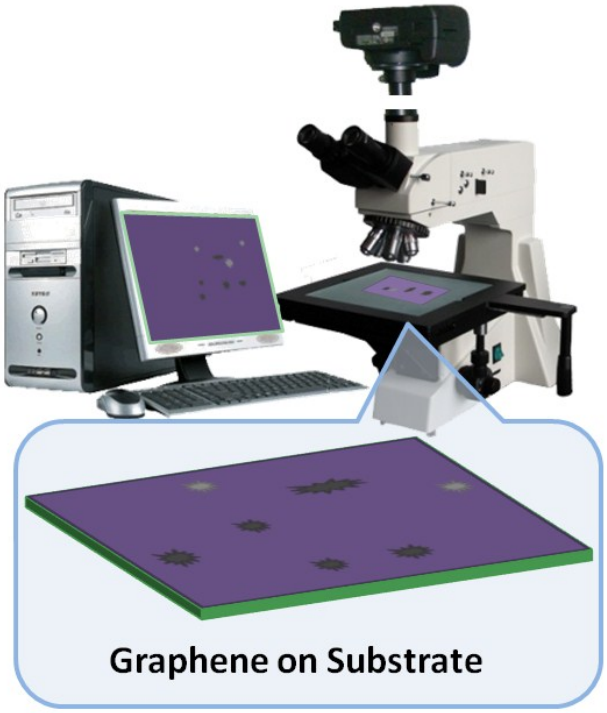

Figure 3-5: Schematic of a typical optical microscope characterization of graphene film.

Although the most direct method to determine number of graphene layers is still atomic force microscopy (AFM), the low efficiency and damage to graphene samples makes AFM less popular in graphene characterizations. In fact, this colour contrast observation under optical microscope has become a convenient and common–accepted way to identify the different numbers of graphene layers [69] (Figure 3-6), which can be further verification with Raman spectra (see section 3.2.2 Raman for more details). This greatly facilitates the characterization and device fabrication processes of graphene.

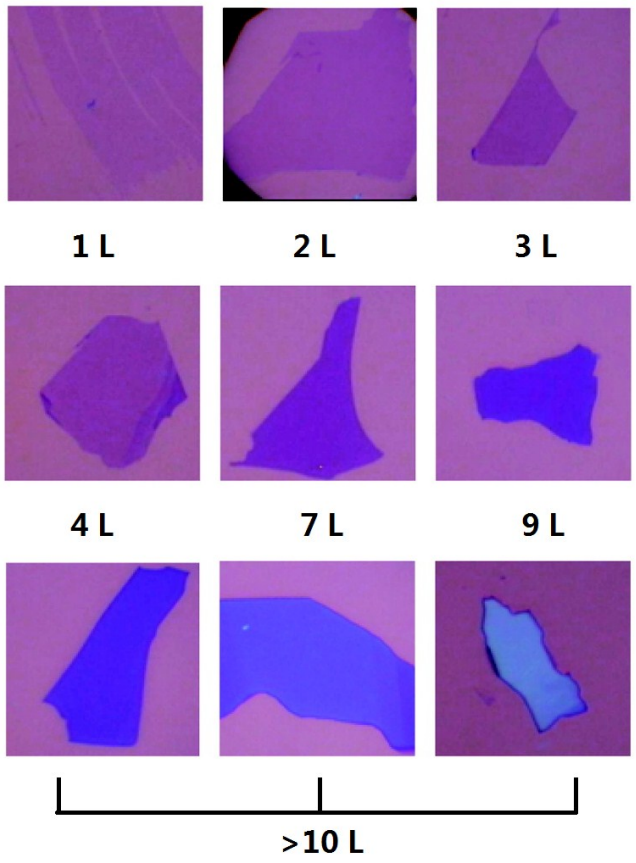

Figure 3-6: Optical image of graphene with different number of layers on Si SiO_2/Si substrate (thickness of oxide layer: 285 nm)

(Layer numbers are listed below each image. Adapted from reference [69])

3.2.2 Raman Spectroscopy

Raman spectroscopy is a spectroscopic characterization technique which identifies molecules through information on inelastic scattering. Photons from the laser light can excite the tested molecule from a ground state (vibrational state) to a virtual state, after which the molecule drops back to a different ground state and emits a photon with a frequency shift due to the energy difference. These shifts in frequencies can be recorded and analysed to obtain information about vibration modes of corresponding chemical bonds in the molecule. [70] (Figure 3-7)

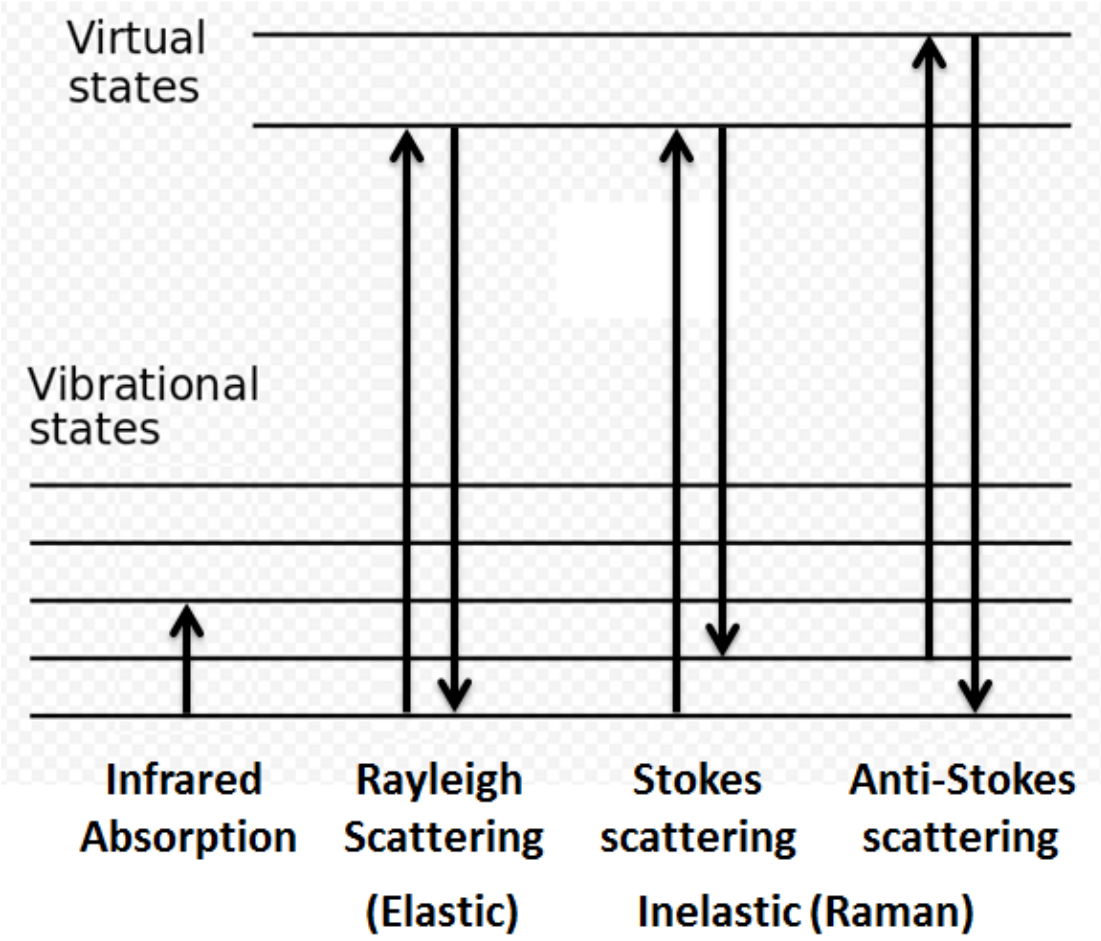

Figure 3-7: Energy-level diagram of different scatterings.

(Adapted from reference [70])

Raman spectroscopy is very sensitive to symmetric carbon-carbon bonds, and thus is a powerful tool in characterizing various carbon materials. Figure 3-8 shows typical Raman spectra of several carbon materials: Graphene, graphite, single-wall carbon nanotube (SWCNT), multi-wall carbon nanotube (MWCNT). [71] The G band (around 1582 cm^{-1}) corresponds to planar sp^2 bonded carbon in graphene, graphite and carbon nanotubes. The D band (around 1350 cm^{-1}) corresponds to sp^2 carbon rings (i.e. defects in sp^2 carbon) and is often regarded as an indicator for defects: its intensity is proportional to the degree of defects in materials with sp^2 carbon. The 2D (G') band (around 2685 cm^{-1}) is the second order of the D band, and typically used to infer the number of graphene layers: although some groups claim that the intensity ratio of G/2D bands can be utilized to identify number of layers (Figure 3-9), the more reliable indicators for the layer number are the shape and position of 2D band (in bilayer or multi-layer graphene, the 2D band is a merged result of components from different layers). [69; 71; 72; 73]

In this thesis, Raman spectroscopy is extensively used for determining the number of graphene layers and structural defects in graphene.

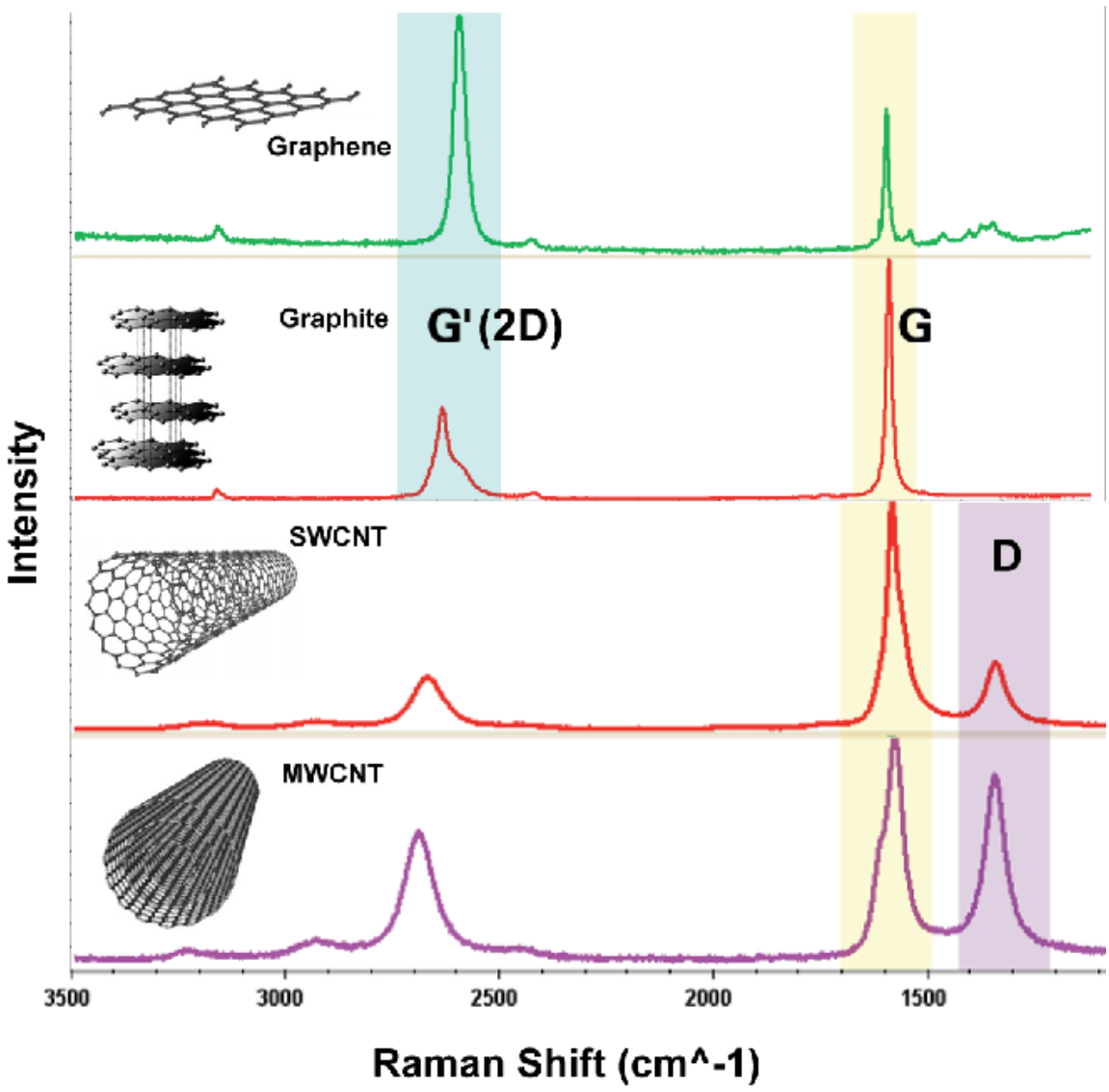

Figure 3-8: Typical Raman spectra of several carbon materials.

Graphene, graphite, single-wall carbon nanotube (SWCNT), multi-wall carbon nanotube (MWCNT) (Adapted from reference [71])

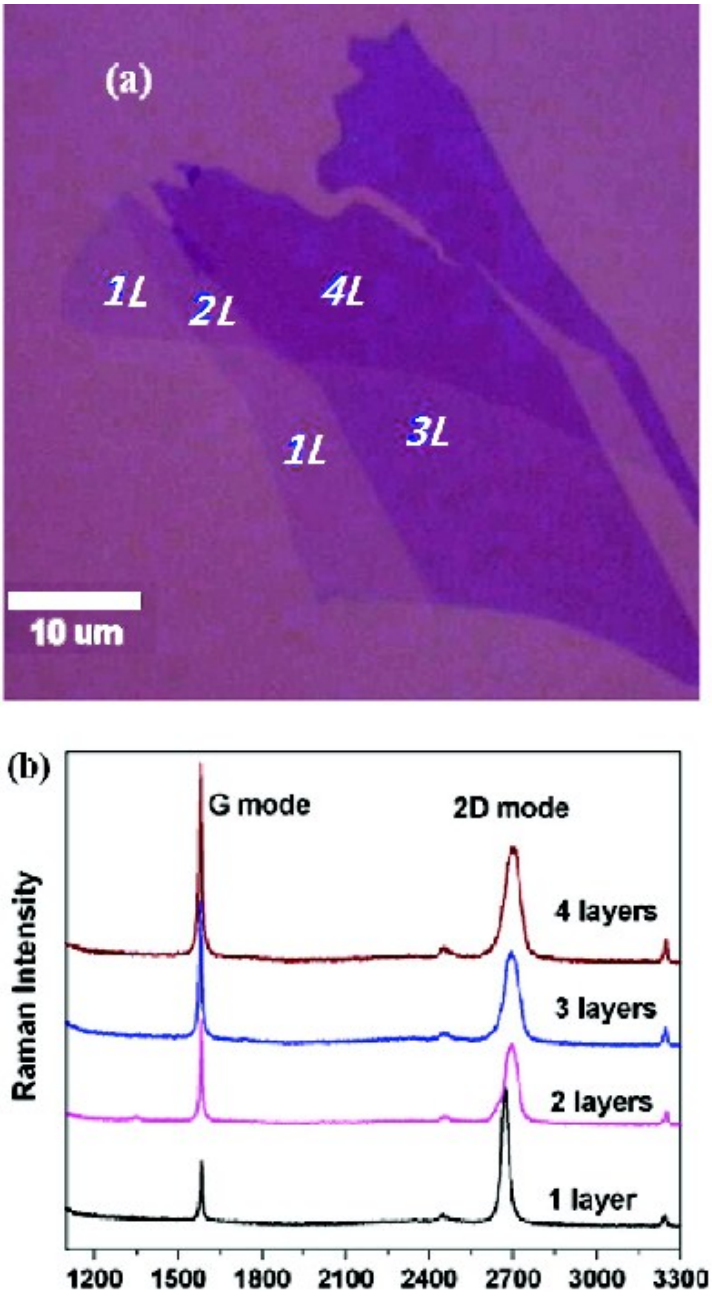

Figure 3-9: Raman spectra of mechanical exfoliated graphene.

(a) Optical image of mechanical exfoliated graphene with 1 - 4 layers. (b) Corresponding Raman spectra (Adapted from reference [69])

3.2.3 Scanning Electron Microscope (SEM) and Energy-dispersive X-ray spectroscopy (EDX)

Scanning electron microscopy (SEM) is a common materials characterization technique which scans a focused electron beam on a sample to reveal its topography and composition information. [74; 75] The incident electron beam will interact with atoms in the test sample, which then releases a range of signals which can be detected, analysed and imaged. (Figure 3-10)

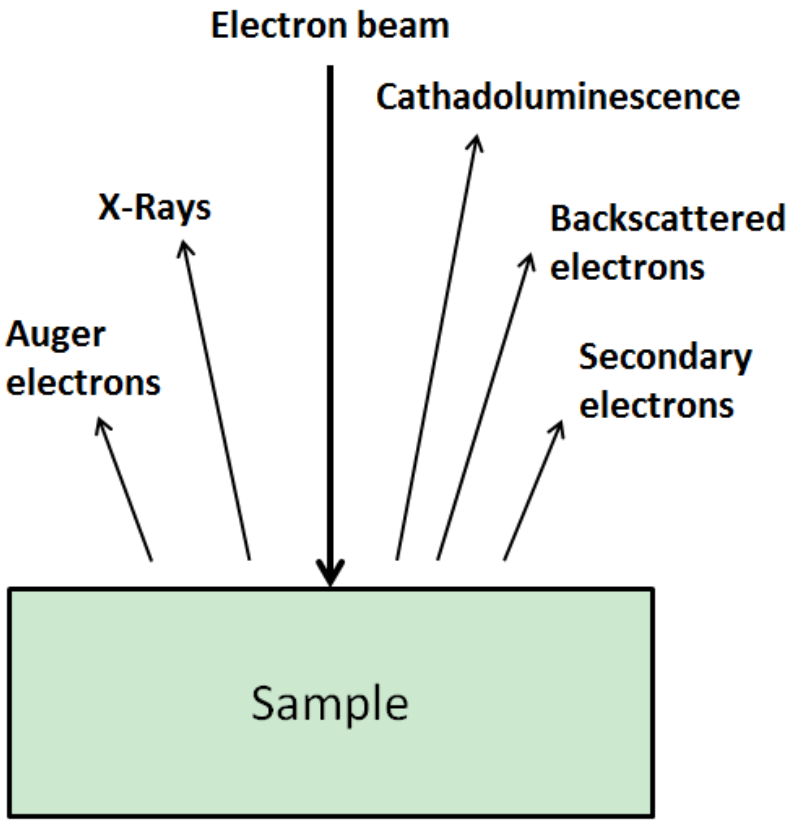

Figure 3-10: Output signals in scanning electron microscope.

(adapted from reference [74])

SEM is a convenient way to characterize graphene, especially direct imaging of CVD grown graphene on copper without transfer. Due to the blockage effect of secondary electrons (SE) [76] (Figure 3-11), graphene appears to be in darker contrast in SEM images (Figure 3-12).

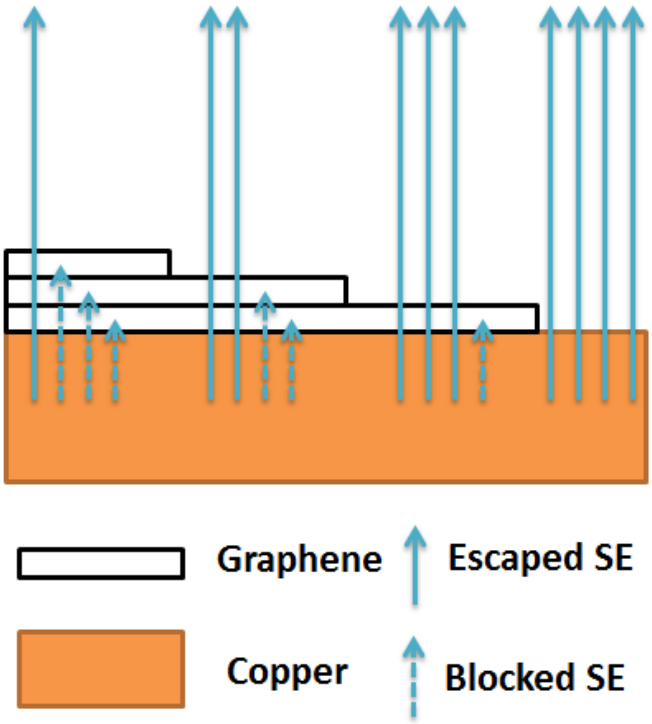

Figure 3-11: Schematic of emitted secondary electrons (SE) blocked by graphene

(adapted from reference [76])

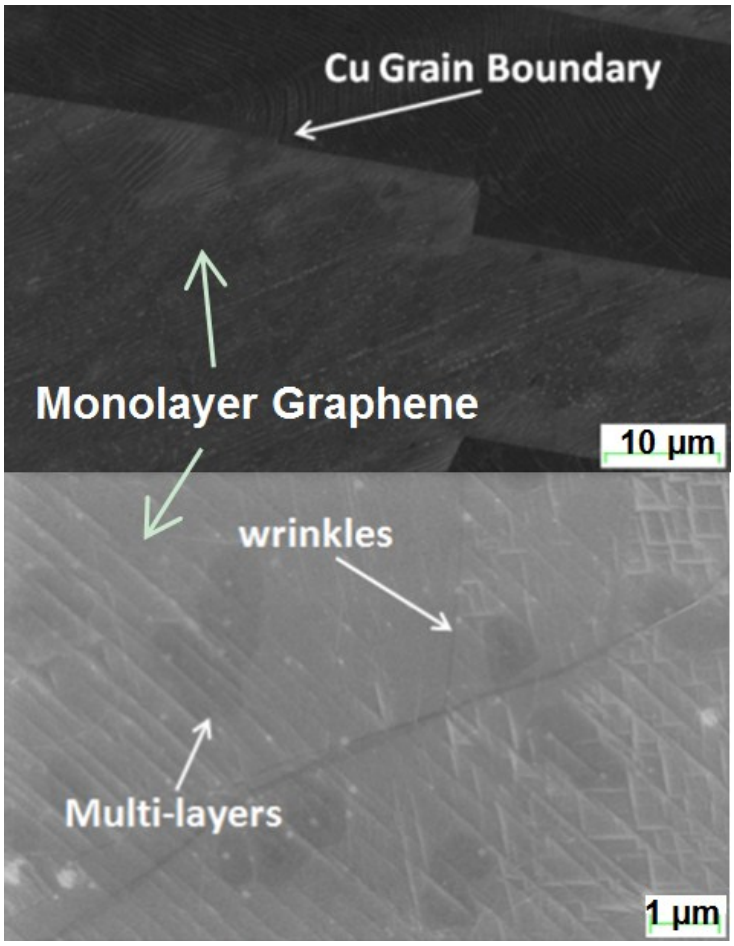

Figure 3-12: Typical SEM images of CVD grown graphene on a copper foil.

All the original SEM images (unless those adapted from references) in the thesis are taken with the LEO Gemini 1525 SEM in Department of Materials, Imperial College London.

The energy-dispersive spectrometer in the SEM can also capture the emitted X-rays. By analysing the number and energy of these characteristic X-rays, information on elements in the sample can be revealed.[75] This elemental analysis technique is called Energy-dispersive X-ray spectroscopy (EDX). EDX is utilized to analyse the impurity particles on graphene films in chapter 4.

3.2.4 Electrical Measurement (Four-Probe Measurement)

To determine the electrical property (sheet resistance) of synthesized graphene, four-probe measurement is conducted on various graphene samples. As shown in Figure 3-13, the current is supplied through two probes while the voltmeter measures the voltage across the other two probes. The probe spacing *s* used in this experiment is 0.635 mm.

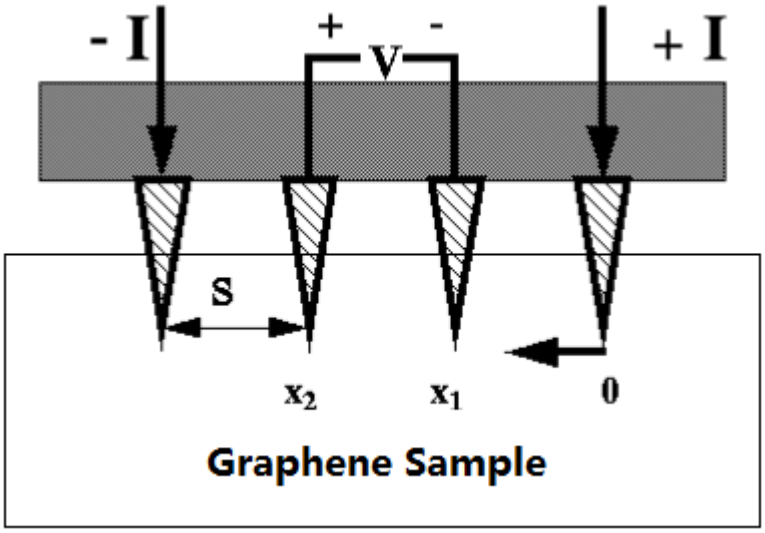

Figure 3-13: Schematic of 4-point probe configuration

(adapted from reference [77])

The sheet resistance of graphene can be calculated as:

$$Rs = \frac{\pi}{ln2} \times \frac{V}{I} = 4.53 \frac{V}{I} \quad \text{(Equation 3-1)}$$

(From reference[78], see Appendix 8.1 for more details about the derivation of this equation.)

The four- probe method is a more accurate way to measure sheet resistance than the two-probe method, as it can eliminate factors such as probe resistance and contact resistance.

4. CVD Synthesis and Transfer of Large-area Graphene Films[2]

This chapter explores the synthesis and transfer techniques to obtain cm^2-size continuous graphene film. Different growth and transfer parameters are explored and optimized to ensure the continuity and quality of the resulting monolayer graphene over the whole substrate (10×10 mm^2).

4.1 The CVD Process

4.1.1 The CVD System

In this PhD project, a home-made LPCVD system was designed and set up for graphene growth (Figure 4-1).

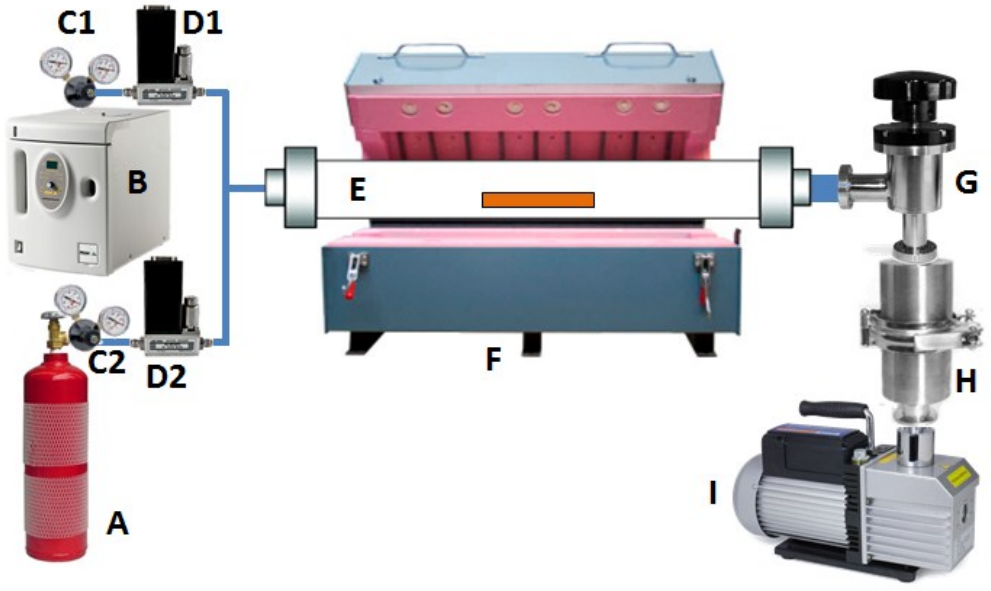

[2] Part of this chapter has been published in Kai Wang, Cecilia Mattevi, et al. (2012). Hydrogen Etching Effect in Chemical Vapour Deposition of Graphene on Copper (Poster Presentation). E-MRS 2012 SPRING MEETING. Strasbourg, France.

Figure 4-1: Schematic of CVD system for graphene growth

A: Methane gas cylinder, providing methane precursors.

B: Hydrogen generator (PH200-220 from peak scientific), providing high purity hydrogen (99.9995) by electrolysis of water. It is safer as a gas source than conventional hydrogen gas cylinders.

C1 and C2: gas regulators, controlling the pressure of output gases.

D1 and D2: mass flow controllers, modulating the flow rates for different gases.

E: Quartz tube: the container for CVD synthesis.

F: Horizontal split tube furnace (THH11 from Elite Thermal Systems Ltd), heating up to 1100 °C.

G: Angle valve: modulating the pumping rate / pressure of the system.

H: Trap, protecting the pump from contaminations.

I: Rotary vacuum pump.

4.1.2 The CVD Procedures

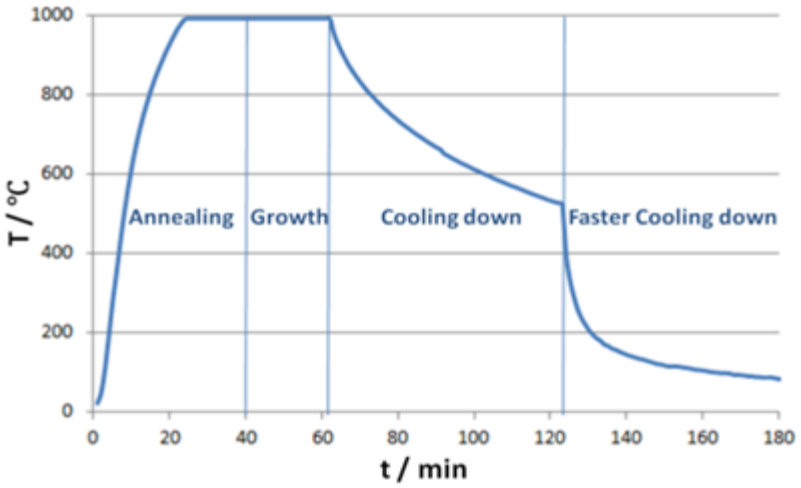

Figure 4-2: Schematic of the heat treatment process for graphene CVD synthesis

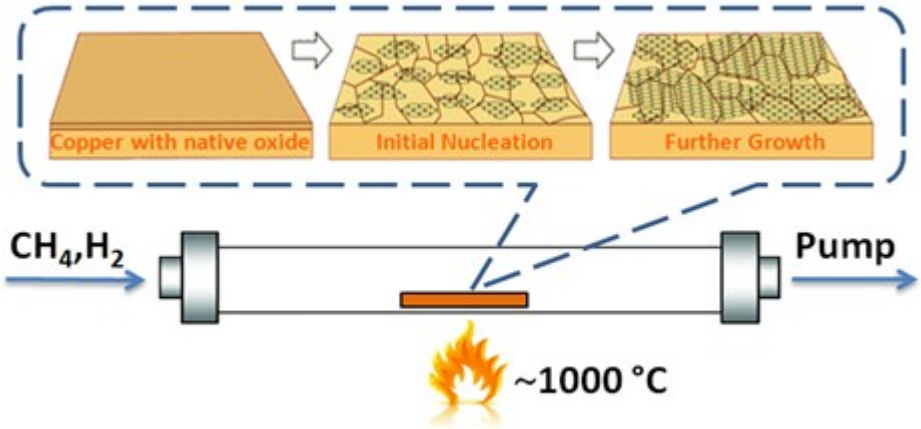

Figure 4-3: Schematic of CVD process for graphene synthesis

(Adapted from [79])

Figure 4-1 and Figure 4-2 illustrate the CVD process. Details of procedures are listed below:

A. Cleaning of copper foil

Copper foil (99.99% purity, 25μm thickness, from Alfa Aesar) is cut into small pieces of desired size (normally 20 mm × 20 mm) with scissors. Cleaning the foil surface is accomplished by sonicating it in acetone, Isopropyl alcohol (IPA) and DI water (each for 10 minutes) and blow to dry in nitrogen gas.

B. Pre-treatment of copper foil

Immerse the foil into acetic acid solution (50%) for twenty minutes to remove the native oxides on copper surface, after which the foil is rinsed with DI water and dried in nitrogen gas.

C. Sample loading

After being flattened between two clean glass slides, the copper foil is placed on a quartz slide and loaded into the middle of the quartz tube. Note: glass slides must not be used as it would be melted in the high temperature environment.

D. Vacuum pumping

Pump the system until ~10^{-2} mBar (1 mBar = 0.75 Torr = 100 Pa) and refill the chamber with H_2 gas to ~100 mBar. Repeat several times to remove oxygen from the system.

E. Annealing

After vacuum pumping, anneal the copper foil at 1000 °C under 80 sccm H_2 gas for 10-60 minutes. This is to remove the remaining native oxides on copper surface and enlarge the copper domains [40].

F. Growth

Introduce the precursor gas (methane) into the system at desired flow rate for a given

period of time (1-30 minutes), after which the heating is turned off. The standard recipe to obtain continuous monolayer graphene is 40 sccm CH_4 with a total pressure of ~ 8 mBar.

G. Cooling

When the temperature of the system falls below 800 °C, open the split furnace to allow faster cooling.

H. Unloading

When the temperature of the chamber falls below 100 °C, the sample is unloaded from the quart tube and stored in a clean sample box.

4.2 The Transfer process

A frame-assisted transfer method is utilized to transfer graphene onto the whole area of the substrate (10 mm * 10 mm SiO_2/Si, quartz and MgO substrates).

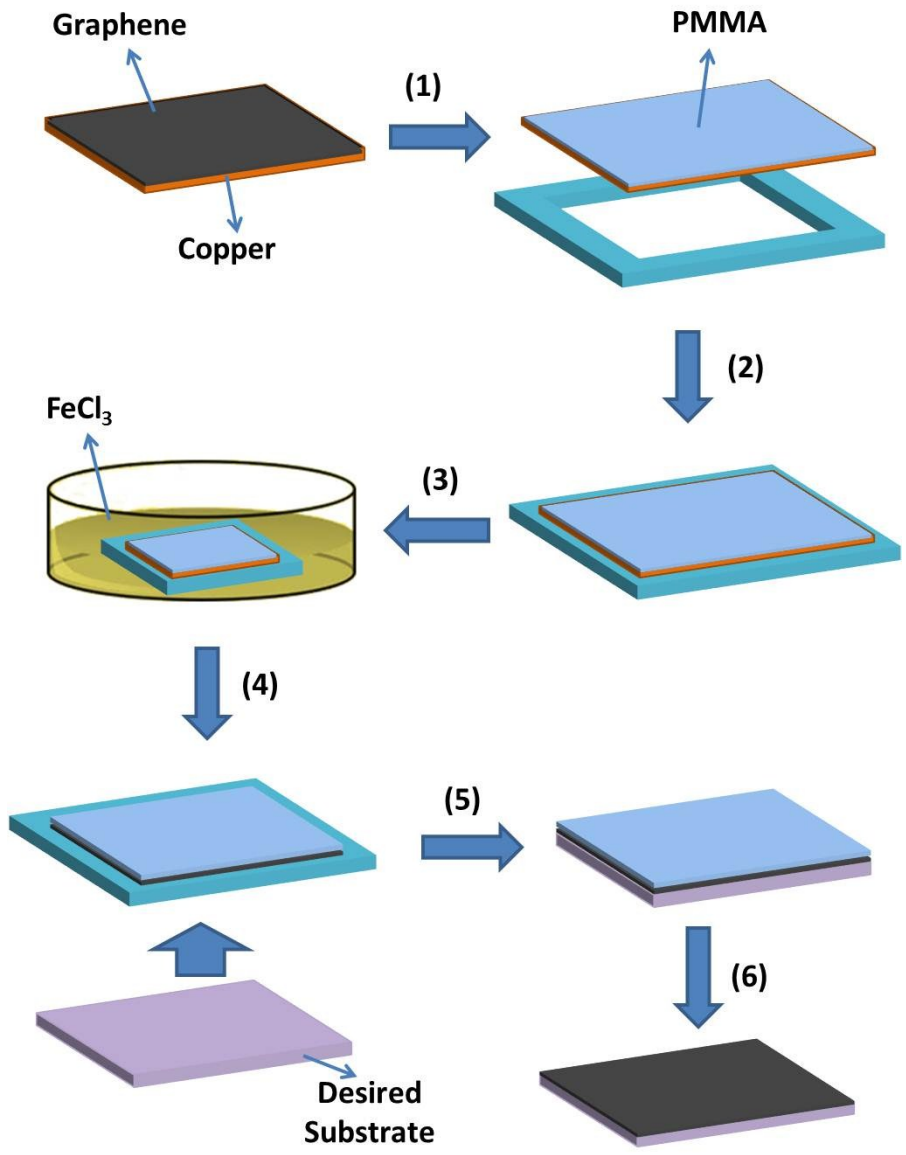

Figure 4-4: Schematic of the frame-assisted transfer process

(1): Spin coat PMMA on graphene/copper. (2): fix PMMA/graphene/copper on plastic frame. (3): Remove copper in $FeCl_3$ etchant solution. (4) Pick up the PMMA/graphene/frame from etchant solution and clean in DI water. (5): Transfer the

PMMA/Graphene film using target substrate from the hole of frame. (6) Remove PMMA support with acetone or annealing.

Figure 4-3 illustrates the frame-assisted transfer process which can cover the whole substrate surface with graphene films with very few wrenches. Details of procedures are listed below:

A. Preparation of copper foil

Flatten the copper foil (with graphene grown on both sides) by pressing it between two clean glass slides. Cut foil into desired size (normally 10 mm * 10 mm) with scissors.

B. Nitric acid treatment

Float the copper foil sample on nitric acid solution (10%) for 2 minute to remove graphene on one side. After etching, float copper foil (with graphene on the top side) on DI water bath for 30minutes to remove the nitric acid residues. Pick up the cleaned foil from the DI water bath and leave to dry.

C. PMMA coating

Place the cleaned copper foil on spin coater and start vacuum pump to fix sample. Use a micropipette to cover the top side of Cu foil (with graphene) with PMMA A6 solution (6% in Anisole, from MicroChem Corp. c). Spin cast with certain recipe of spin speed and period. (Refer to Figure 4-5, typically 3500 rpm for 45s) Leave the sample to dry in air.

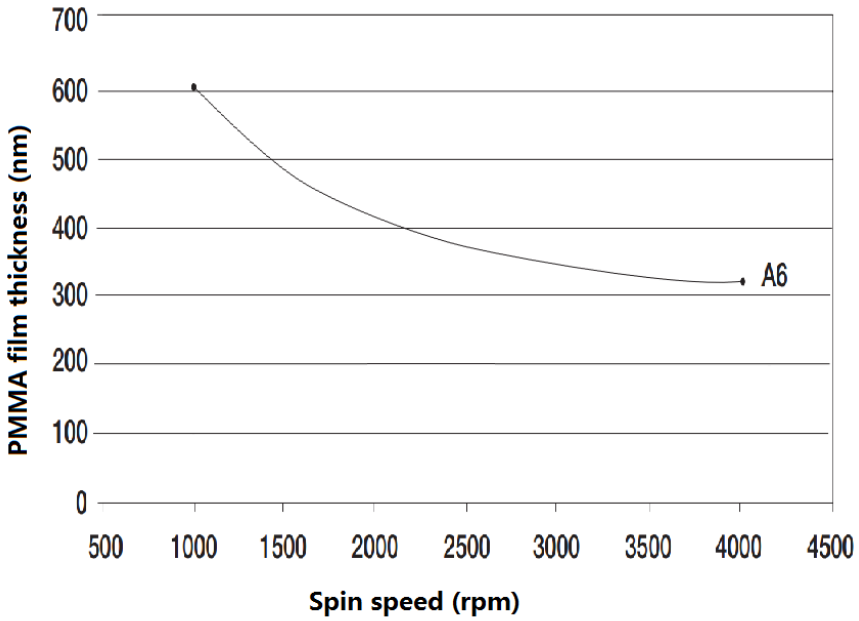

Figure 4-5: The resulted PMMA thicknesses with different spin speeds for 45s.

(Adapted from reference [80])

D. Frame fixing

Place the PMMA/Graphene/Copper onto the plastic frame. Fix the edge with clips.

E. Copper Etching

Prepare etchant bath of $FeCl_3$ (46g/100ml). Immerse the frame into the bath to etch away copper from the bottom side of copper foil (without PMMA protection).

Cover bath with parafilm and leave until copper is completely etched away. (normally 2-5 hours).

F. PMMA/Graphene Cleaning

After all copper are etched away, pick up the frame from the etchant solution. Remove the $FeCl_3$ residues by immersing in DI water bath and HCl bath (10%) several times,

each for 30 minutes. Repeat until the pH value of DI water bath does not change from original.

F. Substrate Cleaning

Sonicate the target substrate in acetone and IPA solution for 10 minutes each.

G. Frame Detachment

Place the PMMA/graphene/Frame onto cleaned substrate and press with clean glass slide. Remove the plastic frame.

H. PMMA removal

(1) Annealing

Place the PMMA/graphene/substrate on a quartz slide in the middle of heating zone of the tube furnace. Anneal the sample in 80 sccm H_2 gas with pressure of ~ 4 mBar.

(2) Acetone treatment

For alternative, acetone solution can be used to remove PMMA from the sample. Dump the PMMA/graphene/substrate into warm acetone bath (45 °C) for 1 hour. Remove and leave to dry.

Some times to get very clean graphene films, annealing and acetone treatment are combined and repeated to minimize the PMMA residues.

4.3 Characterizations

The as synthesized graphene films are characterized by SEM, optical microscope, Raman spectroscopy, and four-probe electrical measurement.

Figure 4-6 shows a typical CVD grown graphene film under SEM. Most of the copper surface (>95%) is covered with monolayer graphene, while some dark area indicates the existence of multi-layer graphene. Due to the differences in thermal expansion between carbon (graphene) and metal (copper in this case), the graphene contracts less than copper while cooling down from the high synthesis temperature (~1000 °C) after growth[81], resulting in the formation of wrinkles which can also be clearly observed in the SEM image.

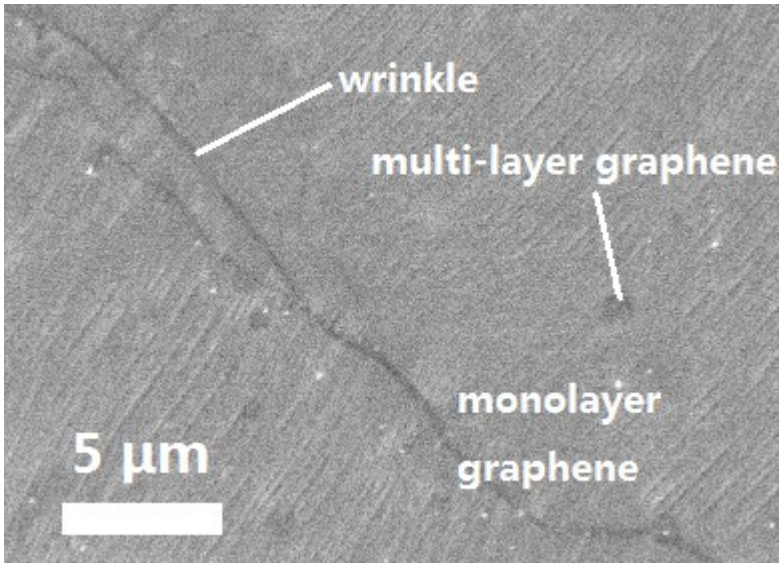

Figure 4-6: A typical SEM image of CVD grown graphene on copper

Figure 4-7 shows a typical CVD grown graphene film transferred onto SiO_2/Si substrate (SiO_2 thickness: 285 nm) under optical microscope. The majority of

monolayer graphene region and small multi-layer graphene regions corresponds to the morphologies observed under SEM (Figure 4-6).

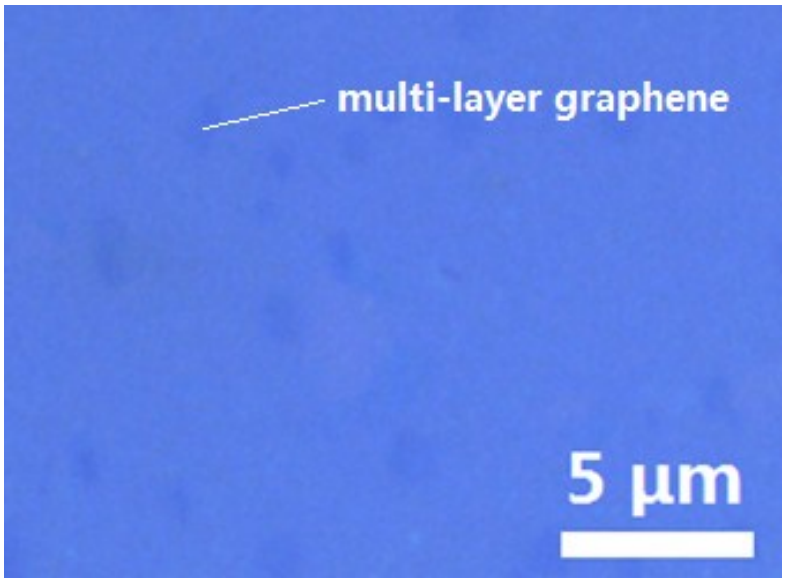

Figure 4-7: A typical optical image of CVD grown graphene transferred onto SiO_2/Si substrate (SiO_2 thickness: 285 nm)

Figure 4-8 shows the optical images of as grown CVD grown graphene and commercial CVD grown graphene (bought from graphene supermarket) transferred onto quartz substrates. As grown graphene has much smaller multi-layer areas compared to large hexagonal multi-layer regions in commercial graphene.

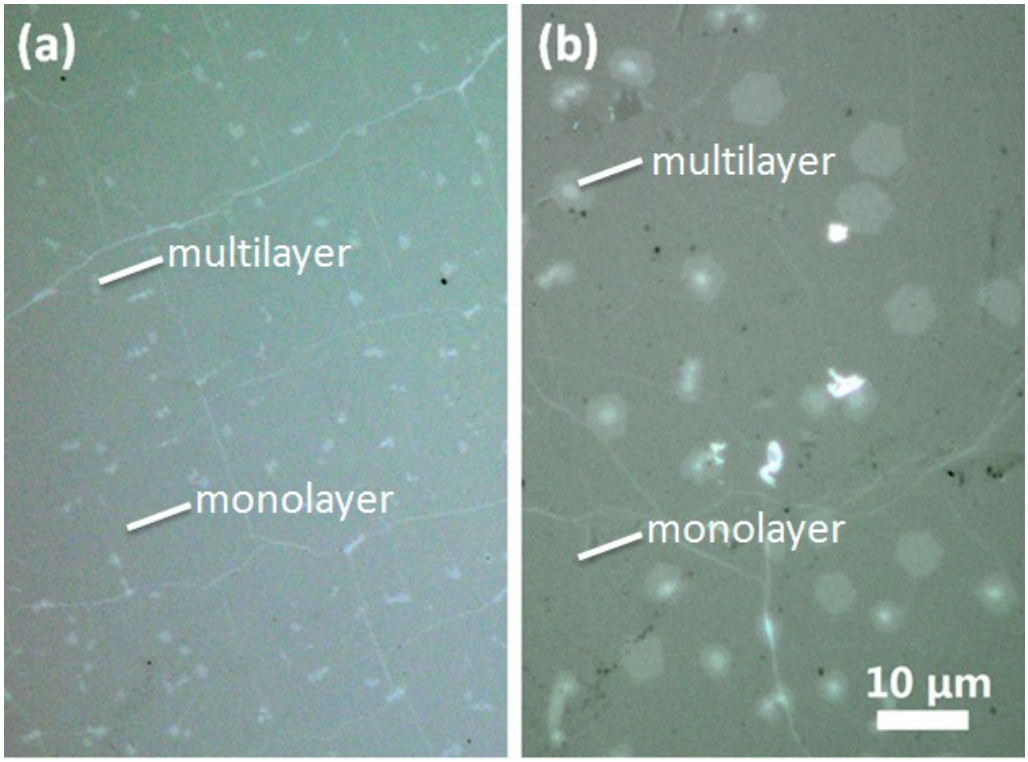

Figure 4-8: Optical images of (a) as grown CVD grown graphene and (b) CVD grown graphene bought from graphene supermarket transferred onto quartz substrates. Scale bar applies to both images.

Figure 4-9 shows a typical optical microscope image of CVD grown graphene transferred onto a quartz substrate. The majority monolayer graphene area and small multi-layer graphene area can be clearly distinguished. Raman spectra (Figure 4-10 and Figure 4-12) further confirm their monolayer / multilayer nature: the weak intensity of the D peak proves the good quality of graphene film; the intensity ratio of G/2D bands as well as the differences in 2D band shapes indicate they are monolayer graphene (Figure 4-10) and multi-layer graphene (Figure 4-12) respectively. The mapping data of G and 2D bands (Figure 4-11) indicate homogenous, high quality monolayer graphene across the mapping area.

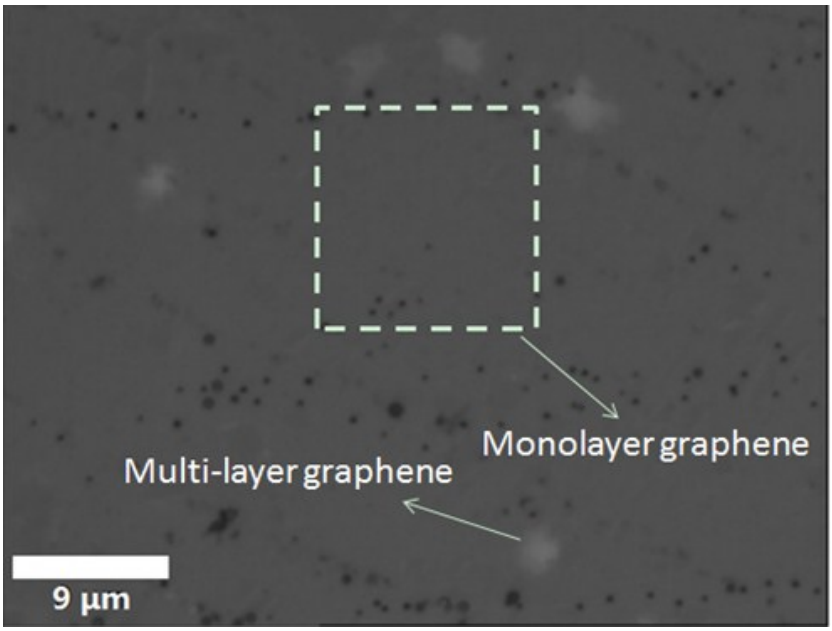

Figure 4-9: Optical image of CVD grown graphene transferred onto a quartz substrate.

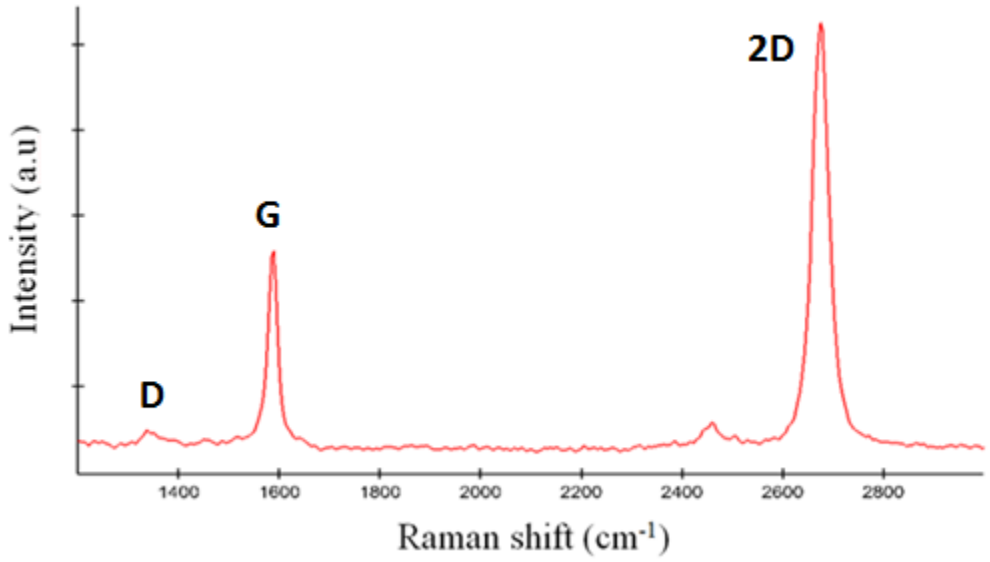

Figure 4-10: Raman spectrum of monolayer graphene region in Figure 4-9.

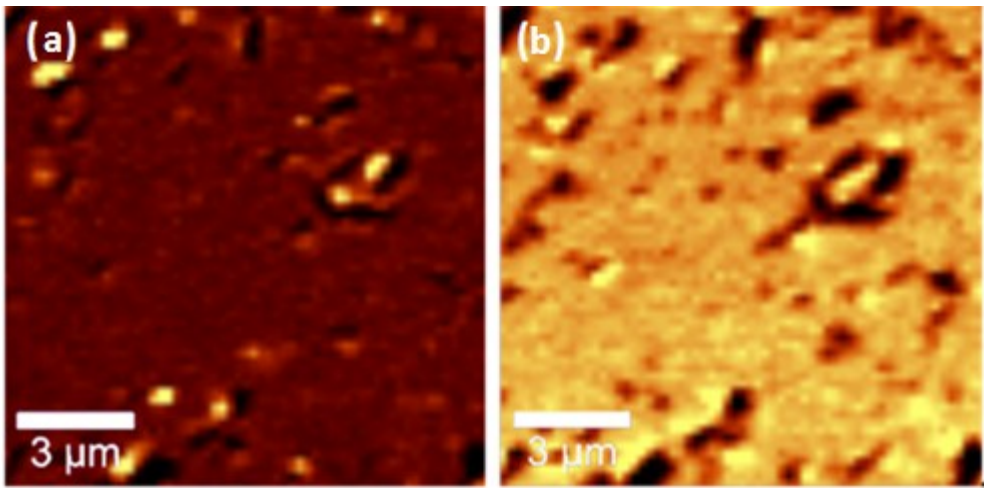

Figure 4-11: Raman mapping of the monolayer graphene region in Figure 4-9.

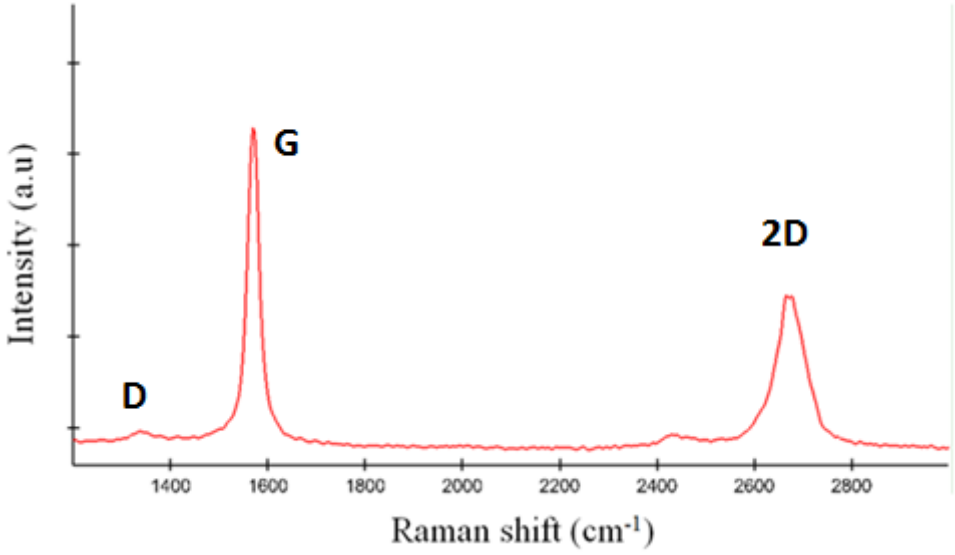

Figure 4-12: Raman spectrum of multilayer graphene region in Figure 4-9.

Four-probe electrical measurements are conducted to measure the sheet resistances of synthesized graphene films transferred onto 10 mm * 10 mm quartz substrates. CVD grown graphene samples (on copper) bought from graphene supermarket are also transferred in the same method onto the same substrate and measured as comparison. It is found that as-grown graphene (840.-1990 Ω/sq) is comparable (slightly more

conductive) than normal commercial graphene (1260-2000 Ω/sq). (See appendix 8.2 for more details.)

It is also notable that even graphene films synthesized under the same conditions vary in their conductivities. On the one hand, better control of the synthesis and transfer processes is needed to improve consistency in graphene properties. On the other hand, a convenient way to examine the conductivity of graphene films in a fast and low-cost way is urgently needed for quality control, which is explored in chapter 5.

4.4 Effects of growth parameters

Different growth conditions are explored by varying a certain parameter and keeping other parameters same as the standard growth condition (session 4.1.2). These parameters are studied and optimized to obtain continuous, high quality monolayer graphene.

4.4.1 Copper pre-treatment

Before the CVD growth, the copper foil is treated with acetic acid solution (50%) for 20 minutes to remove the native oxides on copper surface. This step is very important to reduce the copper oxide particles in the synthesized graphene and to obtain more continuous graphene.

Figure 4-13 shows the graphene/copper surface without acetic acid treatment. Many particles are observed on the surface where graphene film breaks into cracks. These particles hinder the graphene growth to form continuous film and thus should be prevented. Figure 4-14 shows the EDX analysis of these particles. The existence of oxygen indicates these particles are copper oxides.

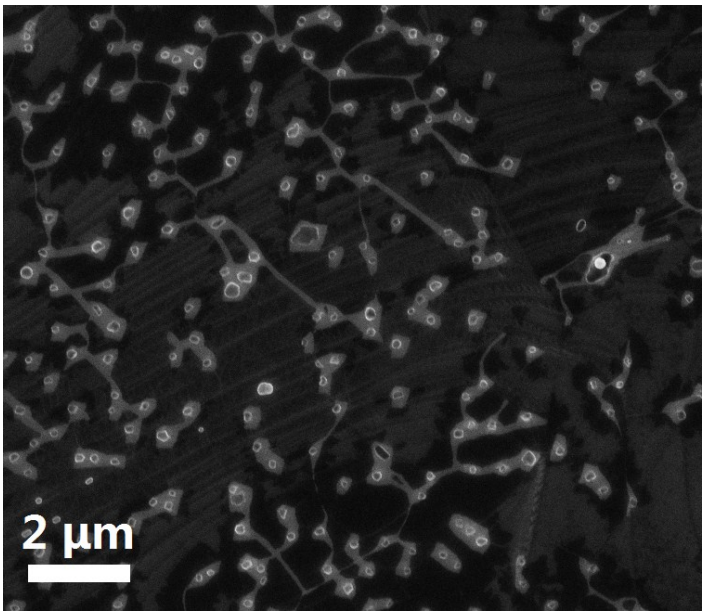

Figure 4-13: SEM image of the CVD grown graphene on copper foil without acetic acid treatment. Impurity particles can be clearly observed near the edges of graphene.

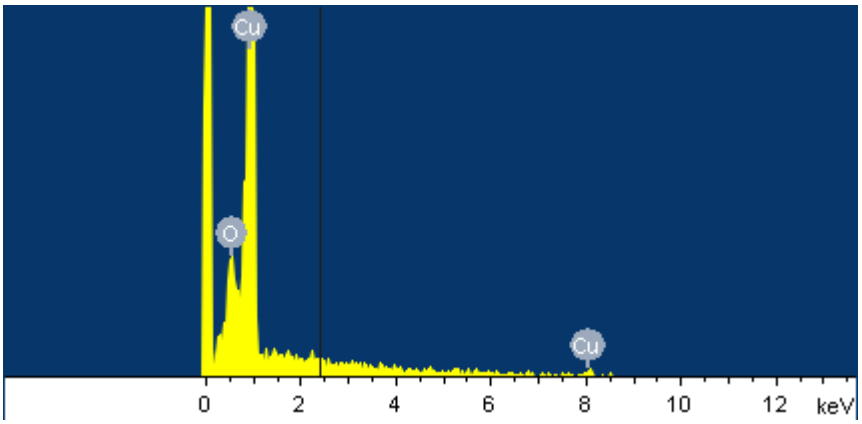

Figure 4-14: EDX analysis of the particles on graphene/copper surface.

Figure 4-15 shows the graphene/copper surface with 20 minutes' acetic acid treatment. Compared with Figure 4-14, the size and number of particles are significantly reduced and the graphene film is continuous. It is thus recommended that

15-30 minutes' minutes' acetic acid treatment of the copper foil to remove most of the native copper oxide immediate before every graphene growth.

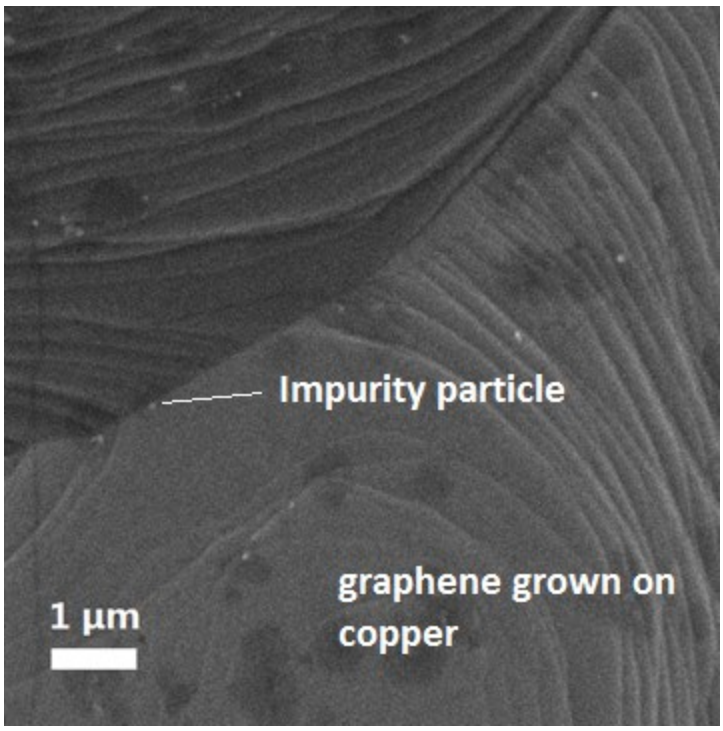

Figure 4-15: SEM image of the CVD grown graphene on copper foil with 20 minutes' acetic acid treatment. Much less and smaller impurity particles are observed.

4.4.2 Annealing

The copper substrate is normally annealed in hydrogen gas to remove the remaining native oxides on the surface. It is found in this study that annealing can also reduce the coverage of multi-layer graphene. Figure 4-16 shows the differences of synthesized graphene on copper without and with annealing for 1 hour at 1000 °C.

The graphene grown without annealing step has multiple multi-layer areas, covering ~51% of the whole surface, while the graphene grown with annealing step has only few small multi-layer areas, covering only <2%. It is probably because annealing can increase the size of copper domains and reduce copper defects [40]where the nucleation of multi-layer graphene would happen.

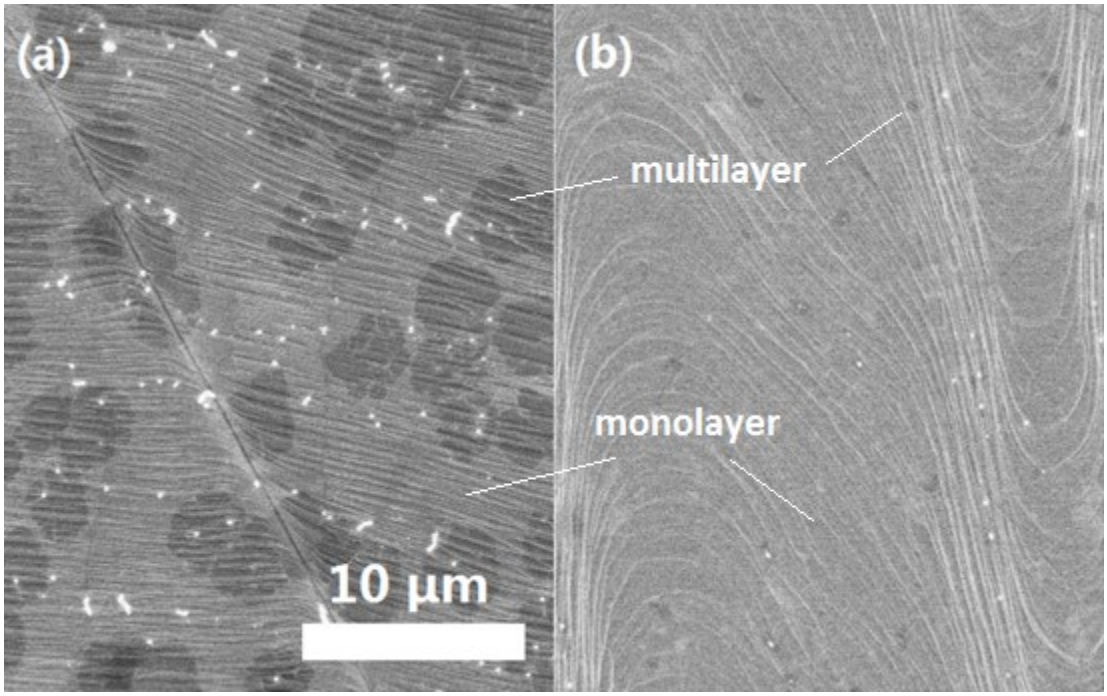

Figure 4-16: SEM images of graphene grown on copper foil (a) without annealing; (b) with annealing for 1 hour at 1000 °C before growth. Scale bar applies to both images.

4.4.3 Growth temperature

Graphene films are grown at a set of temperatures (700 °C, 800 °C, 900 °C, and 1000 °C) while other parameters remain the same as the standard condition (session 4.1.2). According to the SEM images (Figure 4-17), there is hardly any graphene

formed at 700 °C; some small graphene flakes begin to form at 800 °C, and further enlarge when the temperature rises to 900 °C; continuous graphene begin to form at 1000 °C.

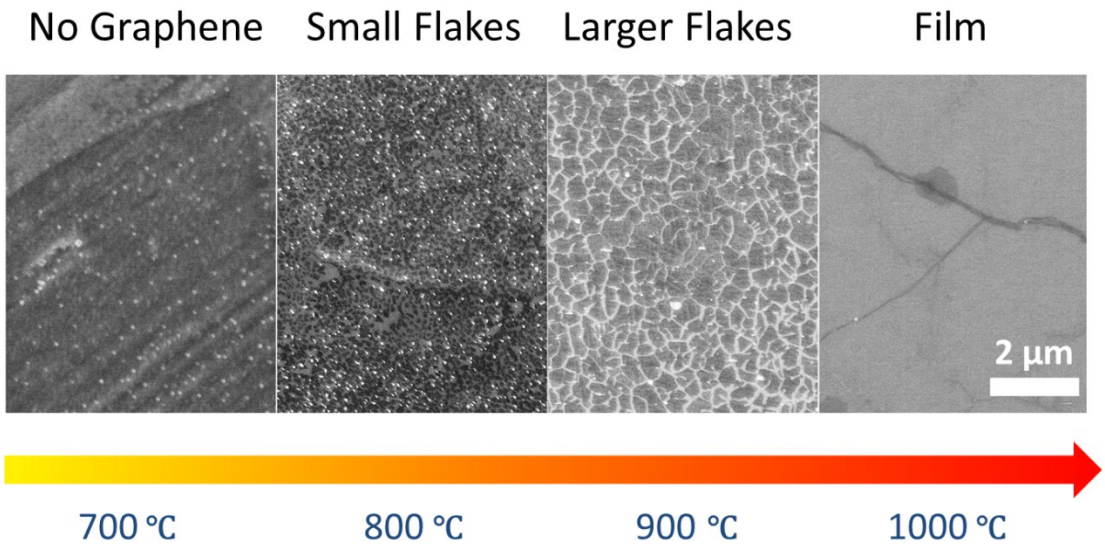

Figure 4-17: SEM images of graphene grown at different temperatures: 700 °C (a), 800 °C (b), 900 °C (c), and 1000 °C (d). Scale bar applies to all images.

4.4.4 Growth time

Graphene growths were conducted in the standard condition (session 4.1.2) for different periods of time (1-30 minutes), which are represented in Figure 4-18. Small graphene flakes (~ 1 µm in size) began to emerge at 1 minute and further grew into larger flakes (~ 10 µm in size). After 10 minutes, those flakes have almost merged into continuous films. The change of graphene coverage over time is shown in Figure 4-19.

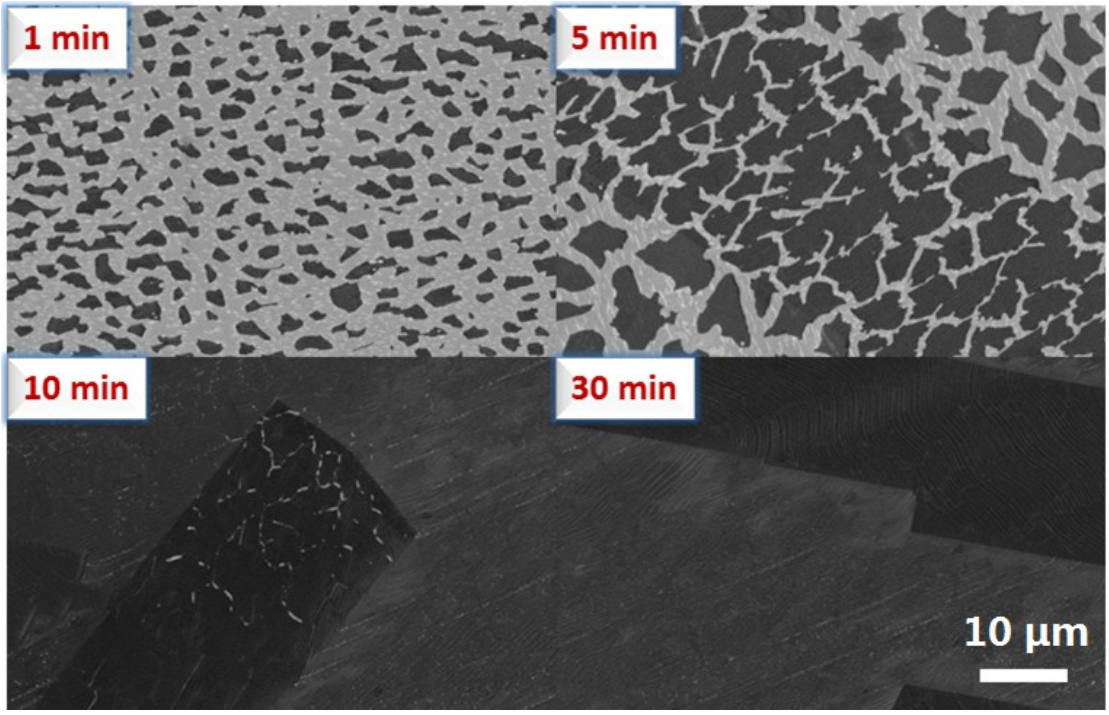

Figure 4-18: CVD graphene grown at different periods of time: 1, 5, 10, 30 minutes. White area: copper surface. Black area: copper with graphene grown on surface.

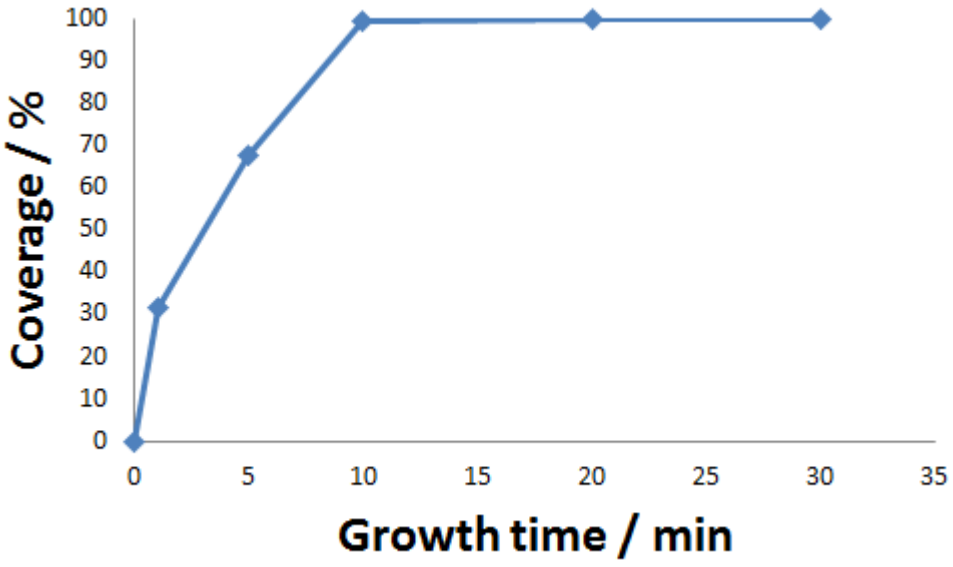

Figure 4-19: Changes of graphene coverage over growth time

4.4.5 Methane / hydrogen ratio

The possible reaction processes during the CVD growth are:

$$CH_4 \rightleftharpoons CH_3 + H$$

$$CH_3 \rightleftharpoons CH_2 + H$$

$$CH_2 \rightleftharpoons CH + H$$

$$CH \rightleftharpoons C + H$$

$$nC \rightleftharpoons \text{Graphene } (C_n)$$

It can be inferred that when the CH_4/H_2 is large, the reactions moves towards the formation of graphene / multi-layer graphene; while on the contrary, graphene formation would be hindered (etched).

Graphene growths are conducted in different CH_4/H_2 flow rate ratios while other parameters remain the same as the standard condition (session 4.1.2), which are represented in Figure 4-20. When CH_4/H_2 ratio is very small (1:8), the synthesized graphene flakes are in small and regular hexagonal shapes due to the significant etching effect of hydrogen. When the CH_4/H_2 ratio is higher (1:4), the graphene flakes become larger and stay in less regular shapes. When the CH_4/H_2 ratio reaches 1:2, continuous graphene films begin to form (mostly monolayer). When the CH_4/H_2 ratio continues to increase, multilayer graphene area becomes larger and covers a significant percentage of the whole surface. The change of graphene coverage over CH_4/H_2 ratio is shown in Figure 4-21.

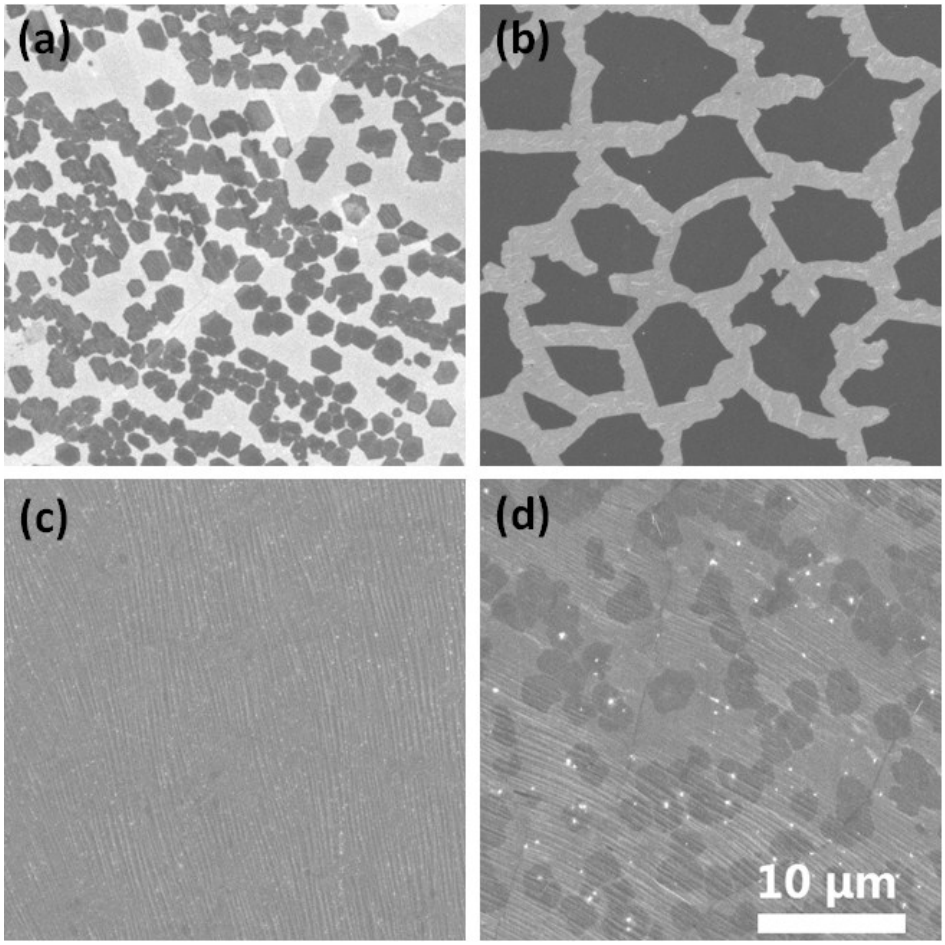

Figure 4-20: CVD graphene grown at different methane / hydrogen ratios: 1:8, 1:4, 1:2, and 2:1. (a): small graphene flakes; (b): larger graphene flakes; (c): continuous monolayer graphene; (d)monolayer graphene with multilayer regions (dark area)

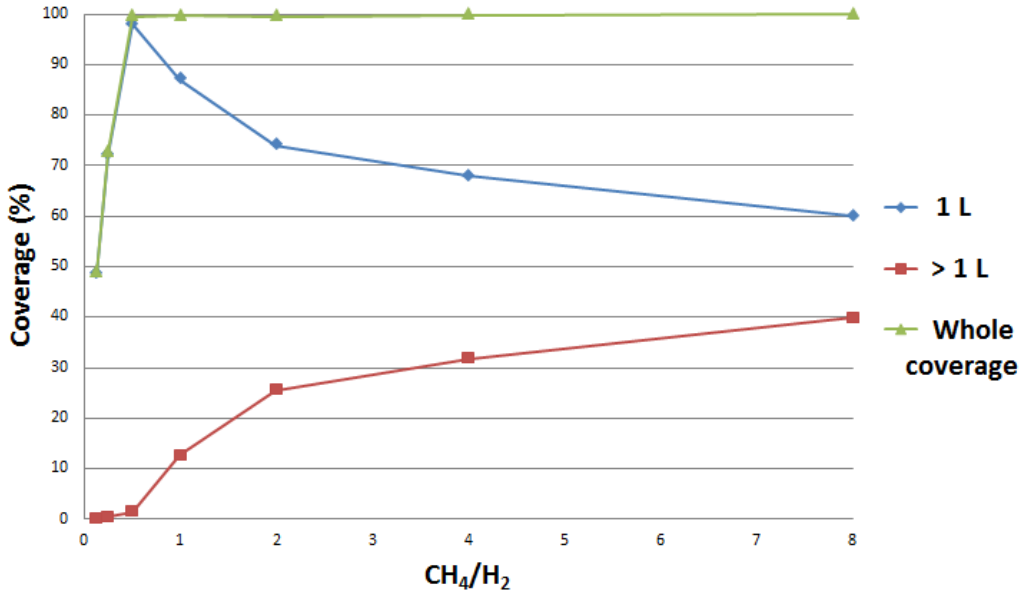

Figure 4-21: Changes of graphene coverage over methane / hydrogen ratio

4.4.6 Total pressure

Graphene growths are conducted at different total pressures while other parameters remain the same as the standard condition (session 4.1.2). According to Figure 4-22, at low pressures (~ 0.8 mBar), graphene tends to grow into large discontinuous flakes while at higher pressures (~ 8 mBar) it ends to form continuous films. At even higher pressures, significant multilayer graphene forms.

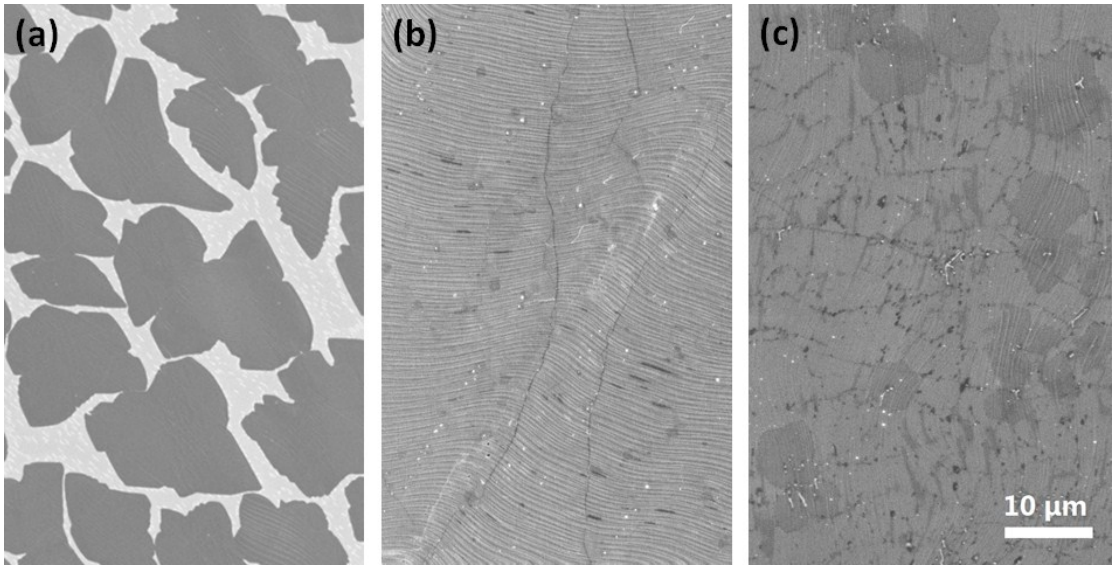

Figure 4-22: CVD graphene grown at different pressures: (a) ~0.8 mBar, discontinuous graphene flakes; (b) ~8 mBar, continuous monolayer graphene (c) ~80 mBar, monolayer graphene with multilayer regions (dark area)

4.5 Optimization of the transfer process

To obtain continuous and clean graphene films over the whole substrate for microwave measurement and other applications, the conventional transfer process is adapted into a frame-assisted transfer process.

4.5.1 The frame-assisted transfer

The conventional fishing method is widely utilized as an effective way for transfer of small-area graphene film (smaller than the substrate). However, when attempting to cover the whole substrate surface with a large graphene sheet, this method always result in holes and ripples due to folding and slipping. (Figure 4-23)

The frame-assisted transfer method (session 4.2) was developed to solve this problem by using a plastic frame to fix the graphene and transfer the flat PMMA/graphene directly to the target substrate without folding (Figure 4-24). Figure 4-25 shows complete graphene substrates transferred using this novel method.

The frame-assisted transfer method also avoids damaging problems during cleaning. In conventional transfer method, the PMMA/graphene film is cleaned in DI water baths several times to remove etchant residues, resulting in damages when the film detaches from the glass slides to new DI water bath. In the new frame-assisted transfer method, the film will not touch any solid surface before transferring onto the target substrate.

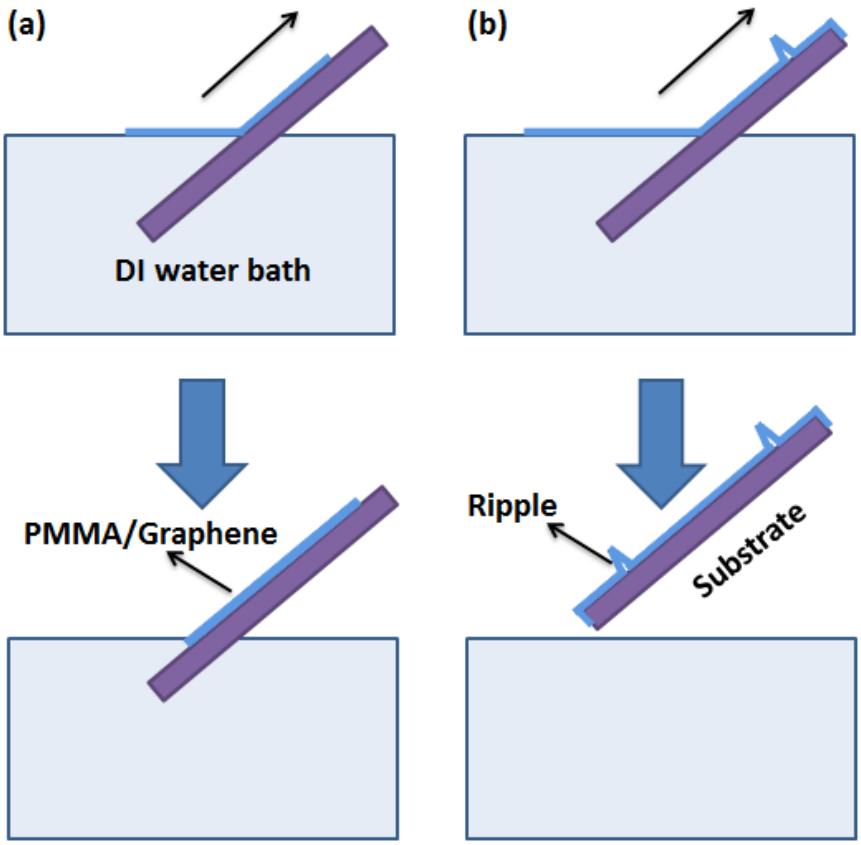

Figure 4-23: Schematic of the conventional fishing transfer process

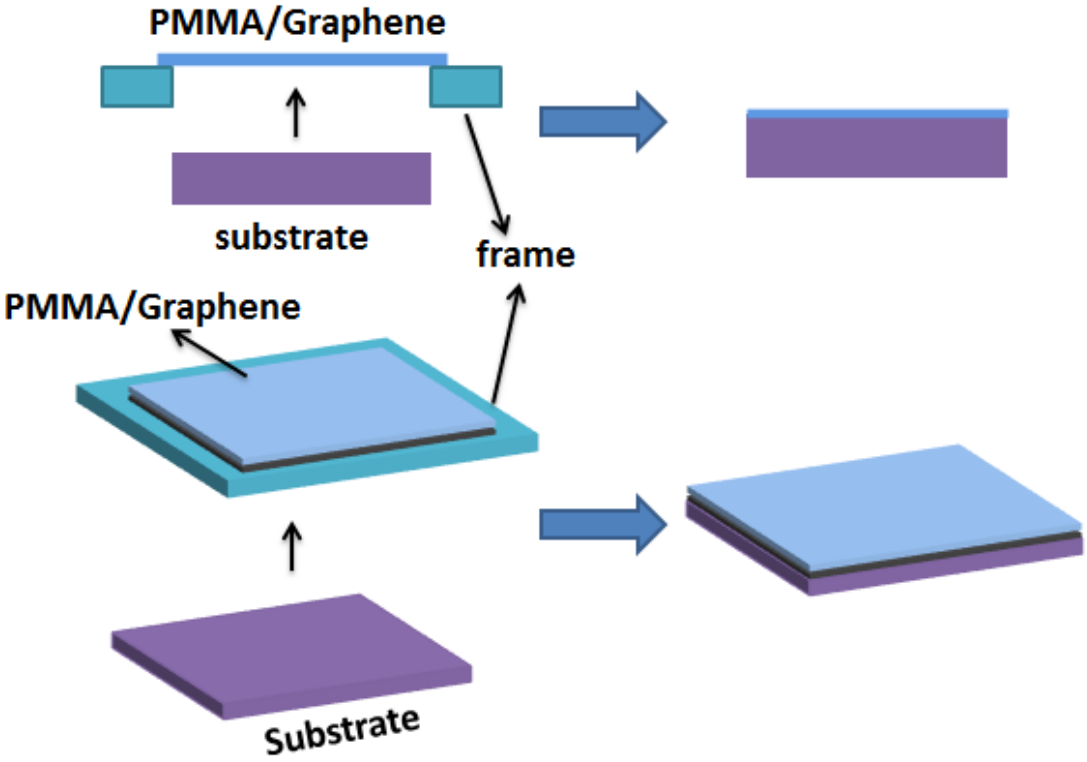

Figure 4-24: Schematic of the adapted frame-assisted transfer method.

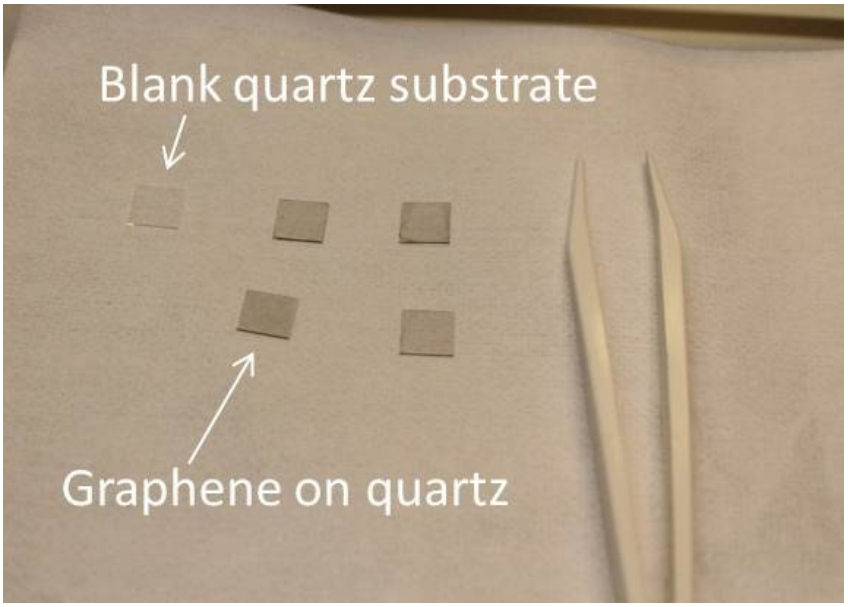

Figure 4-25: A typical photo of complete CVD grown graphene films transferred onto quartz substrates. (substrate size: 10 mm * 10 mm)

4.5.2 Removal of PMMA

Defects and impurities of the transferred graphene film mainly come from three sources: (1) cracking and folding of graphene film during transfer; (2) contaminations from substrate or the etchant solution; and (3) the PMMA residues. Cracking and folding can be minimized through the novel frame-assisted transfer method, and the contaminations can be minimized through repeating cleaning of the substrate and PMMA/graphene films. The PMMA residues remain a big problem to be solved.

Figure 4-26 shows transferred graphene films with different PMMA removal methods utilized. The acetone treatment can dissolve most of PMMA residues; however the broken holes and undissolved PMMA residues still appears on the graphene surface (Figure 4-26 a). The heat annealing brings less damage to the graphene films, but some PMMA residuals are still able to survive the thermal decomposition and evaporation process (Figure 4-26 b). By combining the two methods together, the annealing-acetone method can lead to clean and complete graphene films with few residues and broken holes (Figure 4-26 c).

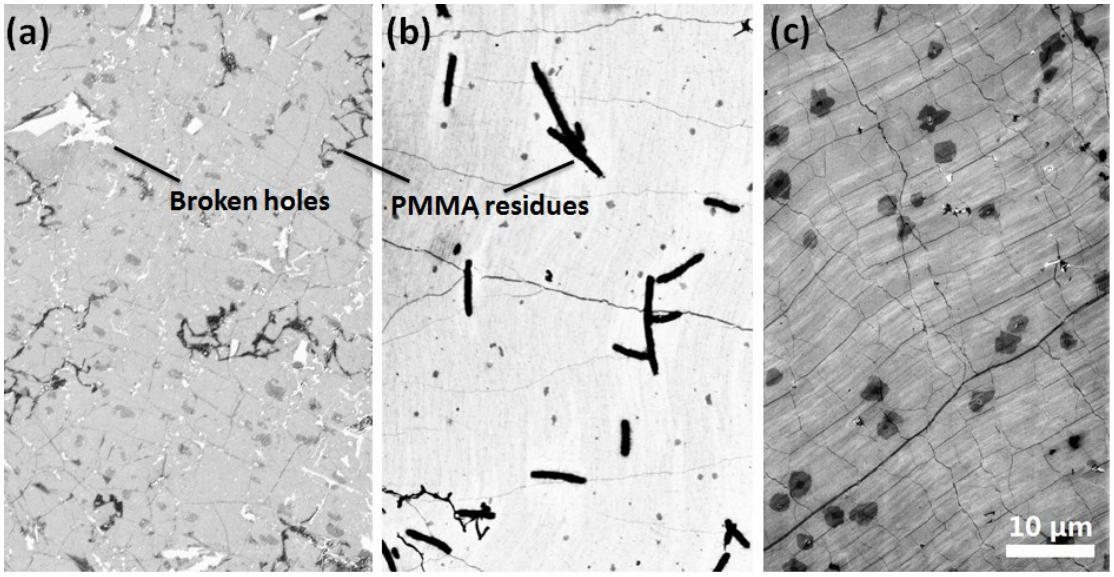

Figure 4-26: SEM images of CVD grown graphene transferred with different methods to remove PMMA: (a) acetone treatment; (b) thermal annealing; (c)

thermal annealing + acetone treatment. The scale bar applies to all 3 images.

4.6 Fabrication of graphene free-standing structures

It is well known that graphene' properties are affected by the underlying substrates due to scattering from charged impurities [82; 83], substrate stabilized ripples [84; 85], and contaminations on substrates. In order to improve the performance of graphene devices, free-standing structures are needed to eliminate effects from supporting substrates.

Although free-standing structures have been fabricated by directly transferring graphene film onto holes [5; 86] and trenches [87; 88], and by etching away the underneath substrate [115], it is still challenging to customize the device structure. Here we proposed a novel fabrication method involving photolithography and copper under-etching to obtain graphene freestanding structures (Figure 4-27).

(1): growth/transfer of graphene;

(2): spin photoresist;

(3): expose and develop;

(4): removal of unmasked graphene by oxygen plasma;

(5): chemical etching of copper;

(6): strip photoresist.

The whole process is compatible with standard semiconductor processing techniques

and the structure can be easily customized to different needs by changing the mask design.

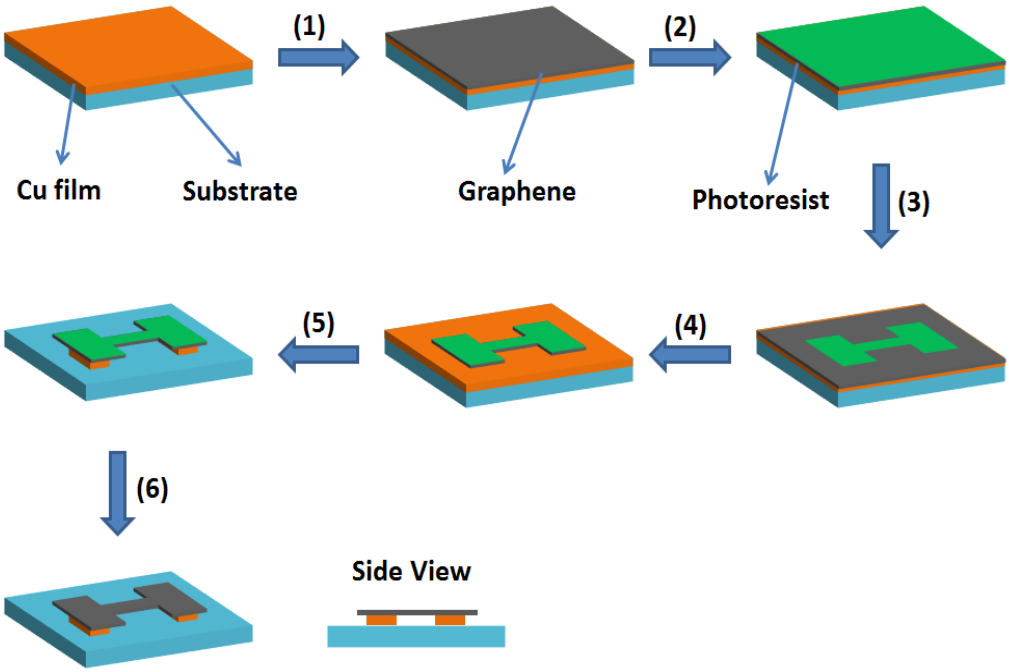

Figure 4-27: Schematic of the proposed transfer-free process involving lithography.

4.6.1 Transfer of graphene onto copper film

As the graphene growth technique on copper thin film has not been fully established in our group, CVD graphene grown from copper foil was transferred onto an 800 nm-thick copper film on a SiO_2/Si substrate with conventional fishing transfer technique. The homogeneous graphene sheet can be clearly observed in SEM images (Figure 4-28 and Figure 4-29).

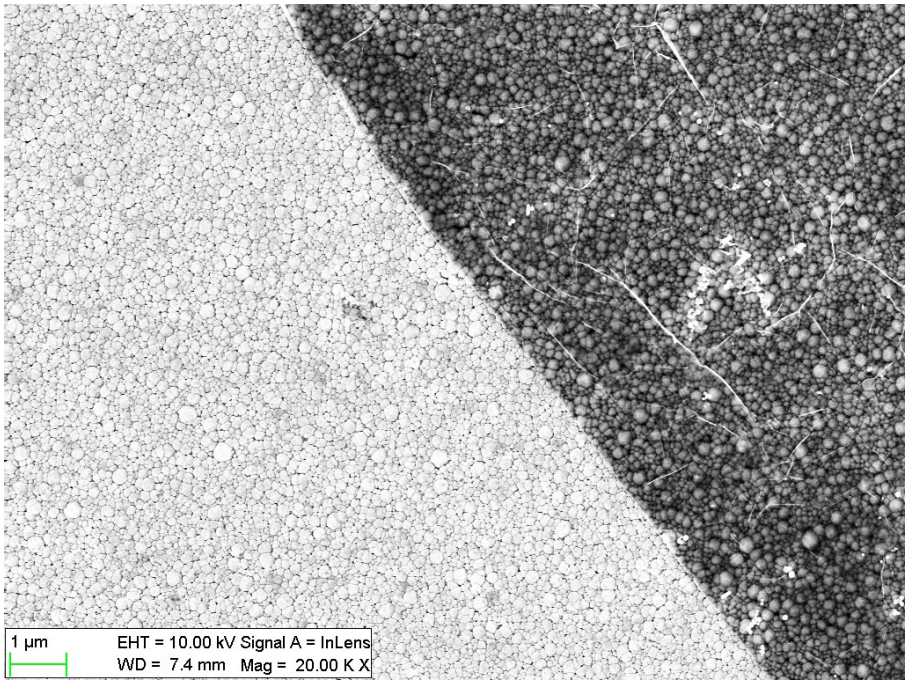

Figure 4-28: SEM image of the graphene sheet transferred onto copper thin film. Left: the copper thin film. Right: graphene sheet on the copper thin film. White lines: wrinkles of the graphene sheet.

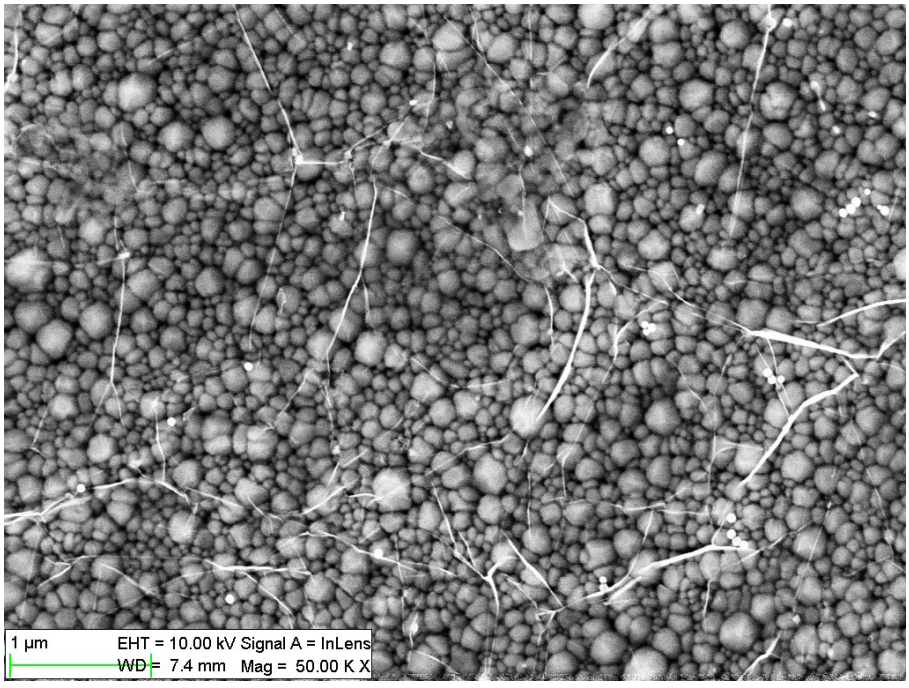

Figure 4-29: High-resolution SEM image of graphene sheet on copper thin film. Graphene wrinkles (white lines) can be clearly observed.

4.6.2 Patterning of bridge structure

A positive photoresist (AZ 5214E, thickness = ~1.4 μm) is then spin coated onto the graphene/copper structure and patterned into bridge structures by the standard photolithography techniques (Figure 4-30). The uncovered graphene is then removed by oxygen plasma.

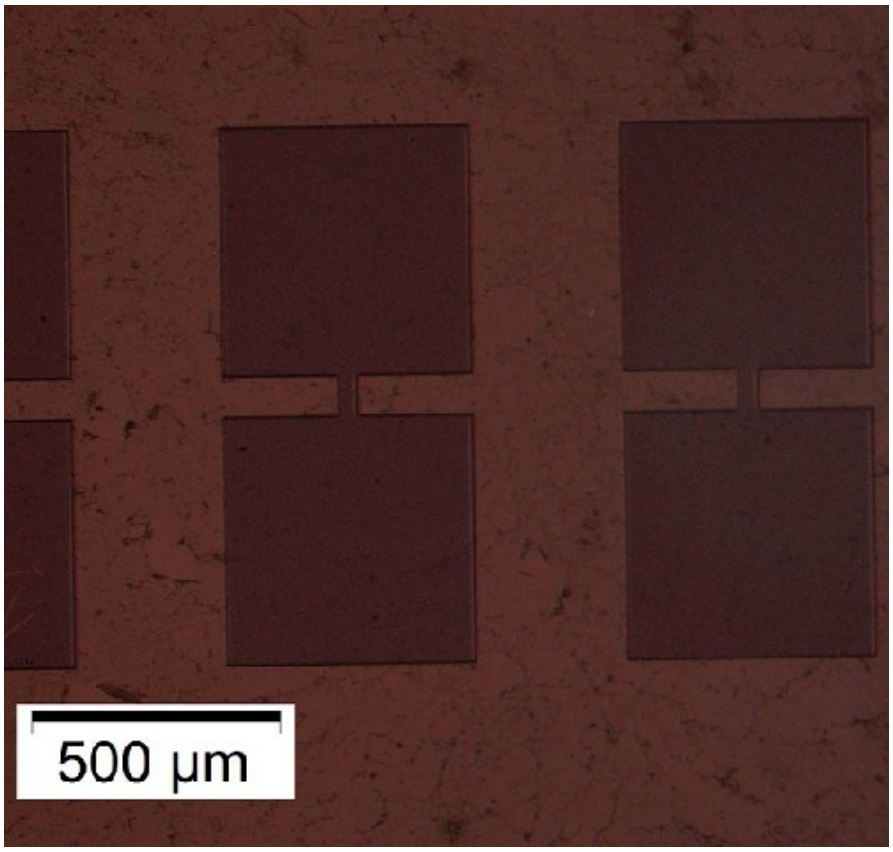

Figure 4-30: Optical image of the patterned photoresist bridge structures on graphene/copper film.

4.6.3 Under-etching of copper

After the uncovered copper is etched away by ammonium persulfate solution ($(NH_4)_2S_2O_8$, 0.1 mol/L), the under-etching begins from the edges of photo-resist-covered copper structures. Figure 4-31 and Figure 4-32 and shows the optical images of the same structure after copper etching for different period of times. The etching rate for under-etching is estimated to be 500 nm/minute. These preliminary results suggest that the under-etching method is effective in removing the underlying copper. However, the length of the bridge structure is still too large to make it completely free-standing from the substrate.

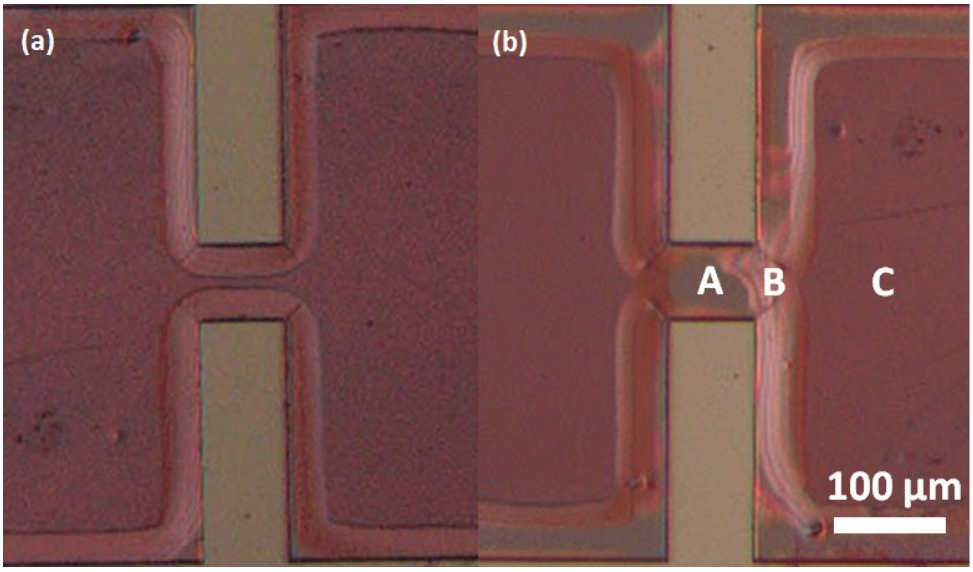

Figure 4-31: Optical images of the same structure after copper etching for 1 hour (a) and 2 hours (b). The scale bar applies to both images.

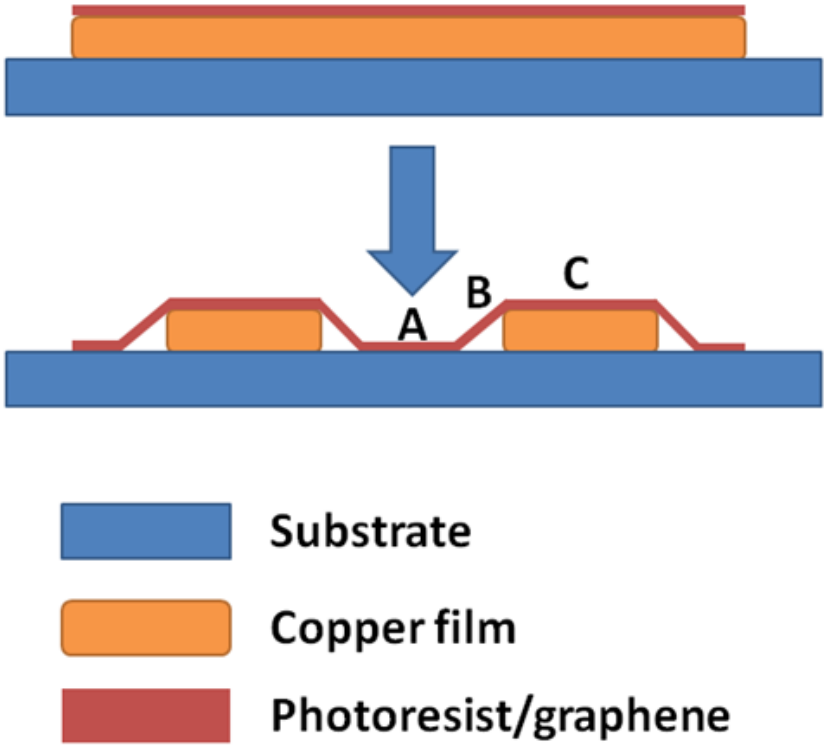

Figure 4-32: Schematic of the under-etching process (side view). Region A, region B and region C correspond to region A, region B and region C in Figure 4-31.

4.6.4 Summary and Future work

The proposed under-etching method is a novel way to obtain graphene free-standing structure lifted up from the substrate. Preliminary results suggest that the under-etching method is effective in removing the underlying copper. Further explorations are still needed:

As the length of the bridge structure is still too large to make it completely free-standing from the substrate, masks with shorter structures are needed.

After the copper under-etching, the graphene free-standing structure could be achieved by removing remaining photoresist. A critical point drying technique can be utilized to remove photoresist without damaging the graphene [17; 89]. This step will be carried out after relevant facilities become available.

This process can also be further explored and optimized by growing graphene directly on copper thin films.

4.7 Conclusions

In summary, the parameters of CVD growth of graphene and transfer processes are carefully explored and optimized. Large-area, continuous and high quality monolayer graphene is obtained: The size of synthesized graphene reaches 20 mm * 20 mm, and can be further extended by upgrading a large reaction chamber; the monolayer coverage rate and conductivity is better than normal commercial graphene products on the market. A novel frame-assisted method is developed to transfer graphene without introducing many defects and impurities. A novel annealing-acetone combined method can remove PMMA residues more effectively and unharmfully. A new under-etching route to fabricate a graphene free-standing structure is proposed and explored.

The conductivity of synthesized graphene is still lower than mechanical exfoliated graphene sheets and need to be further improved. Possible ways include: utilising atomic- smooth single crystal copper as growing substrate, and plasma-enhanced CVD facilities to reduce the growth temperature.

5. Convenient Microwave Examination of Large-area Graphene[3]

5.1 Aim and Purpose

On the one hand, most of the large area transparent electrode applications require a low sheet resistance (<500 Ω/sq) (Figure 5-1).[91] On the other hand, the electrical properties of graphene may be inhomogeneous over a large area in industrial synthesis. It is important to develop convenient, accurate and low-cost methods to examine the conductivity / sheet resistance of graphene for industrial applications.

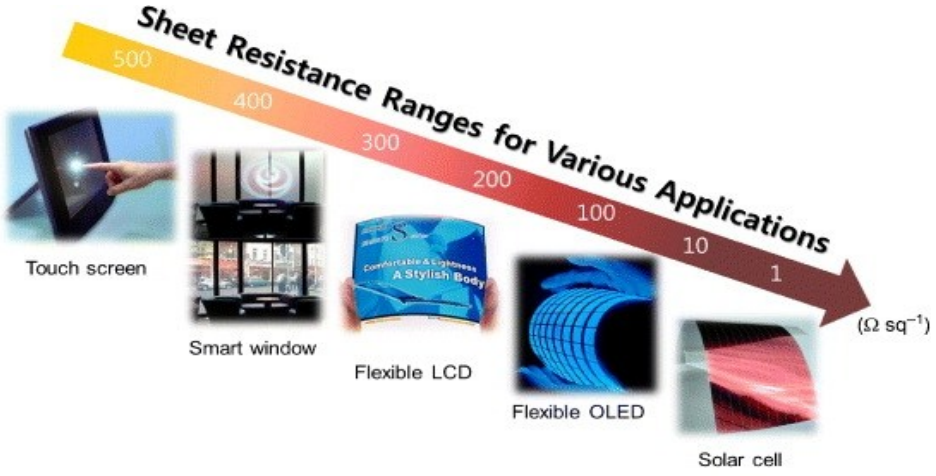

Figure 5-1: Various graphene applications as a transparent electrode and the corresponding sheet resistance requirement for each application. (From Reference [91])

[3] Parts of this chapter has been published or in submission preparation:
Shaforost, O.; Wang, K., et al, "Microwave characterization of large area graphene using a TE01δ dielectric resonator." Physics and Engineering of Microwaves, Millimeter and Submillimeter Waves (MSMW), 2013 International Kharkov Symposium on , pp.427,429, 23-28 June 2013
Shaforost, O.; Wang, K., et al, "Contact-free sheet resistance determination of large- area graphene layers by an open dielectric loaded microwave cavity.". In preparation.

Although direct-contact electrical measurements, such as 4 probes measurements, are the common and established method to measure the sheet resistance of thin film materials including graphene, it involves complex and time consuming steps like lithography to make metallic contacts. What's more, the fabrication processes can also bring contact resistance which alters graphene's intrinsic properties.

As described in previous chapters, Raman spectroscopy is an established non-contact method to examine the quality of graphene products. However, it is not suitable to examine graphene's conductivity: the sheet resistance cannot be inferred from the spectra and the laser beam may bring damage to the graphene. What's more, the limitations on the mapping area and speed make it different to get overall information from a large area sample.

A novel non-contact microwave measurement method has been developed to simplify the processes and to avoid the effects of metallic contacts.[92; 93]

5.2 The Microwave Measurement of Graphene's sheet resistance

5.2.1 The microwave resonator

A microwave resonator was fabricated and utilized together with a Vector Network Analyzer (VNA) to achieve the non-contact measurement of graphene's sheet resistance.

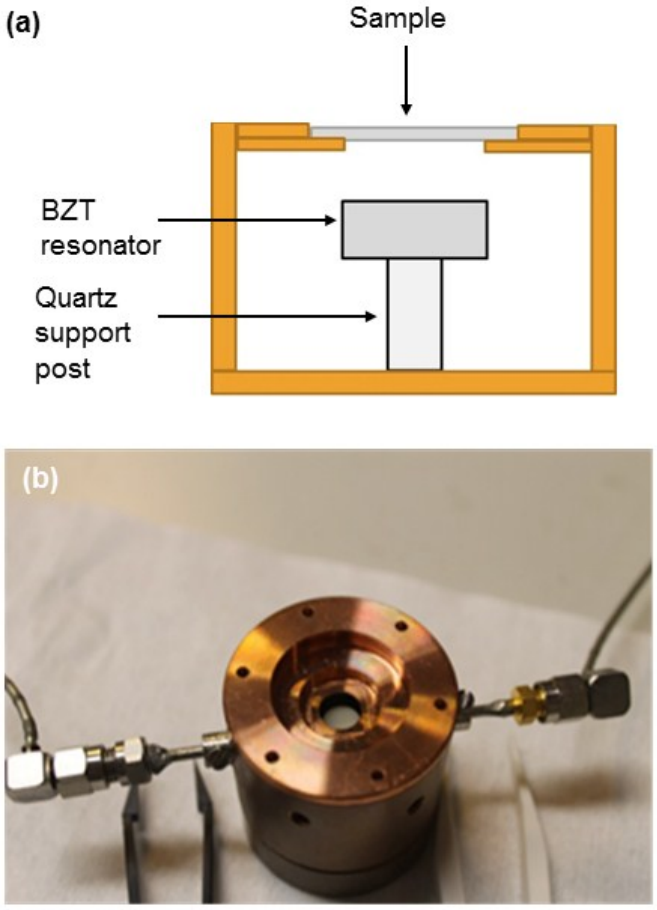

Figure 5-2: Illustration (a) and photo (b) of the microwave resonator.

As shown in Figure 5-2, a BZT (Barium Zirconium Titanate) dielectric disk, whose resonant frequency is around 10 GHz, is excited in the $TE_{01\delta}$- mode. The disk is arranged in a copper cavity with an aperture where the test sample is supported. The electrical field leaks out from the dielectric resonator through the aperture to the test sample (as shown in Figure 5-3).

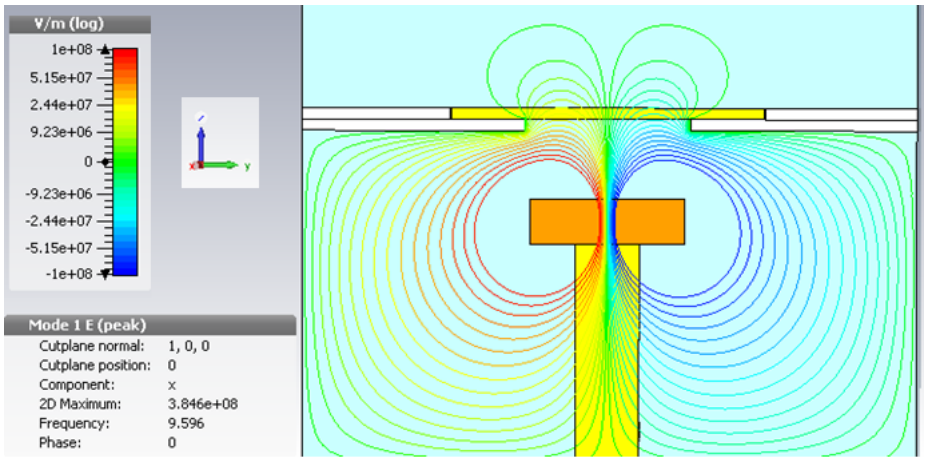

Figure 5-3: CST Microwave Studio simulation of the electric field distribution in the resonator

5.2.2 The measurement procedures

1. The synthesized graphene film is transferred onto target substrates (typically 10 x 10mm^2) using optimized processes described in chapter 4.

2. Blank substrates (as the control group) and the prepared samples are loaded on the resonator (as shown in Figure 5-2).

3. The corresponding curves (as shown in Figure 5-4) are stored and analysed to calculate the sheet resistance of graphene.

4. Every sample is measured several times to minimize random errors.

5. Four-probe measurements are conducted after the microwave measurements as comparisons.

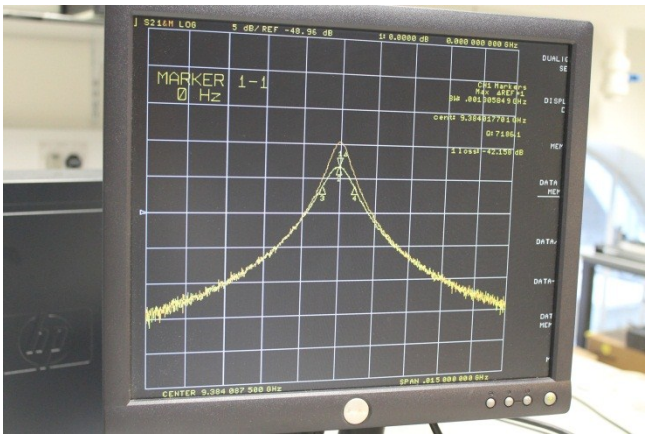

Figure 5-4: Resonance curves displayed on the VNA screen corresponding to a blank quartz substrate (the upper curve) and the quartz substrate covered with a homogeneous graphene monolayer (the lower curve).

5.2.3 Calculation of the sheet resistance based on microwave data

The conducting graphene sheet, whose thickness is only 0.34 nm, can be regarded as a lossy thin film transparent to electric field in microwave frequencies.

Measured inversed change of the Q factor ΔQ_{gr}^{-1} is proportional to power dissipation in graphene P_{gr} per cycle.

$$\Delta Q_{gr}^{-1} = \frac{P_{gr}}{\omega W} \quad \text{(Equation 5-1)}$$

Where W is the total energy stored by the resonator, ω is the cyclic frequency corresponding to the resonant frequency.

The power dissipation P_{gr} can be expressed as the integration of energy conservation over the resonator volume V:

$$P_{gr} = \int_V \frac{\partial W(t)}{\partial t} = \frac{1}{2}\int_V \omega\varepsilon'' \cdot \varepsilon_0 |\boldsymbol{E}^2| dV \quad \text{(Equation 5-2)}$$

where $\boldsymbol{E}$ is the strength of electric field, ε'' is the imaginary part of the relative dielectric permittivity of the lossy dielectric (graphene), and ε_0 is the vacuum permittivity.

ε'' can be expressed as:

$$\varepsilon'' = \frac{\sigma}{\varepsilon_0 \omega} \quad \text{(Equation 5-3)}$$

where conductivity σ can be expressed with sheet resistance R_s and thickness t:

$$\sigma = \frac{1}{R_s \cdot t} \quad \text{(Equation 5-4)}$$

Finally

$$R_s = \frac{1}{\Delta Q_{gr}^{-1}} \cdot \frac{\int_A \boldsymbol{E}^2 dA}{2\omega W} = \frac{\boldsymbol{Z_c}}{\Delta Q_{gr}^{-1}} \quad \text{(Equation 5-5)}$$

Several graphene/quartz samples (CVD grown graphene films transferred onto 10×10×0.05 mm^3 quartz substrate) are measured to determine the characteristic impedance of the cavity $\boldsymbol{Z_c}$. The Q values are obtained through the non-contact measurements; while the sheet resistances R_s are determined through four-probe

measurements (see appendix 8.3 for more details). The regression result is shown in Figure 5-5:

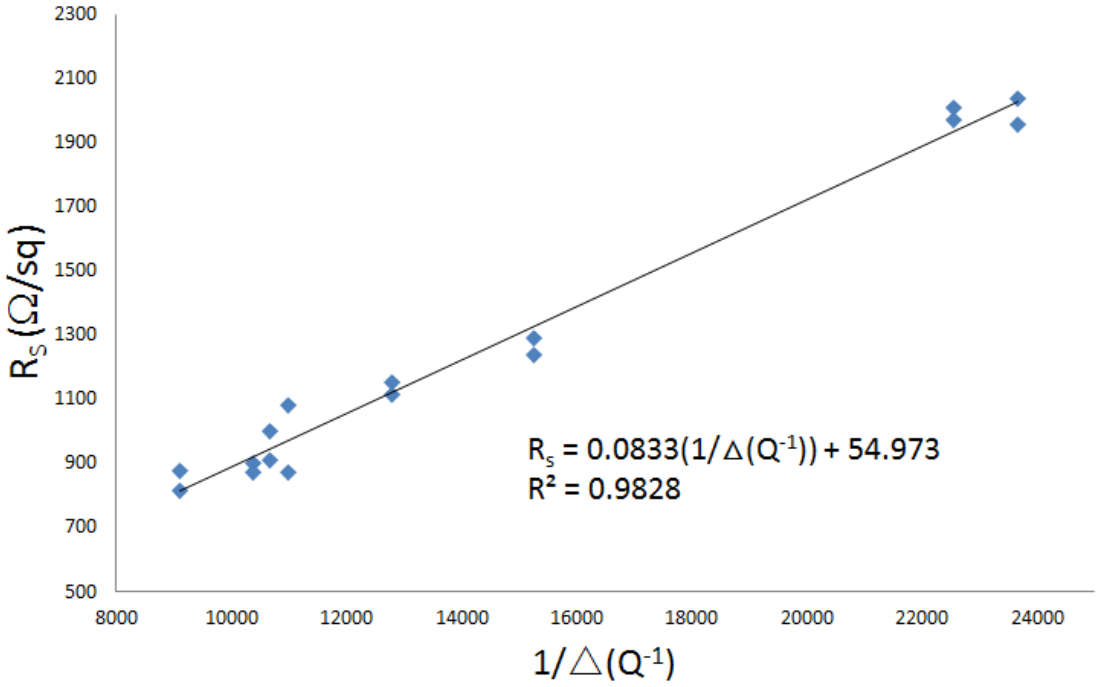

Figure 5-5: The regression of sheet resistances on inversed change of Q-factor. (see appendix 8.3 for more details)

The value of the characteristic impedance was determined by the slope of the trend line:

$$Z_c = 0.0833\ \Omega/\text{sq}$$

The coefficient of determination (R^2) is very close to 1, indicating this method is a reliable way for sheet resistance measurement.

5.2.4 Source of error

① As the graphene test samples are not completely homogeneous over the whole area, four-probe measurements are conducted in different area of the sample to obtain its average sheet resistance. Also, percolation effects[94; 95] may cause some re-distribution effects of currents in case of the dc experiments

② The aperture, where the test sample is supported, is not in ideal symmetry and the graphene samples under test are not completely homogeneous. Several tests are made to obtain the average Q value.

③ The water vapour can also cause significant microwave losses. The microwave measurements need to be conducted in a dry environment.

5.3 Observations of Microwave Field Effect

Since the discovery of graphene in 2004, the field effect of graphene has been a research focus of many scientists [2; 96; 97; 98; 99]. In a typical graphene field-effect transistor (FET), the electronic properties of graphene can be modulated by adjusting the externally applied gate voltage (as shown in Figure 5-6).

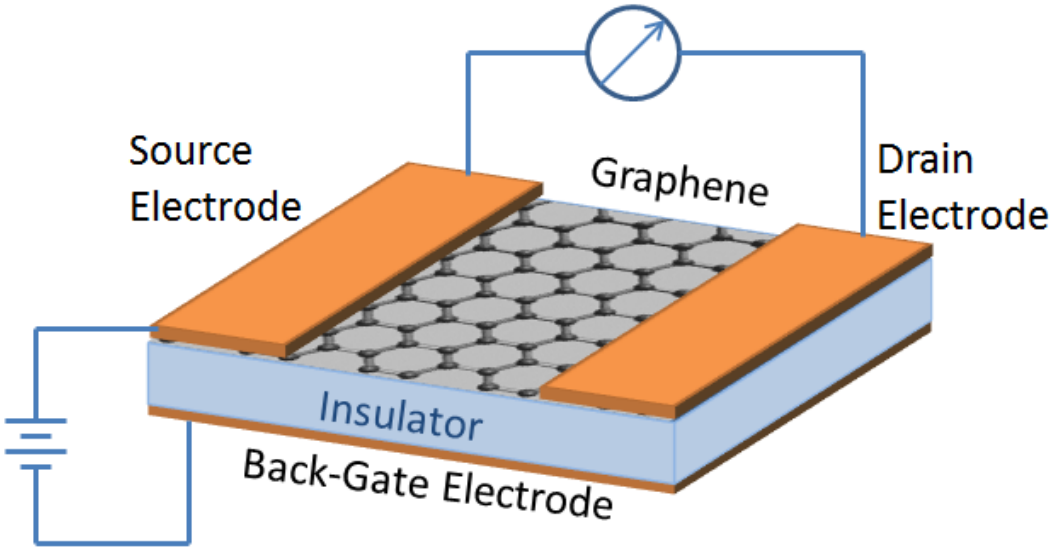

Figure 5-6: Schematic of a typical graphene field-effect transistor.

As is known from the last chapter that the microwave behaviour of graphene is strongly connected to its electrical conductivity, it is fascinating to explore whether the modulation of the graphene's electrical conductivity by the external electric field would eventually lead to corresponding variations in microwave signals. However, there are two main obstacles in current graphene FET devices:

① The current graphene FET devices are too small for microwave examinations. The sizes of the graphene sheets tested are normally in micrometres range while the microwave resonator requires an effective examination area of at least 50 square millimetres.

② The gate electrode, either doped silicon or metals, will introduce significant microwave loss, which makes the observations of the field effect in graphene extremely difficult.

To solve the first problem, large-area CVD grown graphene sheets are chosen instead of mechanically exfoliated ones. To solve the second problem, a new double-layer device was designed and utilized to observe the microwave field effect in graphene. The details will be described in the next sections of this chapter.

5.3.1 Device Design and Fabrication

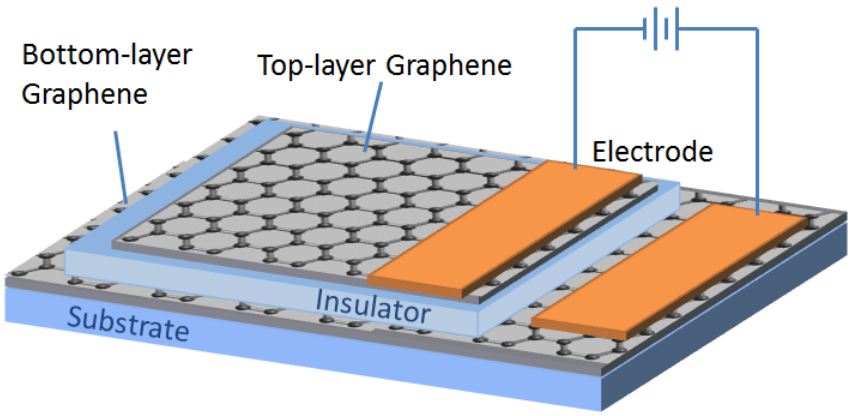

Figure 5-7: Schematic of double-layer graphene microwave field-effect device.

In this PhD project a novel double-layer graphene microwave field-effect device (as shown in Figure 5-7) has been designed and fabricated to overcome the two obstacles: large-area CVD graphene sheets (~10*10 mm^2) are utilized to offer a sufficiently large examination area for the microwave resonator; low lossy substrates like quartz and high resistance silicon are chosen instead of lossy silicon substrates; graphene film replaces Si as the gate electrode for the other graphene layer and the metallic contacts are located on the edge to minimize other conductors' effects on microwave response of the cavity: a thick metal gate would short-circuit the electric field and the losses by the graphene layer would become negligible. The detailed fabrication procedures are listed below (Figure 5-8):

① Transfer of CVD graphene sheet onto the quartz substrate.

② Deposit gold electrodes on the edge of graphene sheet.

③ Spin coat dielectric layer (PMMA ～400 nm) to cover graphene sheet.

④ Deposit gold electrodes on the edge of the quartz substrate.

⑤ Transfer of the second CVD graphene sheet on the dielectric layer.

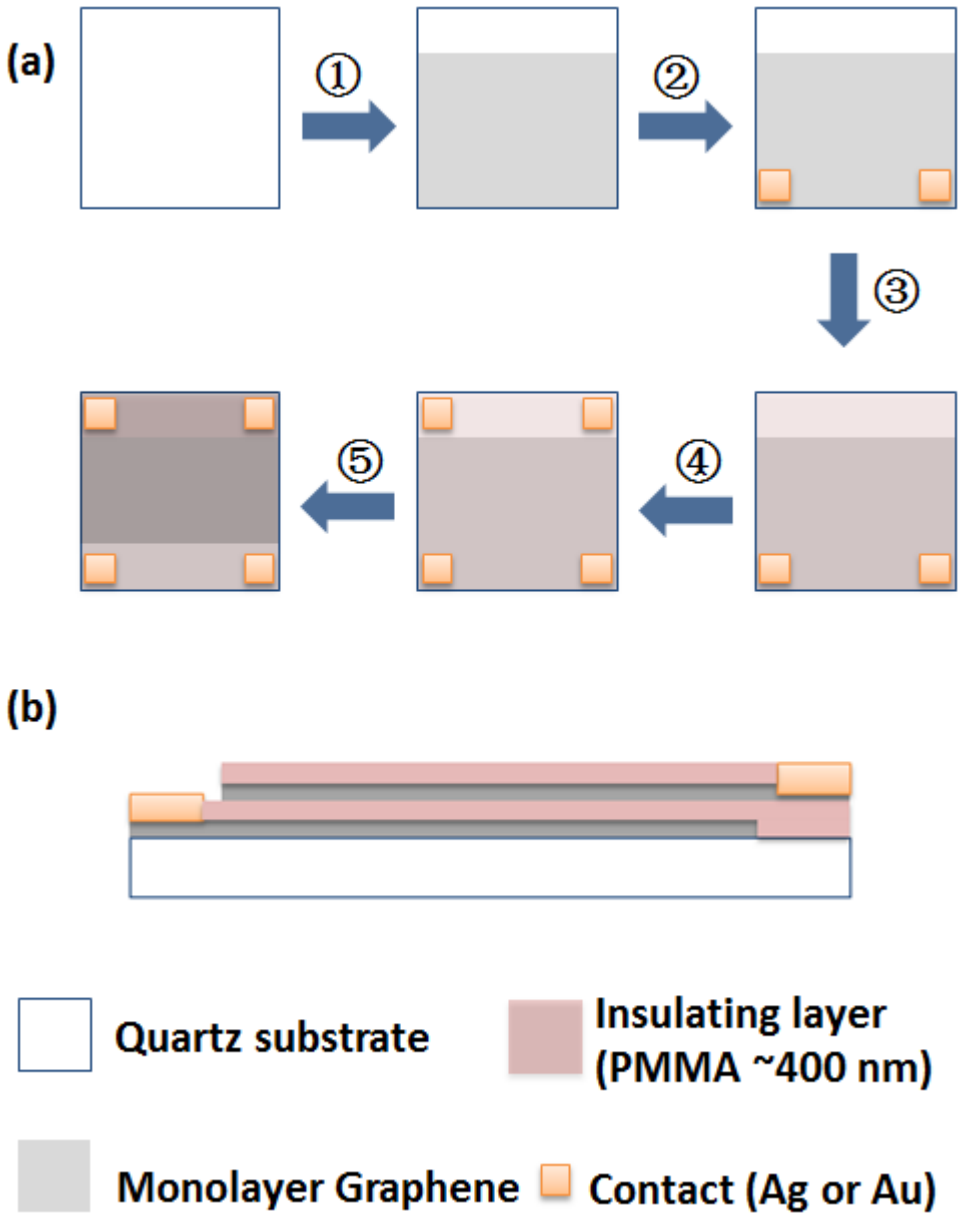

Figure 5-8: (a) Schematic of microwave field-effect device fabrication processes. (b) Side-view of fabricated double-layer graphene microwave field-effect device.

Finally, we get the double-layer structures, which are tested in the microwave resonator (Figure 5-2).

5.3.2 Measurement

The fabricated double-layer device is placed on the microwave resonator and a voltage is applied between two graphene layers through probes (Figure 5-9). The microwave transmission curves under different voltages are stored and analysed.

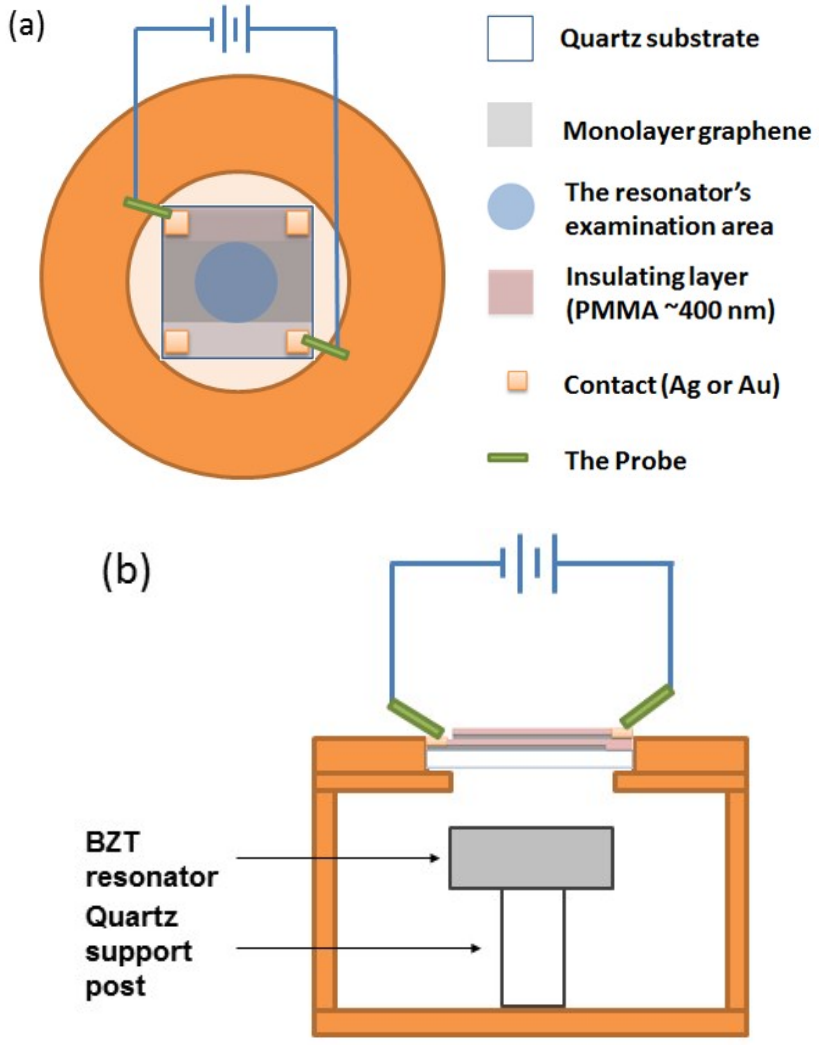

Figure 5-9: Schematic of the microwave field effect test. (a): top-view; (b): side-view.

5.3.3 Results

According to Equation 5-5, the sheet resistance of graphene is inversely proportional to the inversed change of Q-factor ΔQ_{gr}^{-1}. The Q-factor of the resonator with a graphene sample in place can then be described as:

$$Q_{gr} = \left(\frac{Z_c}{R_s} + \frac{1}{Q_0}\right)^{-1} \quad \text{(Equation 5-6)}$$

with Q_0 being the Q factor of the cavity without graphene. Therefore, a decrease in graphene's sheet resistance would lead to a reduction in Q_{gr}. It is predicted that the field effect can improve graphene's conductivity, and thus decrease the measured Q value.

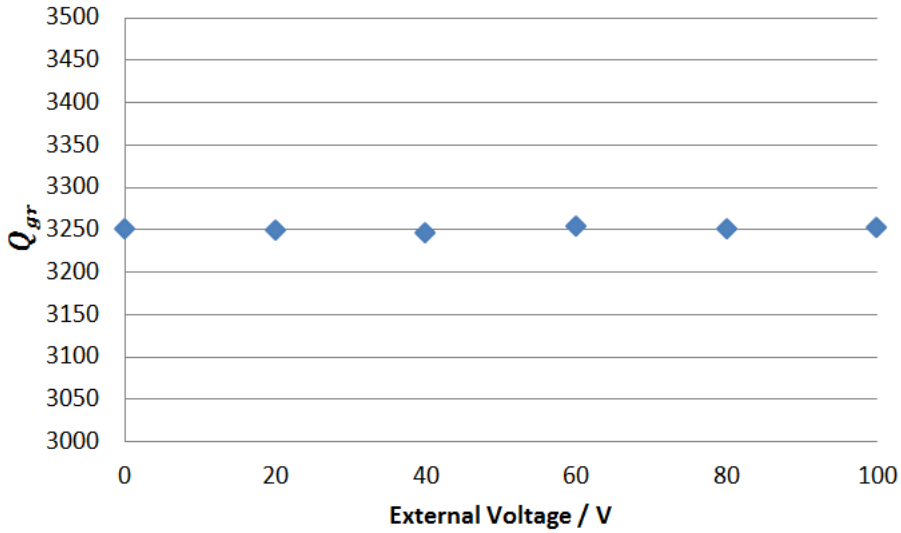

Figure 5-10: The measured Q values of the double-layer device for different voltages applied.

Figure 5-10 shows the measured Q values of the double-layer device for different voltages applied. Changes in Q values are quite small (within the experimental error) and no significant trend is observed.

As a more sensitive method to determine small changes in sheet resistance, the magnitude of power transmission at resonance was recorded as a function of gate voltage.

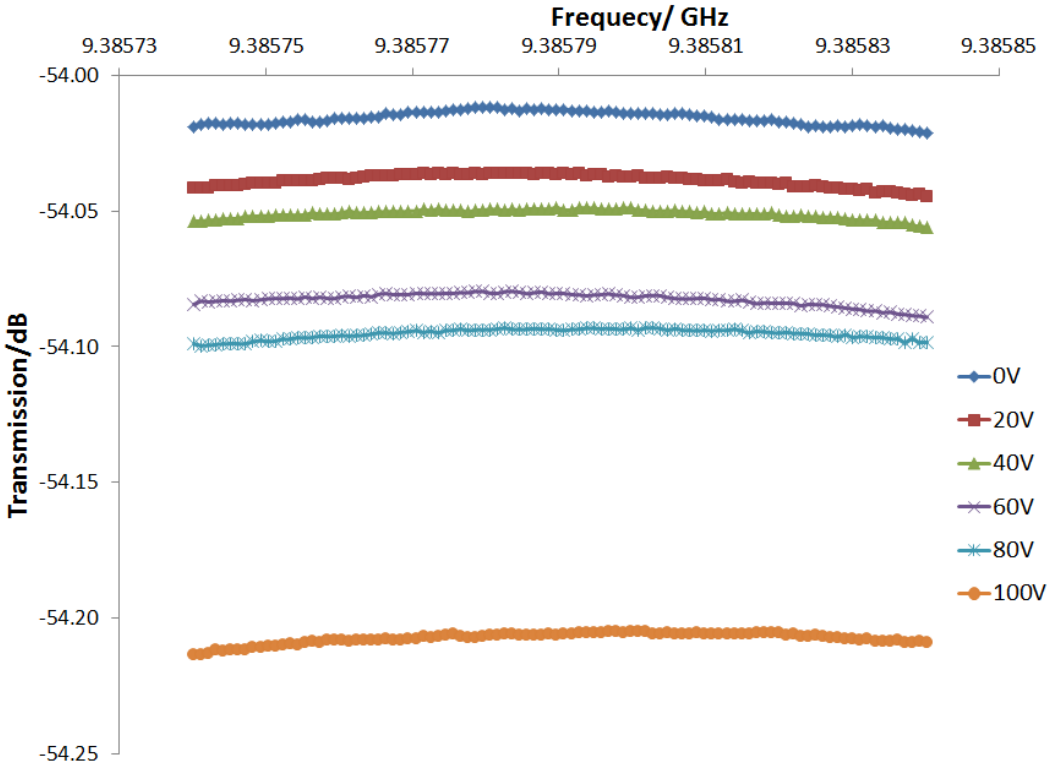

Figure 5-11: The microwave transmission spectra for different voltages applied.

Figure 5-11 shows the microwave transmission spectra for different voltages applied. The experimental results agree well with our prediction that as the external voltage increases, graphene becomes more conductive (lossy), which leads to a decrease in microwave transmission.

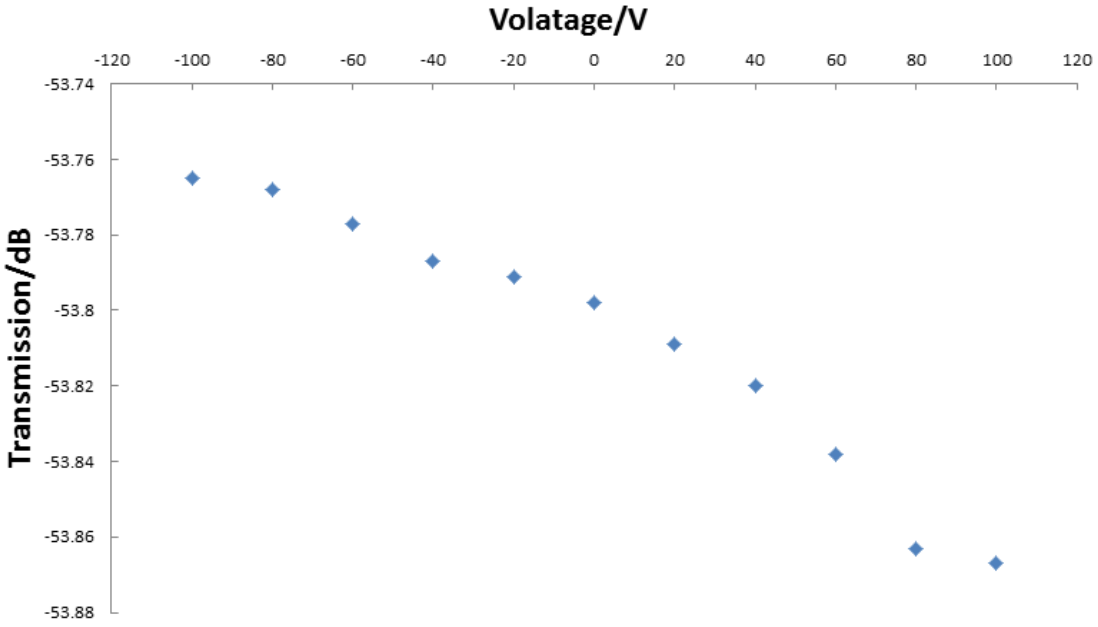

Figure 5-12: The microwave transmission coefficient at the resonant frequency for different voltages applied.

Figure 5-12 shows the microwave transmission coefficient at the resonant frequency for different voltages applied (both positive and negative). As the applied voltage goes to the positive end, the microwave transmission decreases, which is a strong evidence for the field effect.

The measured change in the resonator transmission coefficient can be converted into a change in sheet resistance: The transmission is proportional to the square of the quality factor, hence the difference between the losses in dB at a given gate voltage and gate voltage are directly related to the relative change in sheet resistance:

$$10^{0.1\times(T(U)-T(0))} = \left(\frac{R_S(U)}{R_S(0)}\right)^2 \quad \text{(Equation 5-7)}$$

According to the change of the transmission coefficient by -0.069 dB at 100 V, the corresponding relative change in sheet resistance is only about 1.6%.

5.3.4 Discussion

Intrinsic graphene is a semi-metal with no band gap. When the external voltage is applied between two graphene layers, the electric field will shift the Fermi levels of the two layers into opposite directions: both can enhance the carrier density of graphene and thus increases microwave losses of both graphene layers (Figure 5-13).

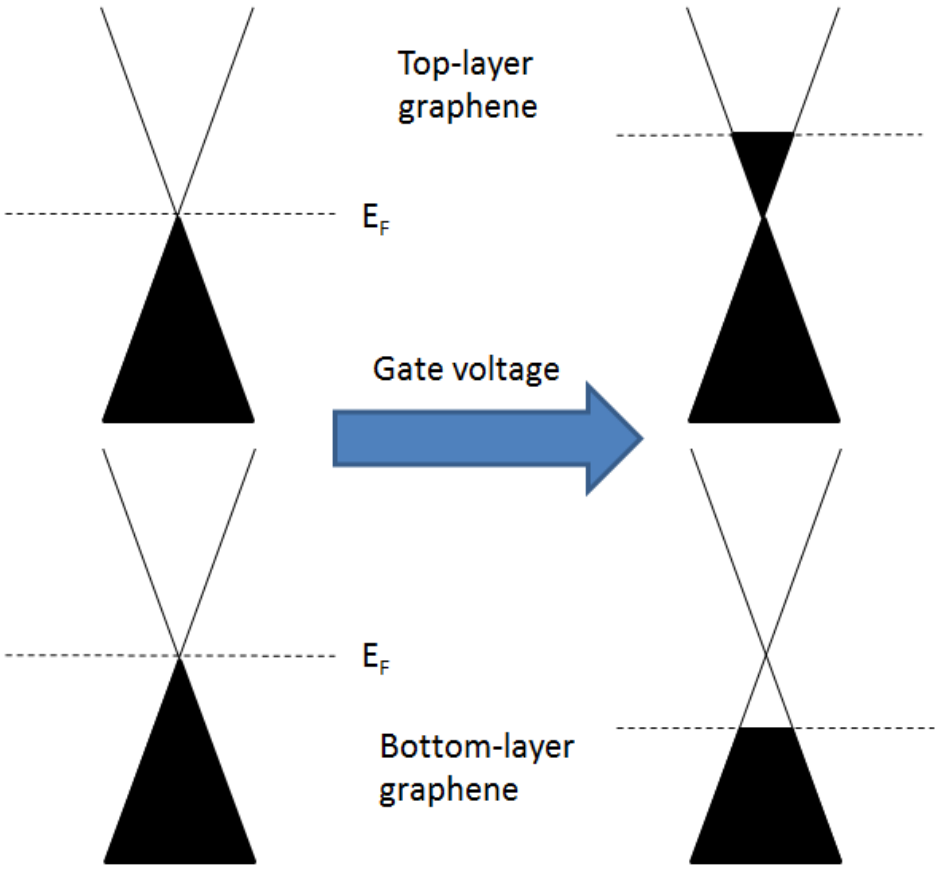

Figure 5-13: Schematic of the field effect in the double layer device.

However the observed microwave field effect in graphene is not very significant (only about 1.6 % change in sheet resistance at 100 V), which is much smaller than electrical field effect results in a similar electric field (100 V/400 nm =2.5 MV/cm). It is probably because the CVD graphene films are not pristine graphene with zero bandgap: instead, they are normally p-doped due to intensified effects of charged impurities due to strong interaction between the graphene and the supporting substrate [100], physically absorbed p-dopants from air (O_2, H_2O, and CO_2) [101] and attached PMMA film[102; 103].

When the external voltage is applied between two layers of p-doped graphene, the electric field will shift the Fermi levels of the two layers into opposite directions: the carrier density of one layer is increased while that of the other layer is decreased. Although the bottom layer of graphene has a larger effect on the microwave transmissions because it is nearer to the resonator, the net effect is quite small because the opposite effect from the top layer graphene offsets most of the changes in microwave transmissions. (Figure 5-14)

To make the microwave field-effect more observable, methods such as hetero atom doping[104; 105] or chemical modification[20; 106; 107] can be explored to offset the p-type doping effect and shift the Fermi level of the graphene back to the Dirac point.

Another factor to consider is the leakage current between the two graphene layers. As the wet transfer processes are not conducted in a clean room, the continuity or the insulation property of PMMA film might be damaged by dust particles. The leakage current between graphene layers can lead to a lower effective electrical field. The PMMA film should be spin-coated homogeneously in an ultra-clean environment to minimize defects. Although thicker PMMA layer normally offers better insulation, it also makes the field effect less notable. Further optimization of thickness as well as exploration of thinner dielectric materials with better insulation (larger dielectric constant) are needed to improve the device performance.

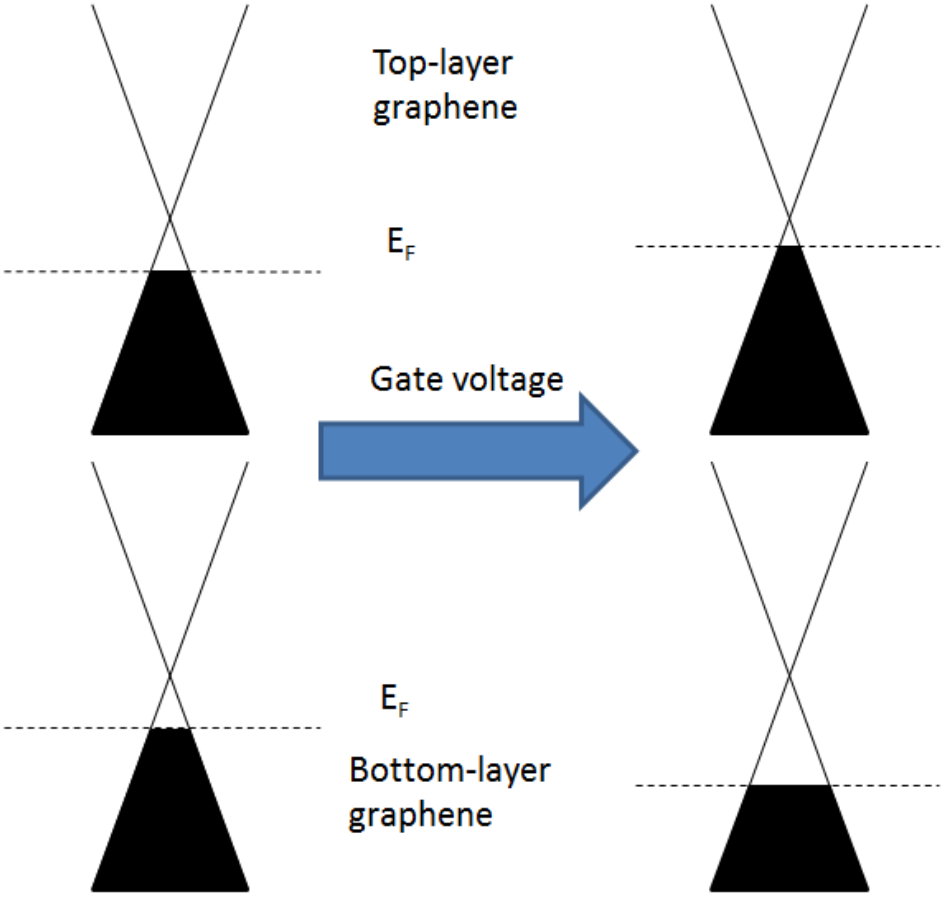

Figure 5-14: Schematic of the field effect in the double layer device (when the grown CVD graphene is p-doped).

5.4 Conclusions

The new microwave examination method enables contact-free determination of the sheet resistance of graphene in a convenient, accurate and low-cost way. It can be further extended to examinations of other conducting thin film materials or examination of the homogeneity over a large-area conducting sheet in a short period. Further advancements in the sensitivity and configuration of the resonator are still needed to improve the accuracy.

A large-area double-layer graphene device is fabricated and the field effect in graphene is indirectly observed with the microwave resonator. To make the microwave field-effect more significant, the p-type doping effect needs to be removed. Possible solutions include: adaptions in the synthesis and transfer processes, hetero atom doping or chemical modification.

The microwave examination method opens a new way to study graphene's properties as well as important references to further optimize the graphene synthesis and transfer processes. It is also fascinating to explore free-standing graphene's properties and field-effect with microwave examination, if proper free-standing structures had been fabricated and flexible microwave probe is available in the future.

6. Deposition of Strontium Titanate (STO) onto Graphene[4]

6.1 Aim and Purpose

The extraordinary electrical properties of graphene, including its ultra-high electron mobility of up to 200,000 cm^2/Vs [15; 16; 17] (which is ~100 times higher than silicon), the high current density of up to $\sim 2 \times 10^8$ $A\,cm^{-2}$ [18] and a high saturation velocity of up to 5.5×10^7 $cm\,s^{-1}$ [19], has made graphene a promising material for high speed FET transistors and super capacitors.

Most graphene FET transistors employ a Si (doped) substrate as the back gate electrode and SiO_2 as gate dielectric. It is chosen mainly because graphene on this substrate is visible under optical microscope, which facilitates the characterization and device fabrication processes. [67; 68] (See section 3.2.1 Optical Microscope for more details)

Although back-gated graphene FET transistors are convenient for basic research, they have several drawbacks.

1. The large thickness (300 nm) and small dielectric constant of the back gate dielectric material (SiO_2) require a high operational voltage [99; 108; 109].

2. Using the substrate as the back gate means lack of control on individual devices because all devices on the whole wafer would be switched on and off simultaneously, which is inappropriate for industrial applications.

3. To achieve optical interference, there is a limited range of SiO_2 thickness.

[4] Parts of this chapter are in submission preparation.

Top-gate FET transistors, however, requires direct deposition of dielectric materials (normally oxides) on top of graphene. On the other hand, in order to fabricate graphene super capacitors with high capacitance [110; 111; 112], it is also crucial to deposit dielectric materials on top of graphene without damaging the graphene.

Strontium Titanate ($SrTiO_3$ or STO) is an incipient ferroelectric material (paraelectric at room temperature) with a large dielectric constant: κ(STO) = ~300 at room temperature while $\kappa(SiO_2)$ = ~3.9. The high dielectric constant makes STO a desirable dielectric material for graphene: (1) the low leakage current can lead to better performances of graphene devices and possibility of thinner dielectric layer / lower operational voltage; (2) higher capacitance for graphene super-capacitors.

The deposition process of Strontium Titanate normally involves deposition and annealing in oxygen at high temperatures. The annealing step is crucial to form high quality oxide films, but can also cause significant defects to graphene. The interaction between graphene and oxygen under different temperatures and oxygen partial pressures is studied to optimize the STO deposition conditions and to minimize the damage of graphene.

One the one hand, the electrical properties and microstructure of STO thin films strongly depend on the deposition conditions, especially the deposition temperature[113] and oxygen partial pressure[114]: as the deposition temperature increases, the STO grains become larger and more uniform (Figure 6-1) while the high oxygen partial pressure can lead to better crystalline quality. On the other hand, high temperature and high oxygen partial pressure during the deposition can cause significant defects to graphene. The interaction between graphene and oxygen under different temperatures and oxygen partial pressures was studied to optimize the STO deposition conditions and to minimize the damage of graphene.

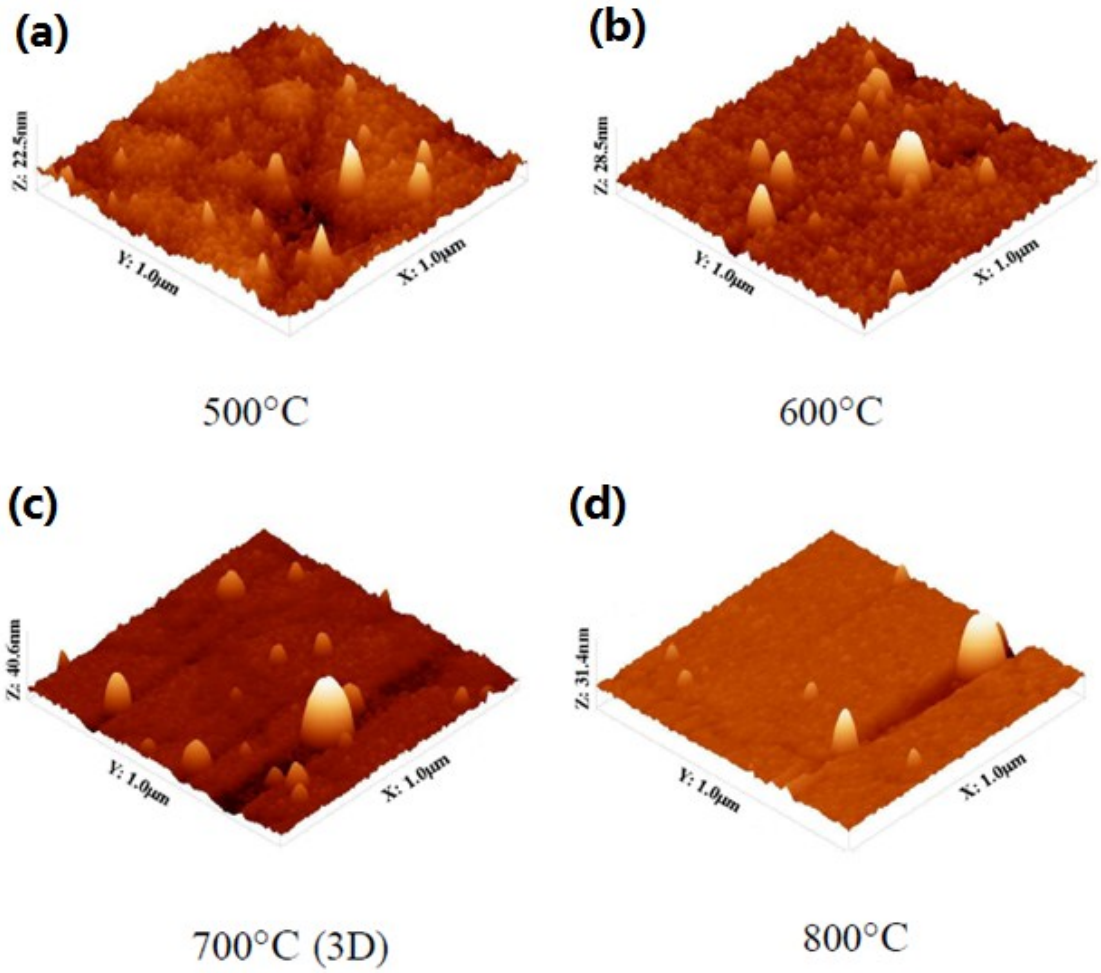

Figure 6-1: 3D AFM images of STO films deposited under different temperatures: as the deposition temperature increases, the STO grains become larger and more uniform.

(Adapted from reference [113])

6.2 Methods

6.2.1 The oxidation treatment test

(1) Graphene growth and transfer:

CVD-grown graphene films are transferred onto SiO_2 substrates, after which the samples are placed in a high vacuum chamber (Figure 6-2).

(2) Removal of air:

The vacuum chamber is pumped to base pressure (~10^{-7}mTorr) and filled will high purity argon gas several times to remove air residues.

(3) Flow in oxygen gas:

The vacuum chamber is then pumped to base pressure again and filled with high purity oxygen gas of given oxygen partial pressure.

(4) Heat treatment:

The graphene sample is then heated to given temperature and last for 1 hour.

(5) Cooling down:

After cooling down to room temperature, the graphene sample is collected from the high vacuum chamber for characterizations.

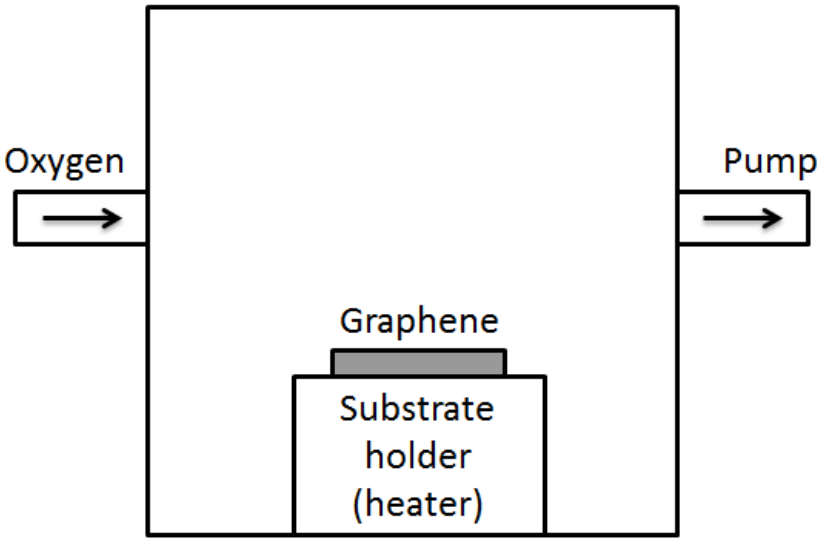

Figure 6-2: Schematic of the high vacuum chamber.

6.2.2 The deposition of STO films

(1) Graphene growth and transfer:

CVD-grown graphene films are transferred onto MgO substrates (MgO is widely used as a epitaxial substrate for STO deposition [113]), after which the samples are placed in a high vacuum PLD chamber.

(2) Removal of air:

The vacuum chamber is pumped to the base pressure (~10^{-7} mTorr) and filled will high purity argon gas several times to remove air residues.

(3) Flow in oxygen gas:

The vacuum chamber is then pumped to base pressure again and filled with high purity oxygen gas of a given oxygen partial pressure (in the range of 0-500 mTorr).

(4) The PLD deposition

The STO film is then deposited at a given deposition temperature (in the range of 0-850 ℃).

(5) Post-deposition annealing

After the deposition process, the substrate is cooled down to the annealing temperature (normally 600 ℃) and oxygen partial pressure (in the range of 0-500 mTorr) for 1 hour.

(6) Cooling down:

After slowly cooling down to room temperature (~10 °C/min), the deposited film is collected from the high vacuum chamber for characterizations.

6.2.3 Characterization

(1) Electrical measurement

Two-probe electrical measurements (probe spacing: 1 mm) are conducted before and after each oxygen treatment to determine the effects on resistances.

(2) Structural measurement

XRD is conducted to examine the crystalline of deposited STO films.

SEM is employed to observe the structural changes before and after oxygen treatment.

(3) Raman measurement

Raman measurement is conducted to determine the defects introduced by oxygen treatment.

6.3 Results and Discussion

6.3.1 Effects of temperature and oxygen partial pressure

Electrical measurement

Figure 6-3 shows changes in graphene sheet resistance before and after oxidation test at different temperatures (O_2 partial pressure = 100 mTorr). When the temperature is below 650 °C, no significant change is observed. However when the temperature reaches 650 °C, graphene's sheet resistance begins to degrade rapidly. When temperature rises to above 700 °C, graphene becomes almost insulating.

Figure 6-4 shows changes in graphene sheet resistance before and after oxidation test under different O_2 partial pressures (Temperature: 600 °C). As O_2 partial pressure rises, graphene's conductivity also degrades.

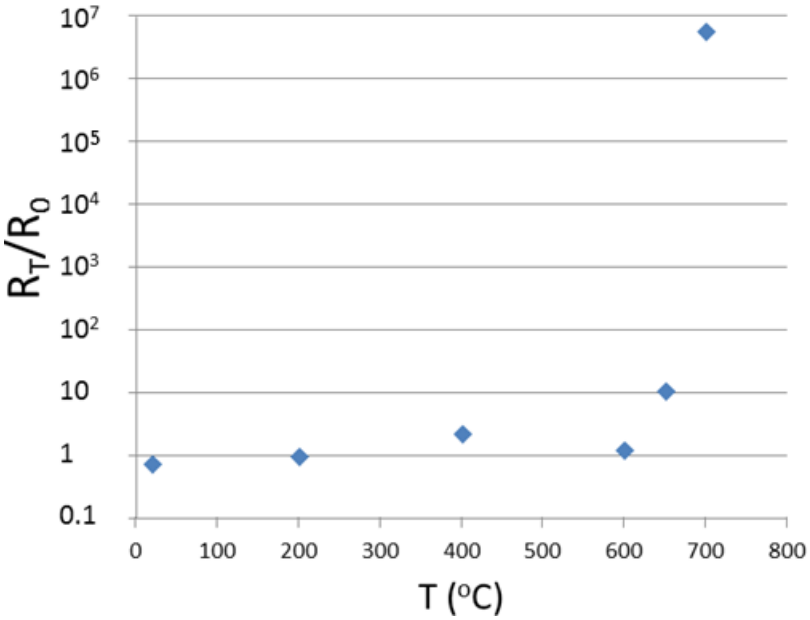

Figure 6-3: Resistances of graphene samples before (R_0) and after oxidation treatment (R_T) under different temperatures (O_2 partial pressure = 100 mTorr).

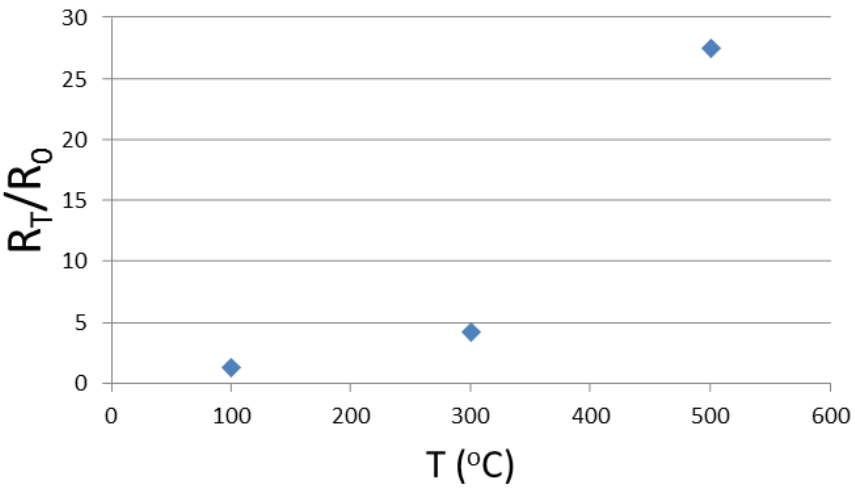

Figure 6-4: Resistances of graphene samples before (R_0) and after oxidation treatment (R_T) under different O_2 partial pressures. (Temperature: 600 ℃)

Raman measurement

Figure 6-5 and Figure 6-6 show Raman spectra before and after oxidation test at different temperatures (O_2 partial pressure = 100 mTorr). The intensity of D band increases as the temperature rises. Figure 6-7 shows Raman spectra before and after oxidation test under different O_2 partial pressures (Temperature: 600 ℃). As O_2 partial pressure rises, graphene's D band intensity also increases. These spectra suggest that the graphene defects can easily form in high temperatures and high oxygen partial pressures, which corresponds to the electrical measurement data above.

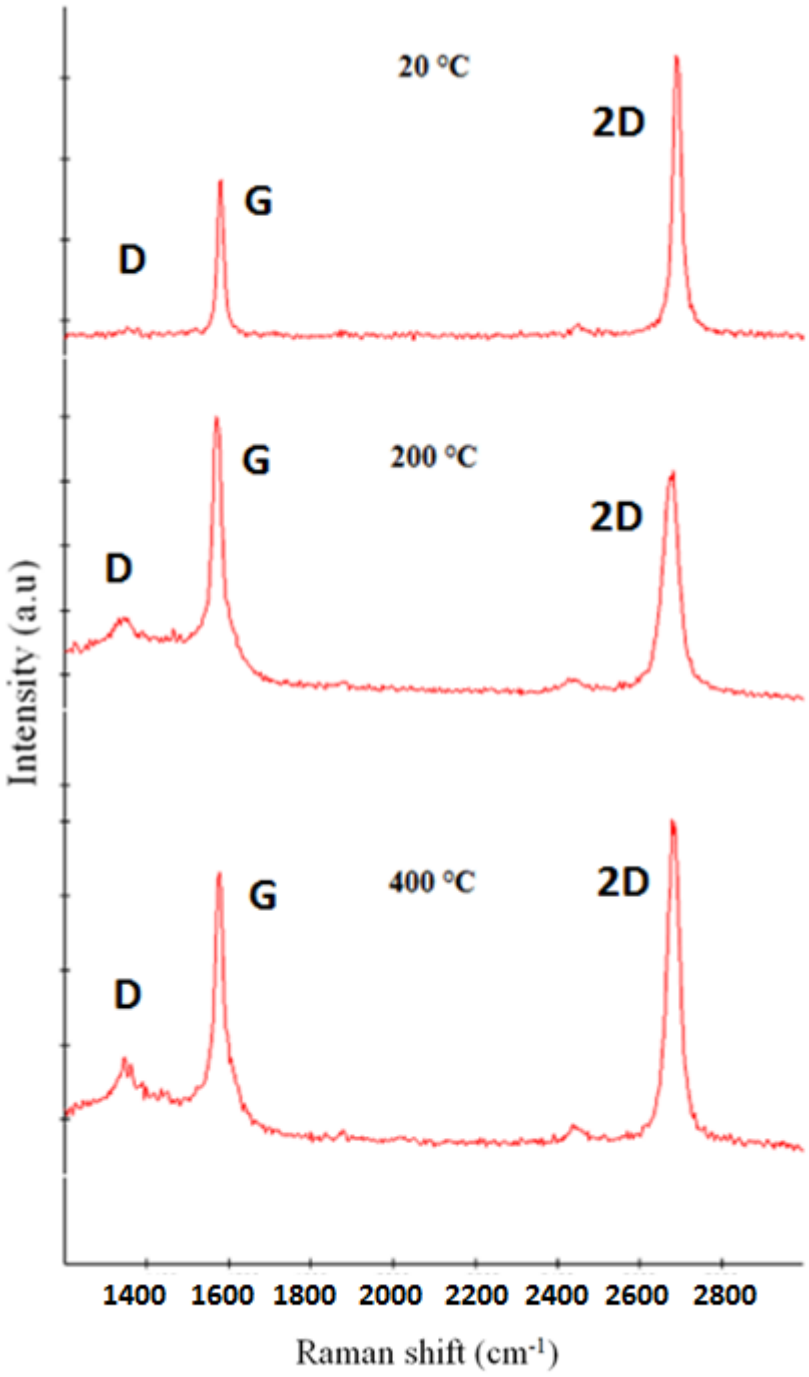

Figure 6-5: Raman spectra of graphene samples before and after oxidation treatment under low temperatures (20 °C, 200 °C, 400 °C. O_2 partial pressure = 100 mTorr).

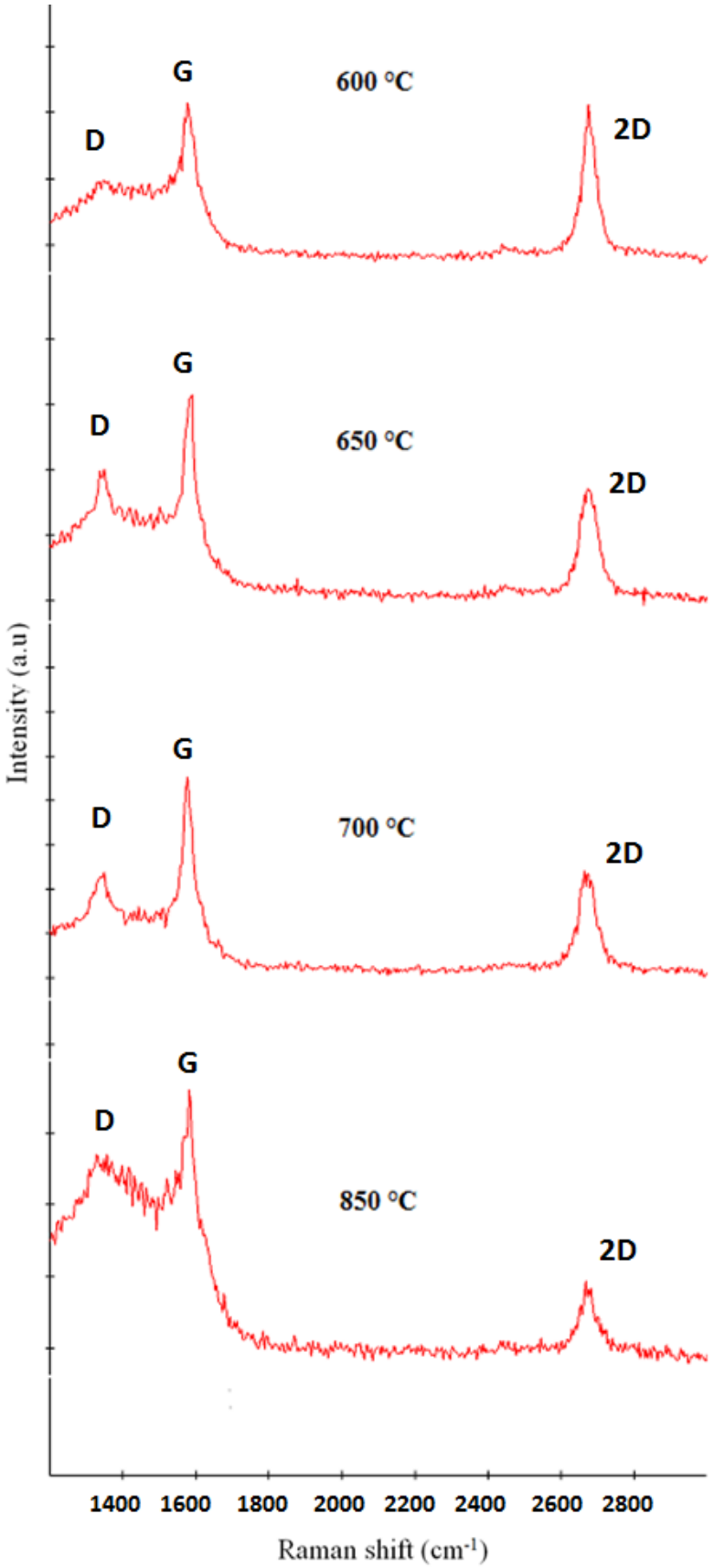

Figure 6-6: Raman spectra of graphene samples before and after oxidation

treatment under high temperatures (600 °C, 650 °C, 700 °C, 850 °C. O_2 partial pressure = 100 mTorr).

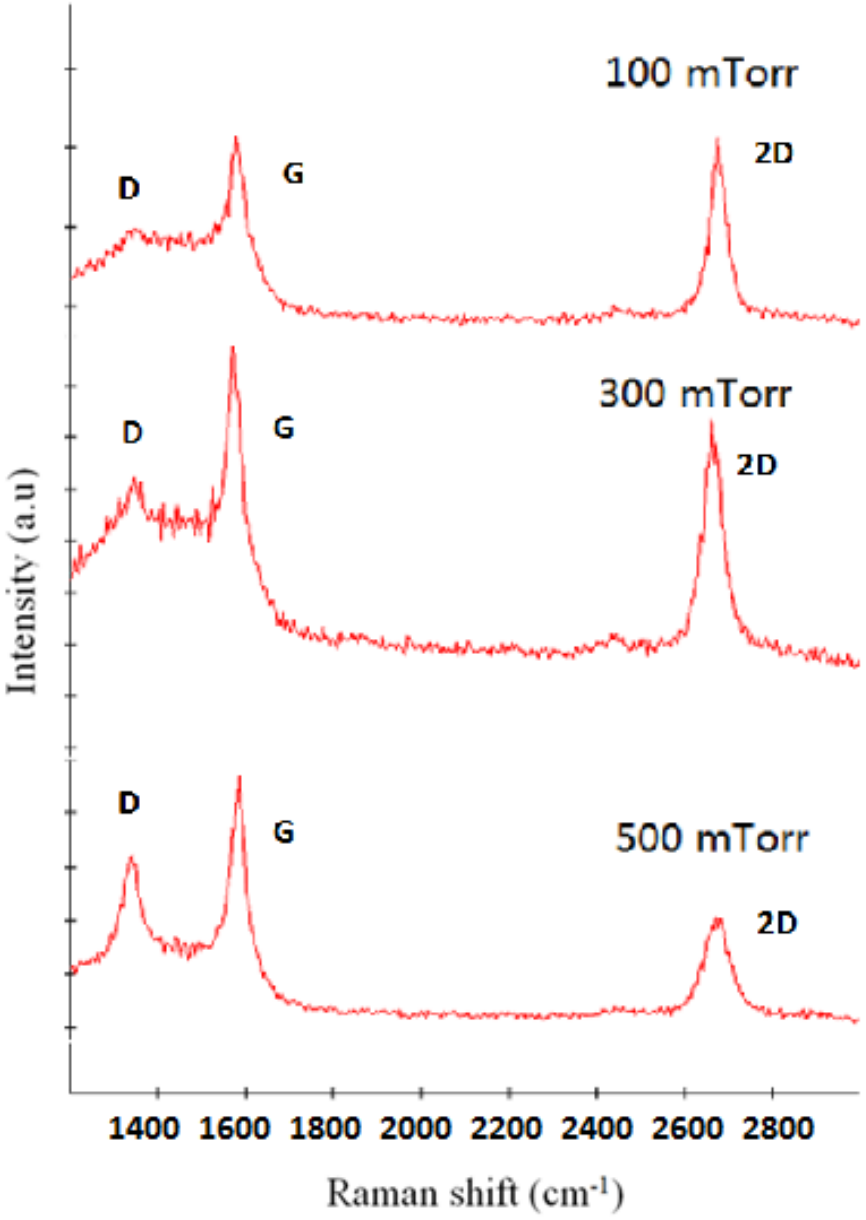

Figure 6-7: Raman spectra of graphene samples before and after oxidation treatment under different O_2 partial pressures. (Temperature: 600 °C)

SEM characterization

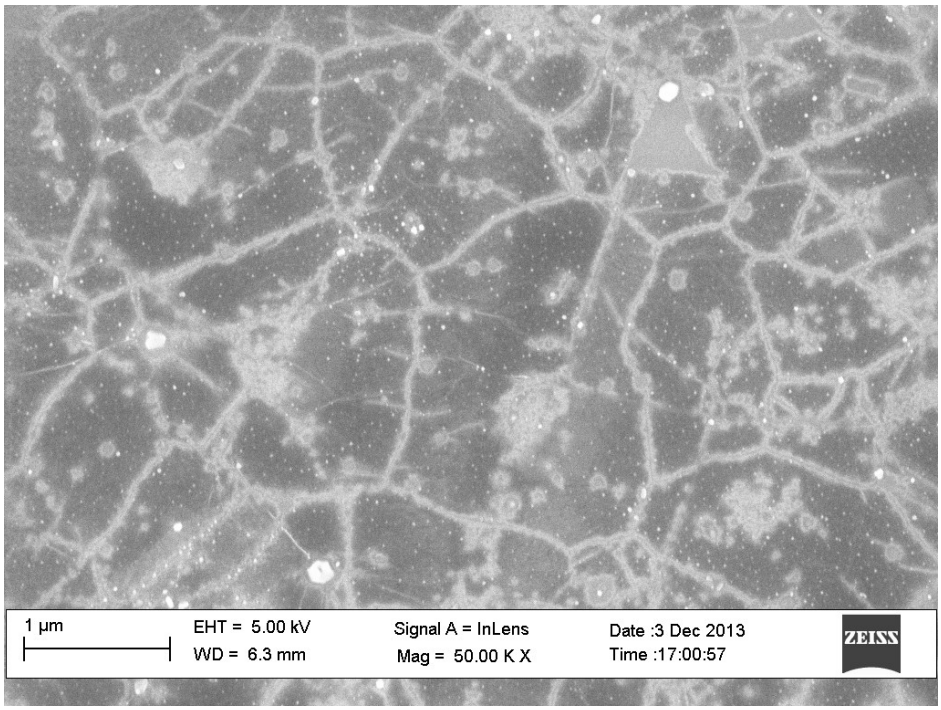

Figure 6-8: A typical SEM image of graphene on SiO_2/Si after oxidation treatment at 700 °C (O_2 partial pressure = 100 mTorr).

Figure 6-8 is a typical SEM image of a graphene sample with defects after the oxidation treatment. The damages parts can be clearly observed. It is interesting to find that oxidation starts from graphene grains boundaries. The oxidation mechanism will be further studied in future works.

6.3.2 Optimizations of the deposition process

The normal PLD process to deposit STO involves high temperature (850 °C) and

oxygen environment (O_2 partial pressure > 100 mTorr) (Figure 6-9). According to our previous oxidation test studies, the graphene will be significantly damaged in these conditions.

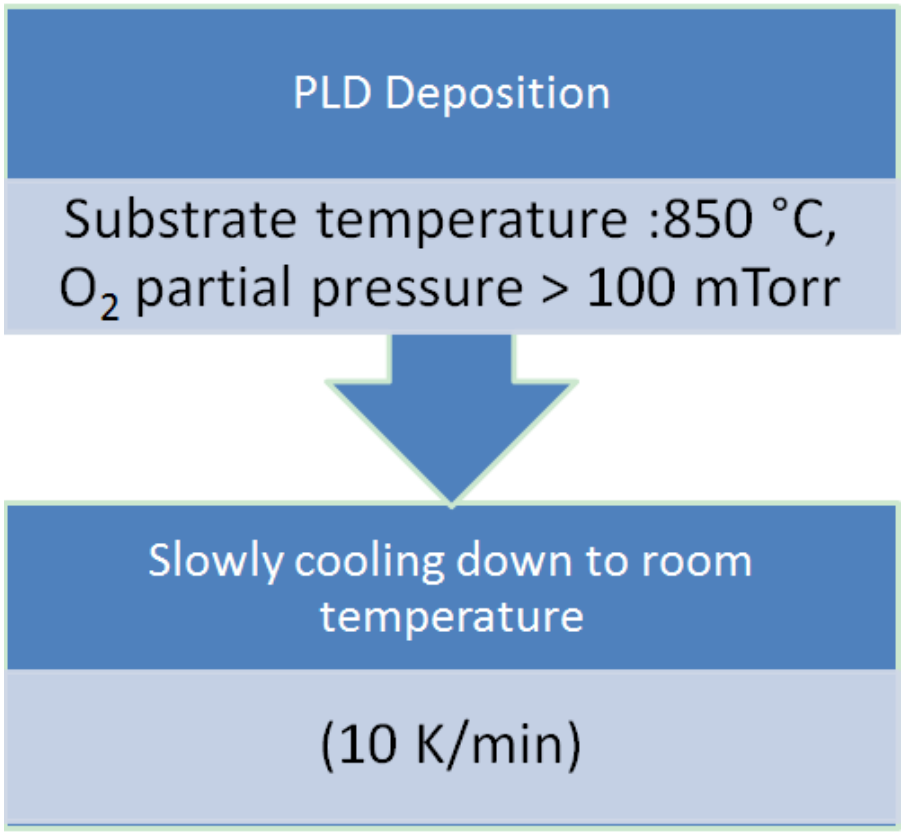

Figure 6-9: Schematic of the typical PLD process to deposit STO

To minimize the graphene's damage during STO deposition, we adapted the conditions based on oxidation test results. As shown in Figure 6-10, the deposition is first conducted in ultra-high vacuum to protect graphene from oxidation. Then the substrate is cooled to a lower temperature (600 °C) and annealed, during which the oxygen atoms are supplemented into the film. (The oxygen partial pressure is set to be 100 mTorr to prevent serious damages from graphene.) At last, the substrate is slowly

cooled down to room temperature and characterized.

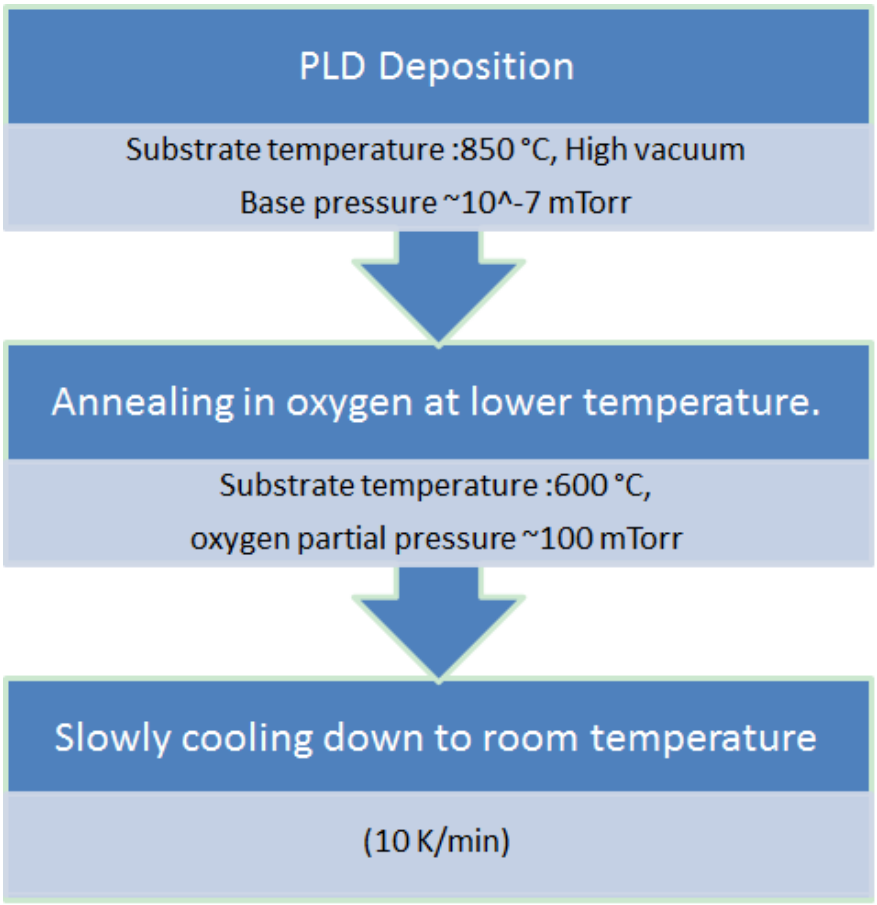

Figure 6-10: Schematic of the adapted PLD process to deposit STO

6.3.3 Characterizations of the deposited STO/graphene/MgO structure

Figure 6-11 shows the continuous STO film deposited on graphene/MgO. Figure 6-12

shows the XRD pattern of the STO/Graphene/MgO structure. Both of them confirm good crystalline quality of the deposited STO films.

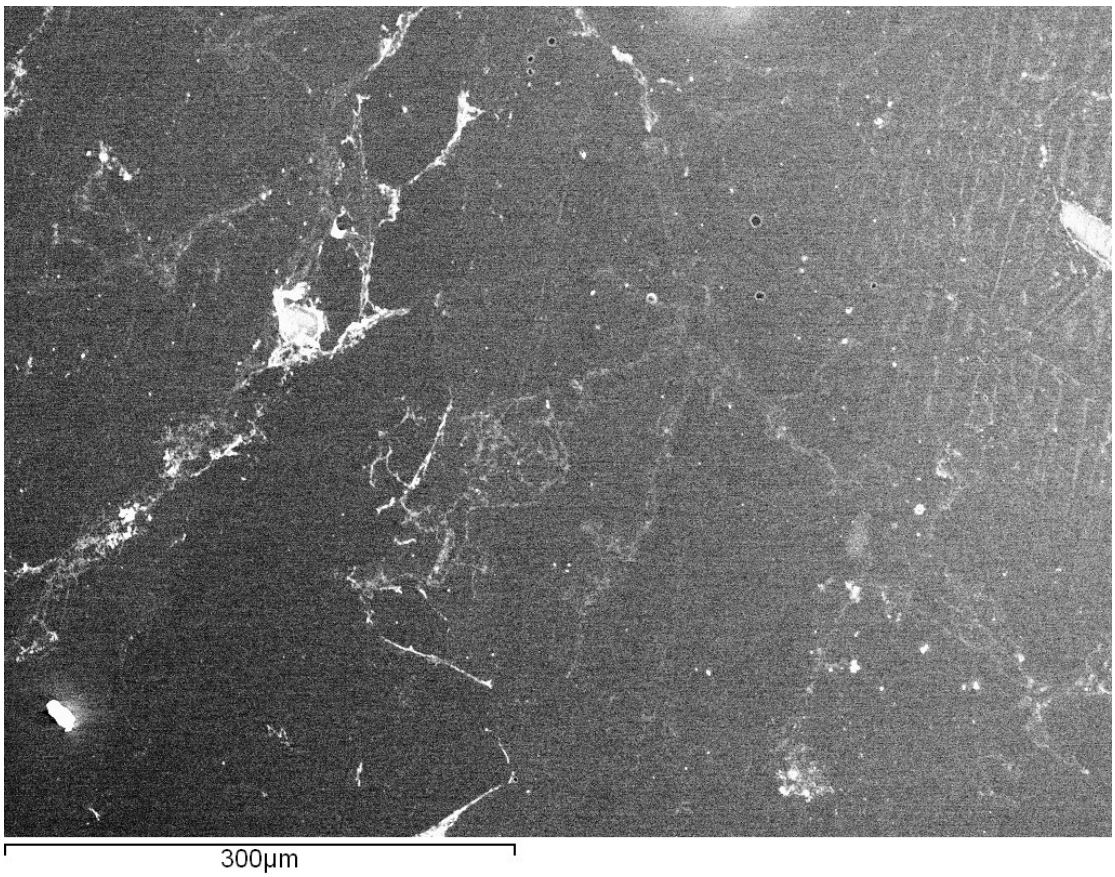

Figure 6-11: SEM image of the STO/Graphene/MgO structure

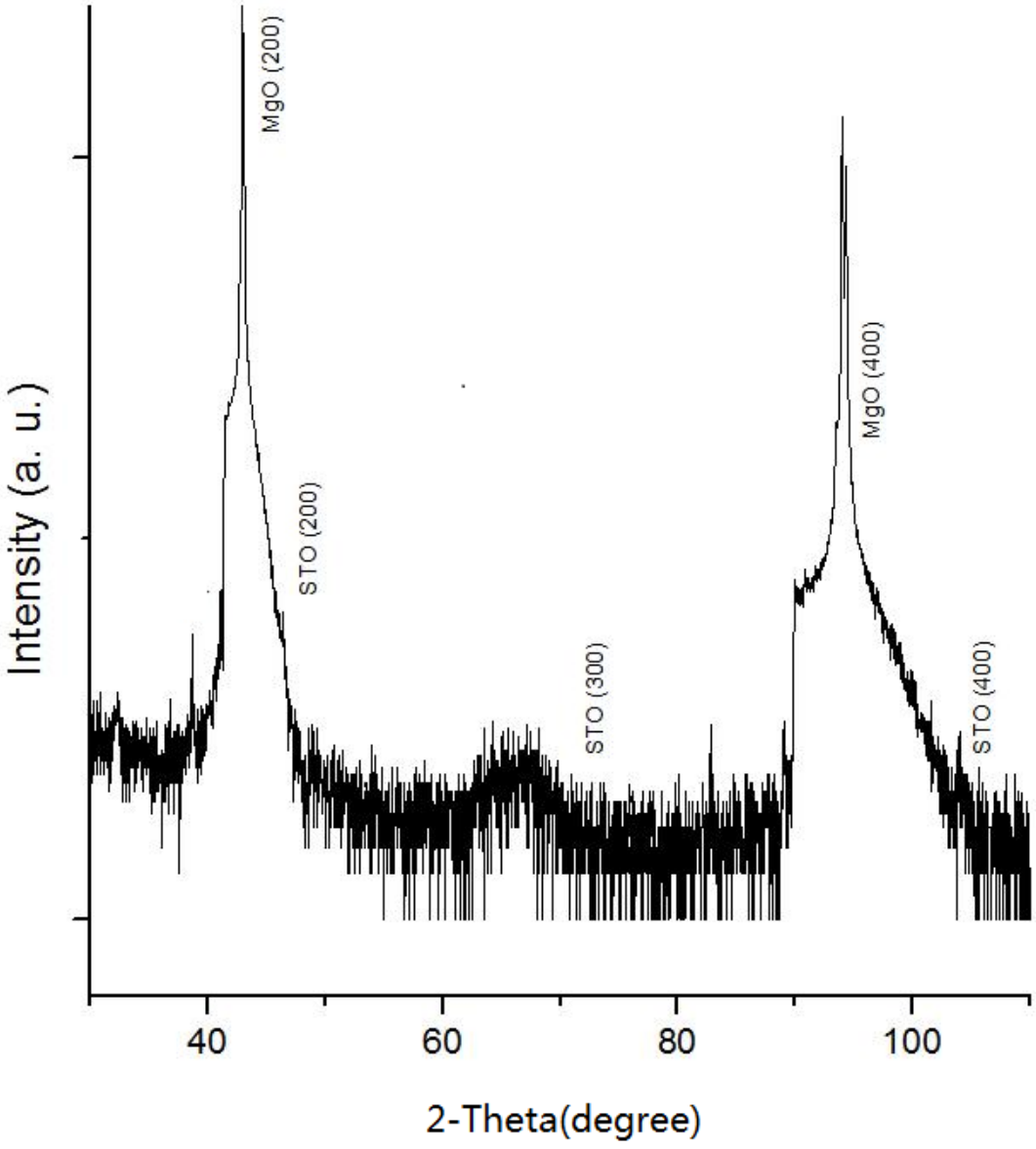

Figure 6-12: XRD pattern of the STO/Graphene/MgO structure

Figure 6-13 and Figure 6-14 are the Raman data of the STO/Graphene/MgO structure. The graphene G band and 2D band can be detected over the whole mapping area, suggesting that graphene have "survived" the deposition process.

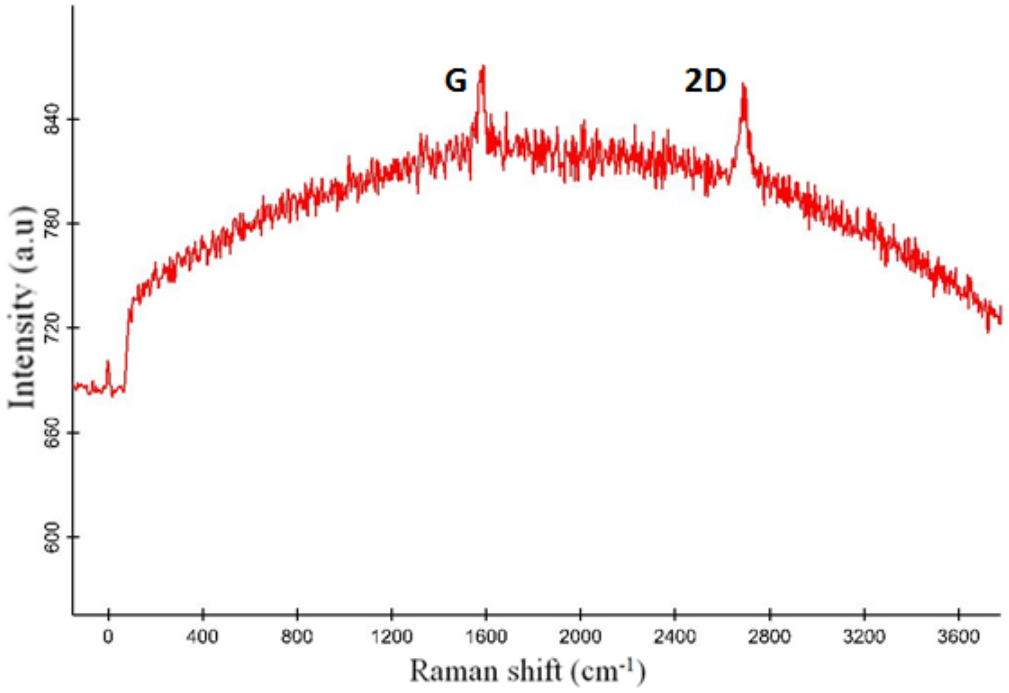

Figure 6-13: Raman spectrum of the STO/Graphene/MgO structure

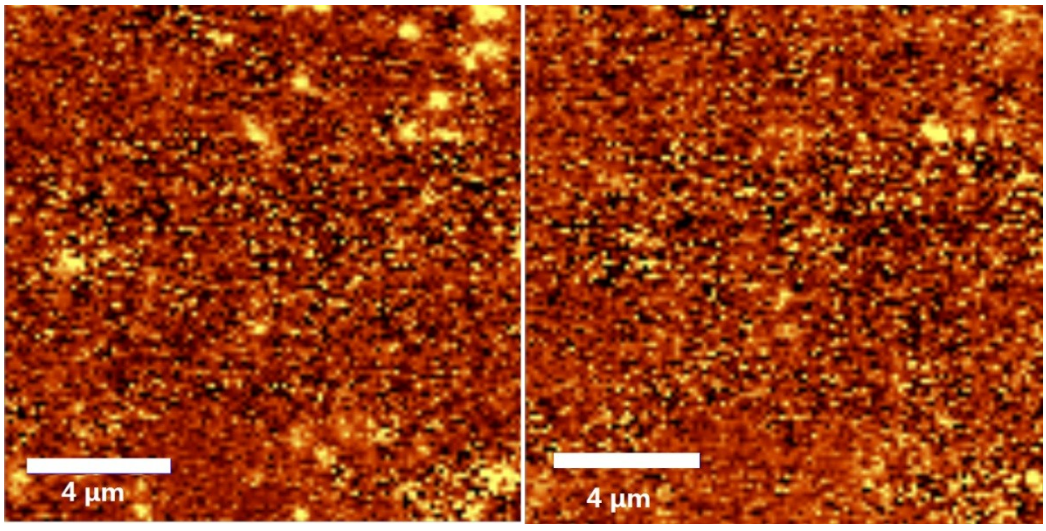

Figure 6-14: G band (left) and 2D band (right) Raman mapping of the STO/Graphene/MgO structure.

6.4 Conclusions

In summary, the interaction between graphene and oxygen under different temperatures and oxygen partial pressures is studied and discussed. Strontium Titanate (STO) film is deposited on transferred CVD grown graphene on MgO substrate. Based on the oxidation test results, the deposition process of Strontium Titanate is optimized to minimize the defects introduced on graphene. Raman mapping data show that graphene is still continuous after the STO deposition although D band suggests some newly formed defects.

The deposited STO/Graphene/MgO structure can be further fabricated into graphene capacitors and other devices. Further optimizations are still needed to improve the performance. One possible solution is to introduce a protection layer on graphene before the STO deposition.

Due to limitations of time and graphene growth facilities, the oxidation study is only conducted on CVD grown graphene. This study can be further extended to graphene grown by other methods, such as mechanically exfoliated graphene and epitaxial grown graphene. This study also offers a new method to deposit other oxide dielectrics on graphene.

7. Conclusions

7.1 Summary

This thesis has been focused on three areas: large-area synthesis and transfer of graphene films, the microwave characterization and the fabrication of novel graphene devices/structures.:

(1) Large-area synthesis and transfer of graphene films

The parameters of the CVD growth of graphene and the transfer processes are explored and optimized. Large-area, continuous and high quality monolayer graphene is obtained. A novel frame-assisted method is developed to cover whole substrate with graphene with less defects and impurities. To remove PMMA residues more effectively and unharmfully, thermal annealing and acetone treatments are combined to obtain a clean graphene surface.

(2) Microwave characterization of graphene films

The new microwave examination method enables contact-free determination of the sheet resistance of graphene in a convenient, accurate and low-cost way. The microwave examination method opens a new way to study graphene's properties as well as important references to further optimize the graphene synthesis and transfer processes.

Preliminary explorations to examine the field effect in graphene by the microwave resonator are conducted. A small change in graphene's sheet resistance is observed

when a range of external voltages are applied.

(3) Fabrication of novel graphene devices/structures

Strontium Titanate (STO) film is successfully deposited onto monolayer graphene sheets on MgO substrates. The interaction between graphene and oxygen under different temperatures and oxygen partial pressures is studied and discussed. Based on the oxidation test result, the deposition process of Strontium Titanate is optimized to minimize the defects introduced on graphene as well as to guarantee good crystalline quality of STO. The STO/graphene structure can be easily fabricated into devices such as capacitors. This study also offers a new route to deposit other oxide dielectrics on graphene.

A new route to fabricate graphene free-standing structure is proposed. Preliminary results suggest that the under-etching method is promising to remove the underlying copper and leave the patterned photoresist/graphene structure suspended. Further adaptions in mask design and critical point drying techniques are still needed to prevent damages in graphene.

A large-area double-layer graphene device is fabricated to detect the field effect in graphene with the microwave resonator. Each graphene layer replaces metal as the gate electrode for the other graphene layer. This novel structure also enables examination of the field effect in both graphene layers at the same time.

7.2 Future outlook

The conductivity of synthesized graphene is still lower than mechanically exfoliated ones and the growth and transfer processes need to be further studied and optimized. Possible ways include: utilising atomic-smooth single crystal copper as growing substrate, and plasma-enhanced CVD facilities to reduce the growth temperature. The novel microwave characterization technique also provides a new reference in growth and transfer optimizations to obtain graphene with the best electrical properties.

Further advancements in the sensitivity and configuration of the microwave resonator are still needed to improve the accuracy of the microwave characterizations. This technique can also be further extended to examinations of other conducting thin film materials or examination of the homogeneity over a large-area conducting sheet in a short period. To make the microwave field-effect more significant, the p-type doping effect needs to be reduced or removed. Possible solutions include: adaptions in the synthesis and transfer processes, hetero atom doping or chemical modification. Replace PMMA with other dielectric materials can also help reducing the p-type doping as well as the leakage current.

The fabrication of a graphene free-standing structure can be further explored and optimized by growing graphene directly on copper thin films, adaptations in mask designs and the employment of critical point drying technique to minimize graphene damage during photoresist removal. It is also fascinating to explore free-standing graphene's properties and field-effect with the microwave technique.

The deposited STO/Graphene structure can be further fabricated into graphene capacitors. Further optimizations of deposition process are still needed to improve the performance.

8. Appendix

8.1 Derivation of the formula for the sheet resistance calculation

For ultra-thin film materials like graphene (thickness t <<probe spacing s), the current distribution can be assumed as ring shaped. A ($A = 2\pi xt$) represent the cross section of the ring at a given distance x in between the contacts at x_1 and x_2 (Figure 3-13):

$$R = \int_{x1}^{x2} \rho \frac{dx}{2\pi xt} = \int_{s}^{2s} \frac{\rho}{2\pi t} \frac{dx}{x} = \frac{\rho}{2\pi t} ln2 \quad \text{(Equation 8-1)}^{[78]}$$

As $R = \frac{V}{2I}$, the sheet resistivity can be expressed as

$$\rho = \frac{\pi t}{ln2} \left(\frac{V}{I}\right) \quad \text{(Equation 8-2)}^{[78]}$$

Finally, the sheet resistance

$$R_S = \frac{\rho}{2t} = 4.53\left(\frac{V}{I}\right) \text{(Equation 3-1)}^{[78]}$$

8.2 Measured sheet resistances for different CVD graphene samples transferred onto quartz substrates

No.	R_S1 (Ω /sq)	R_S2 (Ω /sq)	R_S(average) (Ω /sq)
1	876	815	846
2	2,009	1,971	1,990
3	871	1,084	978
4	1,152	1,116	1,134
5	902	873	888
6	910	1,001	956
GS1	1,959	2,038	1,998
GS2	1,240	1,289	1,265

Table 8-1: Measured sheet resistances for different CVD graphene samples transferred onto quartz substrates.

Samples 1 to 6 are as grown CVD graphene samples transferred onto quartz substrates using the standard recipe described in section 4.1.2 The CVD Procedures. Samples GS1 and GS2 are CVD grown graphene samples (on copper) bought from graphene supermarket, which were transferred in the same method onto the same substrate as comparisons.

8.3 Calibration of the coefficient Z_c in the microwave measurement

No.	Q	$1/\Delta(Q^{-1})$	R_S (Ω /sq)
1	4,830	9,114	846
2	7,059	22,548	1,990
3	5,308	10,979	978
4	5,696	12,780	1,134
5	5,160	10,364	888
6	5,235	10,671	956
GS1	7,166	23,678	1,998
GS2	6,139	15,249	1,265

Table 8-2: Measured Q values, calculated $1/\Delta(Q^{-1})$ values and measured sheet resistances for different CVD graphene samples transferred onto quartz substrates.

Samples 1 to 6 are as grown CVD graphene samples transferred onto quartz substrates using the standard recipe described in section 4.1.2 The CVD Procedures. Samples GS1 and GS2 are CVD grown graphene samples (on copper) bought from graphene supermarket.

The Q value of a blank quartz substrate is also measured as comparison. $Q_{Quartz} =$

10276.

The inversed change of Q-factor for each sample can then be calculated:

$$1/\Delta Q^{-1} = 1/(\frac{1}{Q_{gr}} - \frac{1}{Q_{Quartz}})$$

The results of calculated $1/\Delta(Q^{-1})$ values and DC measured sheet resistances are listed in

Table 8-2.

8.4 Resistances of graphene films before and after oxidation treatment

Temperature (℃)	Resistivity Before Treatment (Ω/sq)	Standard Error	Resistivity After Treatment (Ω/sq)	Standard Error	Normalized to no treatment
700	5015	837	29464390000	1549770000	5875319.7
650	7131	1900	76195	23728	10.7
600	3506	610	4288	402	1.2
400	3938	442	8958	602	2.3
200	4044	599	3897	386	1.0
20	5567	592	4096	758	0.7

Table 8-3：Sheet resistance of graphene samples before and after oxidation treatment under different temperatures (O_2 partial pressure = 100 mTorr).

O_2 partial pressure (mTorr)	Sheet Resistance Before Treatment (Ω/sq)	Standard Error	Sheet Resistance After Treatment (Ω/sq)	Standard Error	Normalized to no treatment
100	3506	610	4288	402	1.2

300	4542	1071	18737	3354	4.1
500	8786	1565	241951	261924	27.5

Table 8-4: Sheet resistance of graphene samples before and after oxidation treatment under different O_2 partial pressures. (Temperature: 600 ℃)

References

[1] Geim, A. K. and K. S. Novoselov (2007). "The rise of graphene." Nat Mater **6**(3): 183-191.

[2] Novoselov, K. S., A. K. Geim, et al. (2004). "Electric Field Effect in Atomically Thin Carbon Films." Science **306**(5696): 666-669.

[3] Neerinck, D. G. and T. J. Vink (1996). "Depth profiling of thin ITO films by grazing incidence X-ray diffraction." Thin Solid Films **278**(1–2): 12-17.

[4] Yu, M.-F., O. Lourie, et al. (2000). "Strength and Breaking Mechanism of Multiwalled Carbon Nanotubes Under Tensile Load." Science **287**(5453): 637-640.

[5] Lee, C., X. Wei, et al. (2008). "Measurement of the Elastic Properties and Intrinsic Strength of Monolayer Graphene." Science **321**(5887): 385-388.

[6] Bae, S., H. Kim, et al. (2010). "Roll-to-roll production of 30-inch graphene films for transparent electrodes." Nat Nano **5**(8): 574-578.

[7] Cai, L., L. Song, et al. (2013). "Super-stretchable, Transparent Carbon Nanotube-Based Capacitive Strain Sensors for Human Motion Detection." Sci. Rep. **3**.

[8] Nair, R. R., P. Blake, et al. (2008). "Fine Structure Constant Defines Visual Transparency of Graphene." Science **320**(5881): 1308.

[9] Thuau, D., I. Koymen, et al. (2011). "A microstructure for thermal conductivity measurement of conductive thin films." Microelectronic Engineering **88**(8): 2408-2412.

[10] Pop, E., D. Mann, et al. (2005). "Thermal Conductance of an Individual Single-Wall Carbon Nanotube above Room Temperature." Nano Letters **6**(1): 96-100.

[11] Nika, D. L., S. Ghosh, et al. (2009). "Lattice thermal conductivity of graphene flakes: Comparison with bulk graphite." Applied Physics Letters **94**: 203103.

[12] Li, X., Y. Zhu, et al. (2009). "Transfer of Large-Area Graphene Films for High-Performance Transparent Conductive Electrodes." Nano Letters **9**(12): 4359-4363.

[13] Kim, H. S., M.-G. Kim, et al. (2009). "Low-Temperature Solution-Processed Amorphous Indium Tin Oxide Field-Effect Transistors." Journal of the American Chemical Society **131**(31): 10826-10827.

[14] Dürkop, T., S. A. Getty, et al. (2003). "Extraordinary Mobility in Semiconducting Carbon Nanotubes." Nano Letters **4**(1): 35-39.

[15] Morozov, S. V., K. S. Novoselov, et al. (2008). "Giant Intrinsic Carrier Mobilities in Graphene and Its Bilayer." Physical Review Letters **100**(1): 016602.

[16] Novoselov, K. S., A. K. Geim, et al. (2005). "Two-dimensional gas of massless Dirac fermions in graphene." Nature **438**(7065): 197-200.

[17] Bolotin, K. I., K. J. Sikes, et al. (2008). "Ultrahigh electron mobility in suspended graphene." Solid State Communications **146**(9-10): 351-355.

[18] Murali, R., Y. Yang, et al. (2009). "Breakdown current density of graphene nanoribbons." Applied Physics Letters **94**: 243114.

[19] Meric, I., M. Y. Han, et al. (2008). "Current saturation in zero-bandgap, top-gated

graphene field-effect transistors." Nat Nano **3**(11): 654-659.
[20] Schedin, F., A. K. Geim, et al. (2007). "Detection of individual gas molecules adsorbed on graphene." Nat Mater **6**(9): 652-655.
[21] Novoselov, K. S., D. Jiang, et al. (2005). "Two-dimensional atomic crystals." Proceedings of the National Academy of Sciences of the United States of America **102**(30): 10451-10453.
[22] Viculis, L. M., J. J. Mack, et al. (2003). "A Chemical Route to Carbon Nanoscrolls." Science **299**(5611): 1361.
[23] Li, X., X. Wang, et al. (2008). "Chemically Derived, Ultrasmooth Graphene Nanoribbon Semiconductors." Science **319**(5867): 1229-1232.
[24] Hernandez, Y., V. Nicolosi, et al. (2008). "High-yield production of graphene by liquid-phase exfoliation of graphite." Nat Nano **3**(9): 563-568.
[25] Hummers, W. S. and R. E. Offeman (1958). "Preparation of Graphitic Oxide." Journal of the American Chemical Society **80**(6): 1339-1339.
[26] Gómez-Navarro, C., J. C. Meyer, et al. (2010). "Atomic Structure of Reduced Graphene Oxide." Nano Letters **10**(4): 1144-1148.
[27] Sutter, P. (2009). "Epitaxial graphene: How silicon leaves the scene." Nat Mater **8**(3): 171-172.
[28] de Heer, W. A., C. Berger, et al. (2007). "Epitaxial graphene." Solid State Communications **143**(1–2): 92-100.
[29] Lin, Y.-M., C. Dimitrakopoulos, et al. (2010). "100-GHz Transistors from Wafer-Scale Epitaxial Graphene." Science **327**(5966): 662.
[30] Wu, X., Y. Hu, et al. (2009). "Half integer quantum Hall effect in high mobility single layer epitaxial graphene." Applied Physics Letters **95**(22).
[31] Kim, K. S., Y. Zhao, et al. (2009). "Large-scale pattern growth of graphene films for stretchable transparent electrodes." Nature **457**(7230): 706-710.
[32] Gomez De Arco, L., Y. Zhang, et al. (2010). "Continuous, Highly Flexible, and Transparent Graphene Films by Chemical Vapor Deposition for Organic Photovoltaics." ACS Nano **4**(5): 2865-2873.
[33] Iwasaki, T., H. J. Park, et al. (2010). "Long-Range Ordered Single-Crystal Graphene on High-Quality Heteroepitaxial Ni Thin Films Grown on MgO(111)." Nano Letters **11**(1): 79-84.
[34] Reina, A., X. Jia, et al. (2008). "Large Area, Few-Layer Graphene Films on Arbitrary Substrates by Chemical Vapor Deposition." Nano Letters **9**(1): 30-35.
[35] Liu, W., B. L. Jackson, et al. (2010). "Large Scale Pattern Graphene Electrode for High Performance in Transparent Organic Single Crystal Field-Effect Transistors." ACS Nano **4**(7): 3927-3932.
[36] Li, X., W. Cai, et al. (2009). "Large-Area Synthesis of High-Quality and Uniform Graphene Films on Copper Foils." Science **324**(5932): 1312-1314.
[37] Li, X., C. W. Magnuson, et al. (2010). "Graphene Films with Large Domain Size by a Two-Step Chemical Vapor Deposition Process." Nano Letters **10**(11): 4328-4334.
[38] Li, X., C. W. Magnuson, et al. (2011). "Large-Area Graphene Single Crystals

Grown by Low-Pressure Chemical Vapor Deposition of Methane on Copper." Journal of the American Chemical Society **133**(9): 2816-2819.
[39] Gao, L., J. R. Guest, et al. (2010). "Epitaxial Graphene on Cu(111)." Nano Letters **10**(9): 3512-3516.
[40] Li, X., W. Cai, et al. (2009). "Evolution of Graphene Growth on Ni and Cu by Carbon Isotope Labeling." Nano Letters **9**(12): 4268-4272.
[41] "ASM Handbook; ASM International: 2002; Vol. 3, Alloy Phase Diagrams.".
[42] López, G. A. and E. J. Mittemeijer (2004). "The solubility of C in solid Cu." Scripta Materialia **51**(1): 1-5.
[43] Ching-Yuan, S. and et al. (2011). "Transfer printing of graphene strip from the graphene grown on copper wires." Nanotechnology **22**(18): 185309.
[44] Yan, K., H. Peng, et al. (2011). "Formation of Bilayer Bernal Graphene: Layer-by-Layer Epitaxy via Chemical Vapor Deposition." Nano Letters: 1106–1110.
[45] Rasool, H. I., E. B. Song, et al. (2010). "Continuity of Graphene on Polycrystalline Copper." Nano Letters **11**(1): 251-256.
[46] Cho, J., L. Gao, et al. (2011). "Atomic-Scale Investigation of Graphene Grown on Cu Foil and the Effects of Thermal Annealing." ACS Nano: 3607–3613.
[47] Wang, H., G. Wang, et al. (2012). "Controllable Synthesis of Submillimeter Single-Crystal Monolayer Graphene Domains on Copper Foils by Suppressing Nucleation." Journal of the American Chemical Society.
[48] Cai, W., Y. Zhu, et al. (2009). "Large area few-layer graphene/graphite films as transparent thin conducting electrodes." Applied Physics Letters **95**(12): -.
[49] Srivastava, A., C. Galande, et al. (2010). "Novel Liquid Precursor-Based Facile Synthesis of Large-Area Continuous, Single, and Few-Layer Graphene Films." Chemistry of Materials **22**(11): 3457-3461.
[50] Chen, Y. P. and Q. Yu (2010). "Nanomaterials: Graphene rolls off the press." Nat Nano **5**(8): 559-560.
[51] Gao, L., W. Ren, et al. (2012). "Repeated growth and bubbling transfer of graphene with millimetre-size single-crystal grains using platinum." Nat Commun **3**: 699.
[52] de la Rosa, C. J. L., J. Sun, et al. (2013). "Frame assisted H_2O electrolysis induced H^2 bubbling transfer of large area graphene grown by chemical vapor deposition on Cu." Applied Physics Letters **102**(2): 022101-022104.
[53] Wang, Y., Y. Zheng, et al. (2011). "Electrochemical Delamination of CVD-Grown Graphene Film: Toward the Recyclable Use of Copper Catalyst." ACS Nano. **5** (12): 9927–9933
[54] Reddy, K. M., A. D. Gledhill, et al. (2011). "High quality, transferrable graphene grown on single crystal Cu(111) thin films on basal-plane sapphire." Applied Physics Letters **98**(11): 113117-113113.
[55] Ismach, A., C. Druzgalski, et al. (2010). "Direct Chemical Vapor Deposition of Graphene on Dielectric Surfaces." Nano Letters **10**(5): 1542-1548.
[56] Levendorf, M. P., C. S. Ruiz-Vargas, et al. (2009). "Transfer-Free Batch

Fabrication of Single Layer Graphene Transistors." Nano Letters **9**(12): 4479-4483.
[57] Jeon, I., H. Yang, et al. (2011). "Passivation of Metal Surface States: Microscopic Origin for Uniform Monolayer Graphene by Low Temperature Chemical Vapor Deposition." ACS Nano **5** (3), pp 1915–1920
[58] Gao, L., G.-X. Ni, et al. (2014). "Face-to-face transfer of wafer-scale graphene films." Nature **505**(7482): 190-194.
[59] Kim, Y., W. Song, et al. (2011). "Low-temperature synthesis of graphene on nickel foil by microwave plasma chemical vapor deposition." Applied Physics Letters **98**(26): 263106-263103.
[60] Terasawa, T.-o. and K. Saiki (2012). "Growth of graphene on Cu by plasma enhanced chemical vapor deposition." Carbon **50**(3): 869-874.
[61] Kumar, A., A. A. Voevodin, et al. (2012). "Rapid synthesis of few-layer graphene over Cu foil." Carbon **50**(4): 1546-1553.
[62] Zhang, L., Z. Shi, et al. (2011). "Catalyst-free growth of nanographene films on various substrates." Nano Research **4**(3): 315-321.
[63] Sun, Z., Z. Yan, et al. (2010). "Growth of graphene from solid carbon sources." Nature **468**: 549-552.
[64] Pierson, H. O. (1999). 2 - Fundamentals of Chemical Vapor Deposition. Handbook of Chemical Vapor Deposition (CVD) (Second Edition). H. O. Pierson. Norwich, NY, William Andrew Publishing**:** 36-67.
[65] Krebs, H.-U., M. Weisheit, et al. (2003). Pulsed Laser Deposition (PLD) -- A Versatile Thin Film Technique. Advances in Solid State Physics. B. Kramer, Springer Berlin Heidelberg. **43:** 505-518.
[66] Hall, D. B., P. Underhill, et al. (1998). "Spin coating of thin and ultrathin polymer films." Polymer Engineering & Science **38**(12): 2039-2045.
[67] Abergel, D. S. L., A. Russell, et al. (2007). "Visibility of graphene flakes on a dielectric substrate." Applied Physics Letters **91**(6).
[68] Blake, P., E. W. Hill, et al. (2007). "Making graphene visible." Applied Physics Letters **91**(6).
[69] Ni, Z. H., H. M. Wang, et al. (2007). "Graphene Thickness Determination Using Reflection and Contrast Spectroscopy." Nano Letters **7**(9): 2758-2763.
[70] Smith, E. and G. Dent (2005). Modern Raman Spectroscopy: A Practical Approach, Wiley.
[71] Hodkiewicz, J. "Characterizing Carbon Materials with Raman Spectroscopy, Thermo Fisher Scientific, Madison, WI, USA.".
[72] Ferrari, A. C., J. C. Meyer, et al. (2006). "Raman Spectrum of Graphene and Graphene Layers." Physical Review Letters **97**(18): 187401.
[73] Graf, D., F. Molitor, et al. (2007). "Spatially Resolved Raman Spectroscopy of Single- and Few-Layer Graphene." Nano Letters **7**(2): 238-242.
[74] Hafner, B. "Scanning Electron Microscopy Primer." Characterization Facility, University of Minnesota—Twin Cities.
[75] Goldstein, J. (2003). Scanning Electron Microscopy and X-ray Microanalysis:

Third Edition, Springer US.
[76] Xie, J. and J. P. Spallas "Different Contrast Mechanisms in SEM Imaging of Graphene." Agilent Technologies Application Note.
[77] Schroder, D. K. (1998). Semiconductor Material and Device Characterization (2nd Edition), John Wiley & Sons, New York.
[78] Chan, J. "Four-Point Probe Manual (1994) ".
[79] Mattevi, C., H. Kim, et al. (2011). "A review of chemical vapour deposition of graphene on copper." Journal of Materials Chemistry.
[80] "PMMA Data Sheet, 2001, MicroChem Corp.".
[81] Kim, K., Z. Lee, et al. (2011). "Multiply folded graphene." Physical Review B **83**(24): 245433.
[82] Chen, J. H., C. Jang, et al. (2008). "Charged-impurity scattering in graphene." Nat Phys **4**(5): 377-381.
[83] Hwang, E. H., S. Adam, et al. (2007). "Carrier Transport in Two-Dimensional Graphene Layers." Physical Review Letters **98**(18): 186806.
[84] Ishigami, M., J. H. Chen, et al. (2007). "Atomic Structure of Graphene on SiO2." Nano Letters **7**(6): 1643-1648.
[85] Meyer, J. C., A. K. Geim, et al. (2007). "The structure of suspended graphene sheets." Nature **446**(7131): 60-63.
[86] Alemán, B. n., W. Regan, et al. (2010). "Transfer-Free Batch Fabrication of Large-Area Suspended Graphene Membranes." ACS Nano **4**(8): 4762-4768.
[87] Du, X., I. Skachko, et al. (2008). "Approaching ballistic transport in suspended graphene." Nat Nano **3**(8): 491-495.
[88] Luo, Z., C. Cong, et al. (2012). "Direct observation of inner and outer G' band double-resonance Raman scattering in free standing graphene." Applied Physics Letters **100**(24): 243107-243104.
[89] Zande, A. M. v. d., R. A. Barton, et al. (2010). "Large-Scale Arrays of Single-Layer Graphene Resonators." Nano Letters **10**(12): 4869-4873.
[90] Bolotin, K. I., K. J. Sikes, et al. (2008). "Ultrahigh electron mobility in suspended graphene." Solid State Communications **146**(9–10): 351-355.
[91] Sukang, B., K. Sang Jin, et al. (2012). "Towards industrial applications of graphene electrodes." Physica Scripta **2012**(T146): 014024.
[92] Hao, L., J. Gallop, et al. (2013). "Non-contact method for measurement of the microwave conductivity of graphene." Applied Physics Letters **103**(12): -.
[93] Hao, L., C. Mattevi, et al. (2012). "Microwave surface impedance measurements on reduced graphene oxide." Nanotechnology **23**(28): 285706.
[94] De, S. and J. N. Coleman (2011). "The effects of percolation in nanostructured transparent conductors." MRS Bulletin **36**(10): 774-781.
[95] De, S., P. J. King, et al. (2010). "Size Effects and the Problem with Percolation in Nanostructured Transparent Conductors." ACS Nano **4**(12): 7064-7072.
[96] Jo, S. B., J. Park, et al. (2012). "Large-area graphene synthesis and its application to interface-engineered field effect transistors." Solid State Communications **152**(15):

1350-1358.
[97] Habibpour, O., S. Cherednichenko, et al. (2011). "Mobility Improvement and Microwave Characterization of a Graphene Field Effect Transistor With Silicon Nitride Gate Dielectrics." Electron Device Letters, IEEE **32**(7): 871-873.
[98] Kim, E., T. Yu, et al. (2011). "Chemical vapor deposition-assembled graphene field-effect transistor on hexagonal boron nitride." Applied Physics Letters **98**(26): 262103-262103.
[99] Kim, S. H., S. Y. Yang, et al. (2006). "Low-operating-voltage pentacene field-effect transistor with a high-dielectric-constant polymeric gate dielectric." Applied Physics Letters **89**(18).
[100] Ryu, S., L. Liu, et al. (2010). "Atmospheric Oxygen Binding and Hole Doping in Deformed Graphene on a SiO2 Substrate." Nano Letters **10**(12): 4944-4951.
[101] Ni, Z. H., H. M. Wang, et al. (2010). "The effect of vacuum annealing on graphene." Journal of Raman Spectroscopy **41**(5): 479-483.
[102] Na, M. and S.-W. Rhee (2006). "Electronic characterization of Al/PMMA[poly(methyl methacrylate)]/p-Si and Al/CEP(cyanoethyl pullulan)/p-Si structures." Organic Electronics **7**(4): 205-212.
[103] Farmer, D. B., R. Golizadeh-Mojarad, et al. (2008). "Chemical Doping and Electron−Hole Conduction Asymmetry in Graphene Devices." Nano Letters **9**(1): 388-392.
[104] Guo, B., Q. Liu, et al. (2010). "Controllable N-Doping of Graphene." Nano Letters **10**(12): 4975-4980.
[105] Lu, Y.-F., S.-T. Lo, et al. (2013). "Nitrogen-Doped Graphene Sheets Grown by Chemical Vapor Deposition: Synthesis and Influence of Nitrogen Impurities on Carrier Transport." ACS Nano **7**(8): 6522-6532.
[106] Wang, X., J.-B. Xu, et al. (2011). "Quantitative Analysis of Graphene Doping by Organic Molecular Charge Transfer." The Journal of Physical Chemistry C **115**(15): 7596-7602.
[107] Singh, A. K., M. Ahmad, et al. (2013). "Tailoring the Electrical Properties of Graphene Layers by Molecular Doping." ACS Applied Materials & Interfaces **5**(11): 5276-5281.
[108] Se Hyun, K., Y. Won Min, et al. (2010). "Hysteresis behaviour of low-voltage organic field-effect transistors employing high dielectric constant polymer gate dielectrics." Journal of Physics D: Applied Physics **43**(46): 465102.
[109] Yan, H., T. Kagata, et al. (2008). "High-dielectric-constant hafnium silicate insulator for low-voltage pentacene field-effect transistors." physica status solidi (a) **205**(12): 2970-2974.
[110] Liu, J., D. Galpaya, et al. (2013). "Graphene-based thin film supercapacitor with graphene oxide as dielectric spacer." Applied Physics Letters **103**(6).
[111] Liu, C., Z. Yu, et al. (2010). "Graphene-Based Supercapacitor with an Ultrahigh Energy Density." Nano Letters **10**(12): 4863-4868.
[112] Zhang, F., T. Zhang, et al. (2013). "A high-performance supercapacitor-battery

hybrid energy storage device based on graphene-enhanced electrode materials with ultrahigh energy density." Energy & Environmental Science **6**(5): 1623-1632.
[113] Wan, X., L. Wang, et al. (2010). "Effect of variable substrate temperature for SrTiO3 thin films using pulsed laser deposition." Proceedings of the SPIE **7658**: 6.
[114] Kalyanaraman, R., R. D. Vispute, et al. (1997). "Influence of oxygen background pressure on crystalline quality of SrTiO3 films grown on MgO by pulsed laser deposition." Applied Physics Letters **71**(12): 1709-1711.
[115] Shivaraman, S., R. A. Barton, et al. (2009). "Free-Standing Epitaxial Graphene." Nano Letters 9(9): 3100-3105.
[116] Song, J., F.-Y. Kam, et al. "A general method for transferring graphene onto soft surfaces." Nat Nano 8(5): 356-362.
[117] "Photolithography Manual". Thin film Technology lab, Imperial College London